Quasi-Static and High Strain-Rate Mechanical Behavior of FP™ (α-alumina) Long Fiber Reinforced Magnesium and Aluminum Metal Matrix Composites

By
Övünç AKİL

A Dissertion Submitted to the
Graduate School in Partial Fulfillment of the
Requirements for the Degree of
MASTER OF SCIENCE

Department: Materials Science & Engineering
Major: Materials Science & Engineering

İzmir Institute of Technology
İzmir, Turkey

December, 2004

We approve the thesis of **Övünç AKİL**

Date of Signature

---------- **08.12.2004**

Assoc. Prof. Dr. Mustafa GÜDEN
Supervisor
Department of Mechanical Engineering

---------- **08.12.2004**

Assoc. Prof. Dr. Metin TANOĞLU
Department of Mechanical Engineering

---------- **08.12.2004**

Asist. Prof. Dr. Engin AKTAŞ
Department of Civil Engineering

---------- **08.12.2004**

Prof. Dr. Muhsin ÇİFTÇİOĞLU
Head of Depatment

ACKNOWLEDGEMENT

I am deeply indebted to my advisor, Assoc. Prof. Dr. Mustafa Güden, for his costant support. He carefully guided me throughout the pursit of my Masters Degree at İzmir Institute of Technology. His ideas and sugesstions have been invaluable to this thesis.

I am grateful to my Institute, İzmir Institute of Technology, for supporting financial assistantship throughout my Master of Science education.

I would like to thank to my co-advisors, Prof. Dr. I.W. Hall and Prof. Dr. Muhsin Çiftçioğlu for their help in my studies.

I would also like to thank Alper Taşdemirci, for his helps in Split Hopkinson Pressure Bar (SHPB) tests, and Iztech-CMR staff, for their help in Scanning Electron Microscope (SEM), and in Atomic Force Microscope (AFM).

I would also thank to my friends and to my family for their support. They were always there when needed.

Lastly I would thank to my wife for her patience and supports.

ABSTRACT

The mechanical response of an FP long fiber (35%) Mg composite has been determined in the transverse and longitudinal directions in compression. Results were also compared with those of a similar composite of Al matrix. It was found that the composite in the transverse direction exhibited strain rate sensitivity of the flow stress and maximum stress within the studied strain rate range (10^{-4} to $1x10^{3}s^{-1}$). However the increase in strain rate decreased the failure strain. Microscopic observations on the failed samples have shown that the composite failed predominantly by shear banding. Near to the fracture surface DRX grains were observed within the shear band and it was proposed that the lower ductility of the composite at increasing strain rates was due to the early DRX grain formation which softened the composite and resulted in lower ductility. Although twinning was observed in the deformed cross-sections of the samples at all strain rates particularly near the shear band region, it was proposed that the main deformation mechanism was slip which was evidenced by the slip lines on the fracture surface. The strain rate sensitivity in fracture stress of the composite in transverse direction was also found to be similar to that of the Al composite tested in the same direction. In the longitudinal direction, the composite failed by kink formation at quasi-static strain rates, while kinking and splitting at high strain rates. The maximum stress in the axial direction was however found to be strain rate insensitive. In this direction similar to transverse direction DRX grain formation was observed in the kink region. The lack of strain rate sensitivity in this direction was attributed to DRX grain formation at high strain rates combined with adiabatic heating and the brittle nature of the composite leading to fluctuatiton in the compressive strength.

ÖZ

Bu çalışmada fiber doğrultusunda ve fiber doğrultusuna dik yönlerde FP™ uzun fiber takviyeli (%35) Mg kompozitin basma davranışı incelenmiştir. Aynı zamanda bulunan sonuçlar benzer özellikteki Al esaslı kompozit ile karşılaştırılmıştır. Kompozitin akma stresi ve maksimum stres değerlerinin, çalışılan aralıkta ($1x10^{-4}$ to $1x10^{3}s^{-1}$), fiber doğrultusuna dik yönde uzama oranına duyarlı olduğu tespit edilmiştir. Kırılan numuneler üzerinde yapılan mikroskobik incelemelerde kompozitin kırılmasında kayma bandının baskın olduğu gözlenmiştir. Kırılma yüzeyi civarında yeniden kristallenme tanecikleri gözlenmiş olup, bunların artan uzama oranlarında erken oluşan dinamik yeniden kristallenme taneciklerinin kompoziti yumuşatması sonucu kompozitin tokluğunu düşürdüğü düşünülmektedir. Bunun yanında tüm uzama oranlarında, deforme olmuş kesitlerde, özellikle kayma bandı bölgesinde, ikizlenme gözlenmektedir. Asıl deformasyon mekanizmasının, kırılma yüzeylerinde gözlenen kayma düzlemlerinden anlaşıldığı üzere, kayma olduğu düşünülmektedir. Kompozitin fiber doğrultusuna dik yöndeki kırılma gerilmesinin uzama oranına duyarlılığı aynı yöde test edilen Al esaslı kompozit ile benzerlikler gösterdiği saptanmıştır. Kompozitin statik uzama oranlarında fiber doğrultusunda sapma bantlarının oluşumu ile kırılmasına karşın, dinamik yükler altında sapma bantları oluşumunun yanısıra boyuna ayrılma ile kırıldığı görülmüştür. Fiber doğrultusunda maksimum gerilmenin uzama oranına duyarlı olmadığı gözlenmiştir. Fiber doğrultusuna dik yönlerde olduğu gibi fiber doğrultusundaki testlerde de, dinamik yeniden kristallenme, özellikle sapma bantı bölgelerinde gözlenmiştir. Bu yöndeki uzama oranı duyarsızlığı, dinamik yükler altında adiabatik ısınma ile oluşan dinamik yeniden kristallenme taneciklerine ve basma gerilmesindeki değişkenliğin neden olduğu kompozitin doğal kırılganlığına bağlanabilir.

TABLE OF CONTENTS

LIST OF FIGURES

LIST OF TABLES

Table **Page**

CHAPTER 1

MAGNESIUM AND MAGNESIUM BASED METAL MATRIX COMPOSITES

1.1 Magnesium and alloy designation

Although Magnesium (Mg) was identified as an element in 1755, its commercial production did not start until about 1920. It differs form other metals as being the lightest engineering metal with a specific gravity of 1.738 which is about 64.3% lighter than aluminum. The elastic modulus of Mg is 45 GPa and in the pure form the tensile strength can be as low as 70 MPa. Primarily due to the relatively low strength, engineering structural application of Mg is usually with alloy additions. The primary alloying elements are aluminum (Al), manganese (Mn), and zinc (Zn). Less common elements such as thorium (Th), zirconium (Zr), and rare earths are also used. These elements have relatively low solubility at decreasing temperatures; therefore, age hardening can be produced similar to Al, copper (Cu), and other nonferrous alloy systems. Al is probably the most important alloying element for Mg. It has a solubility of 12.7% at the eutectic temperature, and only about 2% at room temperature. Small concentrations yield solid solution strengthening, while high concentrations lead to the ability to age hardens. Zn-addition in small concentrations (<1%) improves castability and corrosion resistance and Mn-addition improves corrosion resistance. The rare earths and other elements are used in small concentrations for solid solution strengthening and to improve elevated temperature properties. Lithium-addition to magnesium increases the c/a ratio along with improved forming properties, reduced the density and increased specific strength and corrosion resistance.

The most widely used alloy designation for Mg is the ASTM standart. (American Society for Testing Materials). The ASTM alloy designation system uses numbers and letters. The first two letters indicate the major alloying elements; the second part of the designation indicates the nominal amounts of the principal alloying elements; the third part is a letter from A to Z (except I and O) to indicate a different alloy with the same nominal composition. Suffixes like those used in aluminum system follow the alloy designation to indicate condition and heat treatments such as;

AZ	63	A	T6
Al and Zn are the principal alloying elements	6% Al 3% Zn	First alloy with this composition	Solution treaed and age hardened

Some additional code letters are listed in Table 1.1. A second alloy with a composition similar to the **examplecities** would have a B after the number: AZ63B. Typical suffixes used in ASTM coding are listed are in Table 1.2. In Table 1.3 the alloy designation of ISO and ASTM standards for most widely used magnesium alloys are listed.

Table 1.1 Some designation codes and corresponding elements of some alloys

Code	B	C	D	E	F	H	K	L	M	N	P	Q	R	S	T
Element	Bi	Cu	Cd	Rare Earth	Fe	Th	Zr	Li	M	Ni	Pb	Ag	Cr	Si	Sn

Table 1.2 Some suffixes and corresponding explanations of alloy properties

Suffix	**Explanation**
F	As fabricated
0	Annealed
H1X	(12=½ hard, 14=¼ hard, 16=¾ hard, 18=full hard)
H2X	(22, 24, 26 and 28, strain hardened and partially annealed)
T4	solution heat treated
T5	artificially aged only
T6	Solution heat treated and artificially aged

Table1.3 Alloy designation of ISO and ASTM standards for most widely used magnesium alloys

Alloy Designation (ISO Standards / ASTM)	Elements	Al	Cu	Fe	Mn	Ni	Si	Zn	Ca	Th	Zr	Rare Earths	Others
MgAl3Zn1(21) / AZ31B	Min %	2,5						0,5					
	Max %	3,5	0,05	0,01	0,2	0,01	0,1	1,5	0,04				
MgAl6Zn1(22) / AZ61A	Min %	5,5						0,5					
	Max %	7,2	0,05	0,01	0,15	0,01	0,1	1,5					
MgAl6Zn3 / AZ63A	Min %	5			0,1			2					
	Max %	7	0,2	0,05	0,5	0,01	0,3	3,5					
MgAl8Zn / AZ80A	Min %	7,5			0,15			0,2					
	Max %	9	0,2	0,05	0,6	0,01	0,3	1					
MgRE3Zn2Zr / EZ33A	Min %							0,8			0,4	2,5 to 4	
	Max %		0,1			0,01		3			1		
MgTh3Zn2Zr / HZ32A	Min %							1,7		2,5	0,4	0,1	
	Max %		0,1			0,01		2,5		4	1		
MgZn4REZr / ZE41A	Min %							3,5			0,4	0,75 to 1,75	
	Max %		0,1			0,01		5			1		
MgZn5Zr / ZK51A	Min %							3,5			0,4		
	Max %		0,1			0,01		5,5			1		
MgZn6Th2Zr / ZH62A	Min %							5		1,5	0,4		
	Max %		0,1			0,01		6		2,3	1		
MgZn6Zr / ZK61A	Min %							5,5			0,6		
	Max %		0,1			0,01		6,5			1		

1.2. The application areas of Magnesium alloys and their composites

Development of novel engineering metallic materials with low density and high strength for the use in aerospace and vehicle production industries is of great interest. Such materials are for example currently demanded in automotive industry in order to improve the economy of fuel consumption. During the last decade, magnesium alloys as lightweight structural materials were rediscovered by car manufacturers, thus greatly simulating extensive research activities as to the development of new magnesium alloys with improved strength, stiffness and corrosion properties [1].

In 1920's Mg parts were used in racing cars. Mg castings were however not extensively used in commercial vehicles until 1936 when the Volkswagen Beetle was introduced. The car contained around 20 kg of Mg in the power train and during its peak production in 1971, consumption of magnesium reached 42,000 tones per annum. The magnesium consumption then declined. The technological advances in the alloy performance made in the mid 1980's and the continuous drive to minimize the weight and fuel consumption increased the magnesium production again. Over the past 10 years, there has been significant growth of magnesium in the high pressure die-casting sector, averaging almost 20% per annum worldwide. Further growth is forecast over the next 10 years. In Europe, the increase of magnesium usage as a structural lightweight material is being led by the Volkswagen Group of companies, with the material also being used by other leading manufacturers including Daimler-Chrysler (Mercedes Benz), BMW, Ford and Jaguar. Presently, around 14 kgs of magnesium are used in the VW Passat, Audi A2, A4 and A6. The vehicles use magnesium transmission castings of AZ91D offer a 20%-25% weight saving over aluminum. Other applications include intake manifolds, cylinder head covers, inner boot lid sections and steering wheel cores and column components which utilize the more ductile AM50A & AM60B alloys. In North America, the use of magnesium for auto applications is more advanced. The GM full sized Savana & Express vans use up to 26kg of magnesium alloy.

The motor sport industry worldwide has long recognized the advantages to be gained from using the sand cast high performance alloys originally developed for the aerospace industry. Their lightweight and high strength to weight ratio provide many

teams with a competitive advantage. Elektron®RZ5 gearboxes are commonly used in Formula 1 and most other categories of motor sport. In some cases, Elektron®MSR-B or Elektron®WE43 gearboxes are used where superior properties are required. Elektron®WE43 and Elektron®WE54 alloys in cast and wrought form are being used increasingly in motor racing engines, often due to the high operating temperatures. Elektron®WE54 pistons have been run in Formula 1 engines and offers the potential for future performance improvement.

Magnesium alloys are extensively used for a range of helicopter transmission casings. Elektron®RZ5 is an alloy specified for applications operating up to 150°C due to its excellent castability and good mechanical properties. However, the requirements for longer intervals between overhauls and improved corrosion performance has led to Elektron®WE43 being selected, as the material of choice, for many new helicopter programs including the MD500, Eurocopter EC120, NH90 and Sikorsky S92. Elektron®WE43 has the added advantage of superior mechanical properties compared to Elektron®RZ5.

In defense industry magnesium alloy products are also used in a wide range of forms including castings, powders and wrought products. Structural castings have been utilized in equipments where its low density offers a significant advantage. Casting size varies considerably, from the large sand cast components utilized on armored vehicles, to the more intricate sand and investment castings present in radar equipment, portable ground equipment and Stingray torpedoes. Both sand and investment castings in the defense industry have made extensive use of Elektron®RZ5. Anti tank ammunition rounds have been a major application for magnesium extruded bar. APDS tank ammunition utilizes a magnesium sabot to facilitate the firing of a narrow projectile from a standard 120 mm or 100 mm gun barrel. Once discharged, the sabot is discarded allowing the projectile to continue its course to the intended target. AZ80, AZ61 and AZM are the preferred alloys for this application. Fine and atomized powders are widely used by the military industry in a range of flare and ordnance applications, notably decoy flares and illumination flares. Decoy flares made from magnesium burn white hot and the intense heat of the pyrotechnic candle consumes the flare housing. Such flares are designed to defeat a missile's infrared tracking capability thus making the use of magnesium instrumental in the protection of military helicopters and aircraft.

Ground illumination flares are designed to descend by parachute and illuminate ground terrain and targets.

1.3. Deformation behavior of Magnesium Alloys and Magnesium Metal Matrix Composites

Magnesium has hexagonal close pack (HCP) structure characterized with the limited number of slip systems which makes its machining and forming operations difficult. Because of their relatively poor mechanical properties, rapid loss of strength at temperatures above the ambient and poor creep resistance at elevated temperatures, magnesium is rarely used in high performance and temperature applications in pure form and alloying element addition are generally used to improve mechanical properties. The properties needed for high performance applications such as high modulus and strength, high wear resistance can be resolved by composite structures composed of particulate, short fiber, whisker and long fiber reinforcements. [2, 3, 4, 5, 6, 7, 8, 9]

1.3.1. Quasi-Static Behavior

At a previous study the effects of microstructures and textures of pure magnesium hot-rolled at 400°C in plane-strain compression were investigated [8]. After rolling the plate had grain size of 47 μm and a fiber texture 30° of the plate normal direction. Compression tests were conducted parallel (RD) and normal to the rolling (ND) directions. Because the deformation of polycrystalline magnesium typically produces a texture in which c-axis aligned in the compression direction, in the samples tested through RD, most grains were compressed normal to c-axis direction, while in the samples tested through ND, the grains were compressed along the c-axis. Both samples contained a large number of twin boundaries. Nave and Barnett also observed that the twinning modes in pure polycrystalline Mg showed well agreements with those of polycrystalline AZ31 alloy which was investigated by Yang et.al [10]. Also Barnett [11] investigated the influence of deformation conditions on the high temperature flow stress of AZ31 alloy (3%wt Al, 1%wt Zn, and 0.2%wt Mn). Compression and torsion tests

were conducted on the cylindrical specimens. In uniaxial compression test within the strain rate region between 0.3 s^{-1} and 0.001s^{-1} the flow stress increased with increasing strain rate. Similarly the flow stress in torsion test data increased with increasing strain rate and decreasing temperature. At in another work [10] both theoretically and experimentally, twin orientations in AZ31 alloy was predicted. It was shown that the deformation behavior of polycrystalline magnesium depended strongly on its initial texture structure. Also Myshlyaev et. al. [12] investigated the twinning, dynamic recovery and recrystallization in hot worked AZ31 alloy through torsion test. Torsional peak stress was found to decrease with increasing temperature and decreasing the strain rate. The fracture strain, however, increased with increasing testing temperature and with decreasing the strain rate. At increasing temperature, twins were rarely seen and DRX (dynamical recrystallized crystal) grains formed in place of the original grains. Beside these Kleiner and Uggowitzer [13] investigated the mechanical anisotropy in AZ61 alloy. The extruded AZ61 alloy samples were tested in compression and tension with five different tilt angles. The orientation dependence of the stress was found to be much clearly seen in tension than in compression. The twinning strain although decreased in compression, it increased in tension with increasing tilt angle.[13]

Yan et.al. [14] investigated the effect of constraint on the tensile behavior of an AZ91 (9% Al, 1%Zn, and 0.21%Mn). Tensile tests were performed on the smooth and circumferentially notched samples of different notch radii. The average stress found to increase with decreasing notch radii while average strain increased with increasing notch radii. The compressive plastic deformation of an AS21X magnesium alloy were studied by Barbagallo et. al. [9]. Cylindrical specimens were hot compressed at different temperatures and strain rates after a solution treatment. The stress values decreased with increasing temperature and increasing strain rates. At lower temperatures (about 150 ^{o}C) microstructural behavior was connected to the presence of recovery processes while at higher temperatures (at about 300 ^{o}C) recrystalization was observed [8]. Also DRX formation in a ZK60 alloy was investigated by Galiyev et. al. [15]. The cylindrical specimens were deformed by uniaxial hot compression at a constant strain rate. At **423 ^{0}K** twinning and dislocation glide revealed. At **523 ^{0}K** basal and non basal slip systems were observed to be operative. Short and wavy slip lines associated with cross-slip were found near the original grain boundaries. At **623 ^{0}K** extensive multiple slip was observed within the original grains, and the density of a+c dislocations decreased

with increasing temperature. As the temperature increased from **573** to **723** ^{o}K, new grains were formed at the grain boundaries.

Also there are many studies about the quasi-static behavior of Mg Matrix composites [1, 2, 4-7, 16-30]. Sharma et al [16] investigated the wear resistance of AZ91 alloy with the addition 30-50 μm size 1-5% volume percentages of feldspar particles. The feldspar particle composite showed lower wear rate than that of the unreinforced matrix alloy and the wear rate also decreased with increasing the particle volume fraction of feldspar. The damping properties of pure and 20 μm size and 10% SiC-particule (SiC_p) reinforced magnesium composite investigated at an early study [4]. The damping of magnesium increased with SiC_p addition which was attributed to the increased energy dissipation by the presence of particles itself and improved matrix structure due to particle addition. The mechanical properties of a 150 μm size 10% titanium particle reinforced magnesium metal matrix composite prepared by a powder metallurgical route composing of powder mixing and extrusion at 400 ^{o}C were studied by Pérez et.al [17]. The composite showed relatively high strength and the ductility higher than that of ceramic-reinforced magnesium composites. The breakage of coarse titanium particles suggested the load transfer contribution to the hardening of the composite and resulted form the good bonding between magnesium and titanium particles. Seshan et. al. [5] studied the tensile behavior of heat-treated AM 60 (Mg-6Al) and AZ92 (Mg-9Al-2Zn) alloys containing 20 μm size SiC_p with the volume percentages of 10 and 15%. Compared to unreinforced alloy counterparts, composites show relatively low increases in yield strength, marginal decreases in ultimate tensile strength and significant reductions in percentage elongation to failure. The reduced ductility of the composites was attributed to the fine microscopic cracks initiated at low values of applied stress. The microscopic analysis of the fracture surfaces of the composites showed the particle fracture, decohesion of interface and fast fracture through matrix. Lu et. al. [6] investigated the microstructural changes and mechanical properties of the magnesium alloys containing different amounts of $MgSi_2$ (5, 10 and 15%) synthesized via mechanical milling method. The presence of $MgSi_2$ phase inhibited grain growth. The yield strength and percentages of $MgSi_2$ phase of the composite also increased with increasing ball milling duration. The addition of aluminum as an alloying element further increased the strength, while the increasing of $MgSi_2$ phase reduced the percentage elongation. The effect of four different particulate

reinforcement additions analyzed , ZrB_2, SiC, TiC and TiB_2 with the amounts 5, 8, 12 and 15%, on the mechanical properties of Mg-9%Al alloy produced by powder metallurgy [18]. Among the investigated composites, ZrB_2 composite showed highest yield strength and TiB_2 reinforced lowest yield strength. The yield strength values of the composites were higher than that of the unreinforced matrix alloy, except TiB_2 reinforced composite which showed similar yield strength values as unreinforced matrix alloy. The percentage elongation decreased, with the particulate addition and increasing volume fraction of the reinforcements. The fabrication and characterization of pure magnesium reinforced with 30% SiC_p particulate composite investigated by Saravanan and Surappa [19]. The composite was produced by melt stir technique followed by hot extrusion. The composite yield and ultimate tensile strength values were higher than those of the unreinforced alloy and it showed superior strength up to 400 ^oC compared to unreinforced magnesium. However the elongation to failure reduced to form 12% in pure magnesium to 2% in the composite. An enhanced wear resistance of the composite as compared with pure magnesium was also found. Also Jiang et al. [7] fabricated 10% TiC particulate reinforced AZ91 magnesium composite via self-propagation high-temperature synthesis reaction into molten magnesium using semi-solid slurry stirring process. The ultimate tensile strength, hardness and wear resistance of the composite were found higher than unreinforced alloy. The TiC particle reduced the elongation to failure from 9% in the unreinforced alloy to 4% in the composite. Lim et. al. [20] investigated the wear behavior of a 14 μm size 8% SiC_p reinforced AZ91 alloy composite under 10 and 30 N. At lower load composite showed higher wear resistance compared to unreinforced alloy. This was mainly due to the higher load-bearing capacity of the composite and its ability to maintain stable oxide film which protected metal-metal contact during sliding. At the higher load, the wear resistance of the composite reduced due to transition form oxide to delamination and abrasion which was promoted by the presence of second phase.

The wear behavior of 10, 20 and 30 v% TiB_2 particulate reinforced pure magnesium composite fabricated by powder metallurgy was investigated. As compared with pure magnesium, the hardness of the composite was higher and increased with increasing TiB_2 content. TiB_2-addition also increased the wear resistance of the composite compared to unreinforced matrix. Lianxi and Erde [2] investigated fabrication and mechanical properties of SiC-whisker (SiC_w) reinforced ZK51A alloy. They applied a

two-step squeeze casting composite manufacturing process which reduced the deformation of the perform during casting to a very low level and ensured as-design reinforcement volume fractions in the composite. Within the studied whisker volume fractions (0-20%) liner increases in elastic modulus and yield strength of the composite with whisker volume fraction were reported. The increasing whisker volume fraction although increased the ultimate tensile strength, it reduced the elongation to failure significantly. It was also shown that low casting temperatures did not promote sufficiently strong interface bonding and high casting temperature resulted in melt oxidation and coarsening of the matrix microstructure. The fracture and deformation behavior of an 20% SiC_w/Az91 magnesium composites, produced by squeeze casting, via in-situ tensile testing in a transmission electron microscope analyzed by Zheng et.al. [22]. The deformation was localized at the whisker-matrix interface and micro cracks formed near the interface in the matrix. The final failure occurred by the linkage of micro cracks. Although whiskers and twins were suggested to impede the crack propagation their overall effects were to accelerate the crack formation due to high stress concentrations formed nearby them. It was suggested that the poor ductility of the composite was mainly because of the inherent low ductility of magnesium matrix and the fracture mechanism was matrix-controlled. Investigation of the effect of interfacial reaction on the mechanical behavior of a SiC_w reinforced AZ91 magnesium alloy composite produced with binder ($Al(PO_3)_3$) and without binder were stuied [23]. The use of binder resulted in interfacial reaction (MgO-formation) and an increase in ultimate tensile strength and modulus of the composite compared to without binder composites. Zheng et al. [24] considered microstructure and mechanical properties of aluminum borate whisker reinforced Mg-Zn-Ce (MB8) and Mg-Zn-Zr (MB15) alloys composites produce by squeeze casting process. The composites contained 30%-36% of whisker. The whisker addition increased modulus, yield and ultimate tensile strength greatly but reduced the elongation to failure. A continues layer of MgO, 50-80 nm thick, was formed during squeeze casting in both alloy composites. The investigation of the effect of reinforcement architecture on the tensile and compressive mechanical properties of a planar random saffil short fiber reinforced RZ5 magnesium alloy composite were studied by Towle and Friend [25]. The modulus and yield strength were found slightly higher in fiber plane than normal to the fiber plane. The lower proof strength measured normal to fiber plane in compression as compared to tension was attributed to the residual stresses in the composite. The mechanical properties of the

composite were generally enhanced as compared with unreinforced alloy and the greatest enhancement was observed within plane proof and ultimate tensile strength in compression. The mechanical properties of Mg alloy composites with short Saffil fibers were also investigated [26]. In this work AZ91 and ZE41 alloys were used as matrix materials. Compression tests were conducted on cylindrical samples at temperatures between 20 and 300°C for both parallel and perpendicular to fiber plane. For both directions, reinforcing phase increases the yield strength especially at room temperature. With increasing temperature the anisotropy in the mechanical properties related to the fiber plane orientation decreased. It was also shown that the difference between the yield strength of composite and unreinforced alloy decreased with increasing temperature. The tensional mechanical properties of discontinuous steel fiber reinforced Mg-Li alloy composites of hcp and bcc structures produced by a molten metal inflation process followed by rolling and extrusion were determined by Jensen and Chumbley [27]. The hcp matrix composite had limited formability at temperatures up to 400°C while bcc matrix composites had exceptional formability when rolled at room temperature. It was proposed that texture analysis of the composites were required in order to characterize the deformation behavior of the composites.

Hausmann et. al. [28] investigated the effect aluminum additions on the tensional mechanical properties of 65% continuous T300 carbon fiber reinforced magnesium composite produced by direct squeeze casting process. The aluminum alloy additions to the unidirectional composite were 0, 0.5, 1, 2, and 5%. Although elastic modulus of the composite in fiber direction did not affected by the Al addition, the ultimate tensile strength increased with Al addition until 1%. Above 1% Al addition the ultimate tensile strength values decreased gradually below that of the unalloyed magnesium composite. The microscopic studies indicated that Al addition up to 1% resulted in matrix strengthening solely by solid solution, leading to a failure mode of fiber pull-out, while higher percentages of Al addition resulted in formation Al_4C_3 and needle Al rich grains which induced damages at fiber surfaces leading to brittle step-like or flat fracture surfaces [28]. Pahutova et. al. [29] investigated the creep resistance of 20% saffil (δ-Al_2O_3) fiber and 15% SiC_p reinforced AZ91 (Mg-9wt%Al-1wt%Zn-0.3%Mn) and QE22 (Mg-2.5wt%Ag-2wt%Nd rich rare earths-0.6wt%Zr) magnesium alloy composites and their unreinforced matrix alloys for comparison purposes. In short fiber composites of both matrix alloys the creep resistance increased considerably

compared to unreinforced alloys. Although the creep resistance of AZ91 alloy increased with SiC_p addition, particle addition into QE22 alloy decreased the creep resistance. It was further proposed that direct composite strengthening controlled the creep resistance of the short fiber magnesium composite. It was found that the indirect strengthening of fine particles as inhibiting dislocation motion although generally resulted in strengthening, it produced weakening in QE22 alloy [29]. The fabrication and mechanical properties of carbon fiber reinforced magnesium alloys were investigated in an early work [30]. The long carbon fiber reinforced AM20, AM50, AZ91 and MSR-B alloy composites were fabricated by high pressure infiltration technique. The effect of Al alloy addition on the microstructures of the composite was also investigated and found to be formation of the ternary Al_2MgC_2 carbide. It was shown that composites showed transverse tensile strength values decreasing with increasing fiber volume fraction. The failure of the composites along the fiber axis was shown to be a mixture of micro buckling and delamination. Both mechanisms were controlled by the matrix/fiber interface strength and the matrix shear strength. Almost a linear relation between composite axial compression strength and matrix compression strength was also shown. It was reported that the low transverse strength of the tested composites was caused by the low strength of the fiber/matrix interface [30].

The mechanical behavior of magnesium-lithium alloys and its composites have recently been rewived by Kudela [1]. It was emphasized that the use of steel and titanium wires could hardly be considered the feasible reinforcement for Mg-Li alloys because of the increase in the density of the resultant composite and excellent strength to weigh ratios was possible with the use of advanced carbon fibers. It was also stated that the excellent chemical compatibility between SiC_w and Mg-Li melts was believed due to the thin silica film which assisted the formation of strong interfacial bond.

1.3.2. High strain rate behavior

Despite the quite many experimental investigation were conducted for understanding of deformation behavior and determining mechanical properties of magnesium metal matrix and unreinforced alloys at quasi-static strain rates, there

existed limited number of studies on the effect of strain rate on the mechanical behavior of magnesium based metal matrix composites.

To determine the high strain rate behavior of Magnesium Klimanek and Pötzch [31] investigated the microstructural evolution of pure magnesium under compression at different strain rates and temperatures. Flow stress increased with decreasing temperature and with increasing strain rate, proved a strain rate sensitive flow stress behavior. The mean volume fractions of mechanical twinning in the samples tested at quasi-static and high strain rates at room temperature and 150 ^{o}C were measured to increase to a maximum at about 5% strain, then decreased and remained to be constant after 10% strain, while the mean twin size decreased only slightly with increasing strain. The decrease in the twin volume fraction between 5 and 10% strains was explained by the multiple twinning, which reduced the size of the twins, making twins invisible under the optical microscope. It was reported also that under the investigated strain rates (10^{-3},10^{-2}, $500s^{-1}$) and temperatures, the deformation strain rate and temperature did not influence the twinning process significantly. The dislocation density measurements as function of the strain have shown that dislocation density increased with increasing strain and strain rate, while the increase in dislocation density was relatively smaller in the strains less than 10% because of intensive twinning. In contrast Klimanek and Pötzch Mukai et.al. [32] investigated the effect of grain refinement on the tensile ductility of pure magnesium and a ZK600 alloy under dynamic loading. It was shown that the yield strength of the pure magnesium and ZK600 increased with decreasing grain size at high strain rates ($1.8x10^{3}$ s^{-1}) similar to the quasi-static behavior. The increase in yield strength in high strain rate as compared with quasi-static strain rate was however found higher in the alloy than pure magnesium. In high strain rate tested sample of ZK600 although macroscopic cracks along the twin boundaries were seen in coarse grained samples, these did not form in fine grained sample which enhanced the high strain rate ductility of the fine grained alloy. In another work Mukai et.al investigated the high strain rate superplasticity of ZK61 magnesium alloys [33]. To obtain the mechanical properties tensile tests conducted to cylindrical ZK61 samples. At the strain rates below 1×10^{-2} s^{-1} ZK61 alloy exhibits slight strain hardening opposite to higher strain rates. As expected at the highest strain rate 1×10^{-1} s^{-1} strain softening was observed over the large strains. Flow stress increased with increasing strain rate. Mukai et. al. [34] investigated the processing of ductile AZ31 magnesium

alloys under dynamic tensile loading. It was shown that the simple shear processing through equal channel angular extrusion (ECAE) following by annealing developed a texture different from the directly extruded alloy. Similar to Mukai et. al. Wei et. al. [35] investigated the supreplastic behavior of in magnesium alloy at high strain rates. Wei et. al. used rolled AZ91 magnesium alloys at temperatures ranging from 623 to 698 K. tensile tests are conducted to obtain superplastic behaviors. The true stress values are decreasing with decreasing strain rate and increasing rolling temperature. Twins are observed at the rolled alloy before tensile superplastic deformation. At the deformed samples cavities also observed.

Fjeldly and Roven [36] investigated the effects of strain rate and anisotropy on the tensile deformation properties of extruded AlZnMg Alloys. Tensile tests were conducted to cylindrical samples at different orientation directions. It is known that AlZnMg has strong mechanical anisotropy. The early fracture is in the extrusion direction and nominal strain increases with increasing orientation angle. Flow stress decreases with increasing strain rate, and this is significant at high strain values. Takuda et. al. [37] investigated the effect of strain rate on deformation behavior of an MgLiZn alloy. Uniaxial tension tests were carried out in the directions of 0, 45, and 90° to the rolling direction. At rolling direction sheet, especially in low strain rates, has sufficiently high formability. Also from the results of tension tests in the other directions shows similar with the results of rolling direction, although at normal to rolling direction, the elongations is slightly smaller than the others. From the microstructures of the samples tested at various strain rates, the grains of both α and β phases become smaller with increasing strain rate. Also the stress increases with strain rate while elongation decreases. Beside these El-Saeid Essa et. al. [38] investigated the damage and fracture mechanisms of 12%, 10 μm size SiC_p reinforced Mg-5%Zn-1%Mn magnesium alloy at quasi-static and high strain rate at different temperatures. Dynamic tests were conducted using a tensional split hopkinson pressure bar set-up. It was found that dynamically tested composite and unreinforced alloy showed higher flow stresses than those of quasi-statically tested counterparts. In dynamic test at room temperature, the percentage of particle fracture was higher than that of the dechored particles while in quasi-static test at room temperature the percentages of broken and dechored particles were similar. The effect of increasing testing temperature was to increase the

percentages of the decohered particles, but this effect was more pronounced in quasi-static tested samples.

The main objective of this experimental study is to determine compression mechanical properties of a long fiber reinforced Mg MMC as function of strain rate. The effect of strain rate on the important mechanical properties such as flow stress and failure stress and strain was determined and these were compared with those of a similar long fiber MMC that contained an Al matrix. This comparison will be expected to give valuable information of the effect of the matrix alloy type, hcp and fcc, on the strain rate dependent mechanical properties of MCCs. The study is therefore contribute to the literature in two ways; (ı) understanding the compression mechanical properties of Mg based long fiber composites at both quasi-static and high strain rates which has not been extensively investigated yet and (ii) experimentally determining the effect of matrix alloy type on the strain rate dependent mechanical properties of long fiber MMCs.

CHAPTER 2

COMPRESSION FAILURE MODES OF LONG FIBER REINFORCED COMPOSITES

2.1 Compression failure in the axial direction

Compressive failure in the axial direction of unidirectional long fiber reinforced composites may take place in following modes: elastic microbuckling, fiber crushing, matrix failure and plastic microbuckling [39]. These modes are shown sequentially in Figs. 2.1(a) through (d).

The earliest theory of elastic microbuckling was developed by Rosen [40]. Rosen assumed two different modes of deformation; shear and extensional modes as shown in Fig. 2.1(a). In shear mode, fibers buckle in phase producing shear stresses in the matrix while in extensional mode, fibers bend out of phase producing tensile stresses in the matrix. Assuming fibers were initially perfectly aligned, Rosen formulated the composite compressive strength (σ_c) for two modes of deformations as

Extensional mode: $$\sigma_C = 2V_f \sqrt{\frac{V_f E_m E_f}{3(1-V_f)}} \qquad (2.1)$$

Shear mode: $$\sigma_C = \frac{G_m}{(1-V_f)} \qquad (2.2)$$

Where V_f, E_m, E_f and G_m are the fiber volume fraction, matrix elastic modulus, fiber elastic modulus and matrix shear modulus, respectively. The compressive strength predicted by the extensional mode is however higher than the strength predicted by the shear mode. The predicted compressive strengths of Eqns. 2.1 and 2.2 were also found to be higher than experimental results at least a factor of 2. The model is based on the idealized fiber-matrix structures, therefore ignores the presence of possible defiencies such as fiber misalignment.

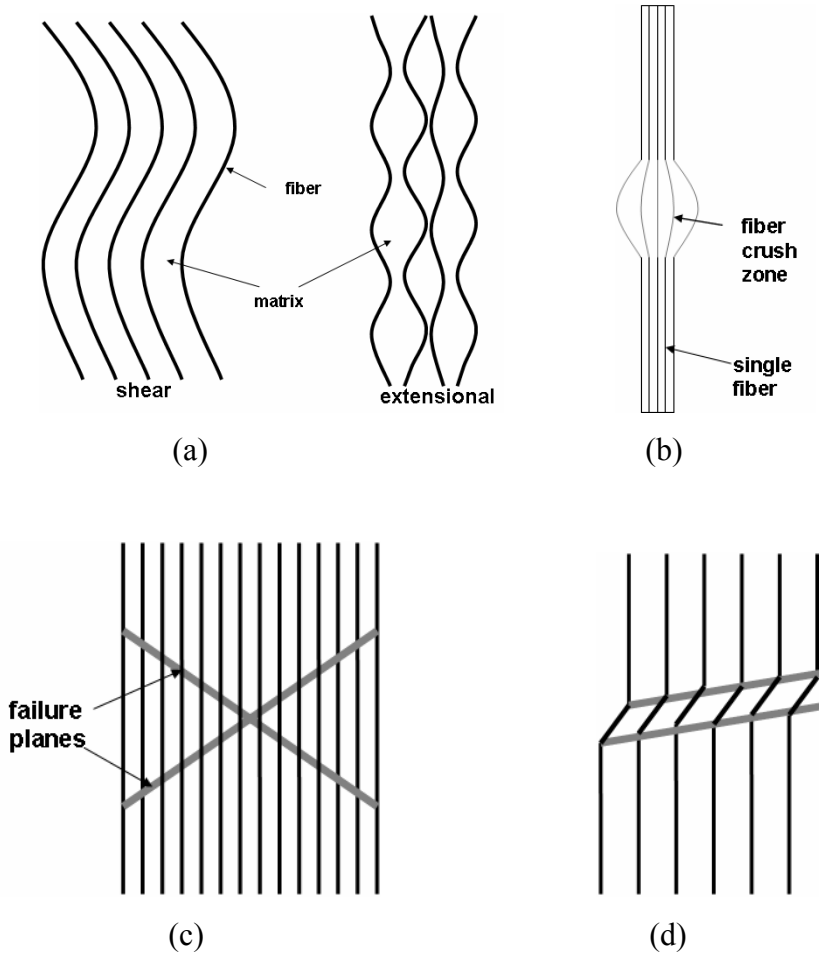

Fig. 2.1 Compressive failure modes in unidirectional fiber reinforced composite in the fiber direction (a) elastic microbuckling (b) fiber crushing (c) matrix failure and (d) plastic microbuckling (kinking or kink band formation).

When the axial strain of the composite reaches a critical value equal to the fiber failure strain, fiber crushing occurs. The fiber crushing might be in the forms of fiber splitting, plastic yielding of metal fibers and plastic buckling of the microstructural units in each fiber as shown in Fig. 2.1 (b).

Matrix failure of the composite in the axial direction is possible when the axial strain in the composite reaches a critical value equal to the matrix failure strain. The cracks in this mode propagate in a brittle manner through the matrix phase as depicted in Fig.2.1(c). The strength in this case was predicted using following equation:

$$\sigma_c = \sigma_m \left(\left[\frac{V_f E_f}{E_m} \right] + (1 - V_f) \right) \qquad (2.3)$$

Where σ_m is the matrix failure strength. This mode of failure was operative in ceramic matrix composites.

Plastic microbuckling occurs as a direct consequence of plastic microbuckling coupled with the low failure strain of the reinforcing fibers. Microbuckling is the buckling of the fibers embedded in a matrix while kinking or kink band is a highly localized fiber buckling as shown in Fig. 2.1(d).

In unidirectional composites, kink band formation was considered to be the primary failure mechanism limiting the composite strength in compression [39, 41, 42, 43]. Experimental studies on carbon fiber reinforced epoxy composites have shown that microbuckling initiated from intentionally induced holes or notches [44-46]. The microbuckling was found to initiate from the edge of the hole at a stress level of 80% of the compressive strength and propagated through the specimen [44]**.** In unnotched specimens, microbuckling initiates in regions of fiber misalignment [47]. Fiber misaligned regions can result in local shearing of the matrix, resulting in a reduced axial strength which is about 20-30% of the stress required to buckle fibers in a perfectly aligned composite [48].

The existing models of microbuckling are based on either on maximum compressive stress corresponding buckling stability followed by kink formation or assumption of pre-exist kinks [49]**.** Applying the former concept, Argon [50] have shown that the critical stress σ_c for buckling is

$$\sigma_c = \frac{\tau_y}{\phi} \tag{2.4}$$

where τ_Y is the interlaminar matrix shear strength and θ is the initial fiber misalignment with respect to compression axis. Argon's equation described the conditions needed nucleation of a localized buckling site which then spreads across the specimen at a shear angle. Budiansky [51] further modified Argon's equation for elastic-plastic shear response as

$$\sigma_c = \frac{\tau_y(\gamma)}{(\phi + \gamma)} \tag{2.5}$$

It can be easily seen from the Eqns. 2.4 and 2.5, that the dominant factors are the initial fiber misalignment and composite yield stress which scales with matrix shear yield

strength. The interpolation of the compressive strength of the unidirectional polymeric composites to the matrix yield strength has shown a linear relationship [39]. This interpolation has further predicted an initial fiber misalignment of 3˚ which seems reasonable for fiber lay-ups [52].

The schematic presentation of kink formation is shown in Fig. 2.2 The α , β, l and d labeled in Fig. 2.2 were kink angles and kink length and with respectively. Typical values of β is given as 20-30^{o} and α is nearly 2β for polymeric composites [39]. The morphology of kink formation has been summarized by Evans and Adler [41] and shown in Fig 2.2. If the fibers are well bonded such as composite studied here, the matrix within the kink must be subjected to a shear strain, presented as ϕ in Fig. 2.2. Therefore, the region of A'B'C and AOB must be experiencing a large localized strain which may lead to void formation. The microstructural analogy of Fig. 2.2 is shown in Fig. 2.3(a) and (b). In Fig. 2.3(b) the localized region of plastic deformation is noticeable.

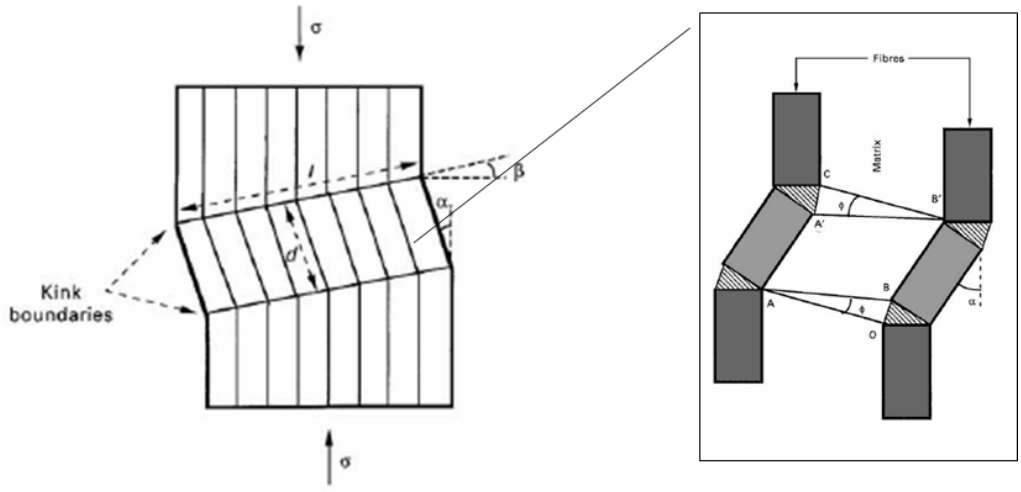

Figure 2.2. The schematic presentation of kink formation

The kink formation and the compressive stress/strain curve of the unidirectional composite may be considered in three distinct regions by analogy with the observations of kink formation in carbon-epoxy composites [53]. These three stages are incipient, transient and steady state kinking as shown in Fig. 2.3. Incipient kinking begins shortly before the peak stress and is characterized by non-linearity in the stress/strain curve near to the peak stress [45]. The non-linearity in the stress/strain curve near to the peak stress was suggested to be a cumulative effect of many small scale localized regions [54]. In

this region, the stress rises to the peak stress which shows the end of the incipient kinking region. In the transient kink region, the localized areas of the incipient kinking grow and coalescence to form a single kink band across the specimen. Due to localized deformation in this region, the stress drops from the peak value to a steady state. In this region fibers show axial compression and rotation until volumetric lock-up stiffens the response of the fibers within the kink band [53]. After that point, deformation proceeds laterally through the unkinked regions under constant stress, a process known as steady-state kink broadening [53].

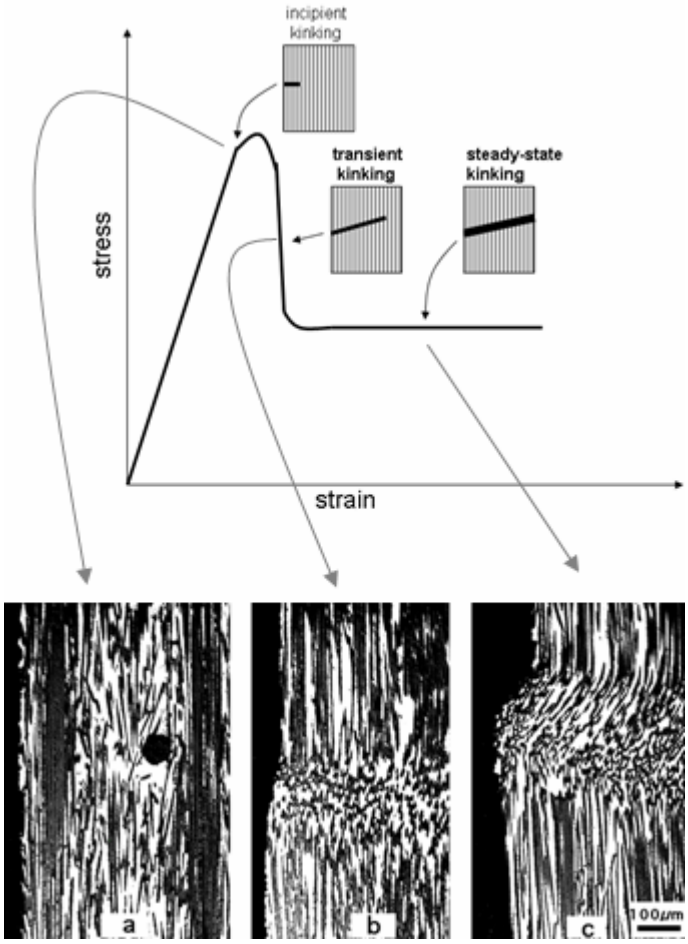

Figure 2.3. Progressive kink formation in a FP-Al_2O_3 fiber reinforced Al metal matrix composite (a) before kinking (1% strain), (b) fiber rotation and buckling (1.8% strain) and c) developed kink region (3% strain).

2.2 Compression failure in the transverse direction

Transverse compressive failure of unidirectional composites occurs usually by shear in the matrix (Figure 2.4) [54]. This mode of failure may be accompanied by

fiber-matrix debonding and crushing. Because of the difficulty of fibers sliding across each other along the shear band, transverse compressive strength $\sigma_{22}(C)$ for the unidirectionally reinforced composites is generally higher than the stress at which the unreinforced matrix material yields under compressive loading. Skudra (1985) proposed that $\sigma_{22}(C)$ can be determined from the following equation

$$\sigma_{22} = \frac{2\sigma_{22}(T)\sin 2\phi}{(1+\nu_{23})(1-\cos 2\phi)} \qquad (2.6)$$

where $\sigma_{22}(T)$, ϕ, are the transverse tensile strength of the lamina and inclination angle of the fracture path (experimentally determined) with respect to the direction of loading which can be seen at Figure 2.4

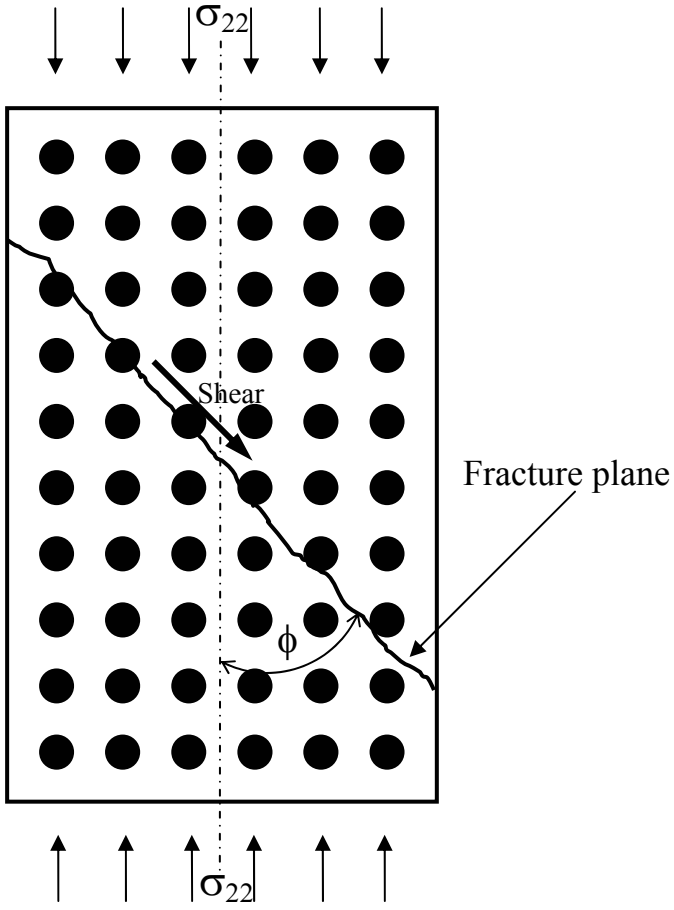

Figure 2.4 Compressive fracture of unidirectional composite in transverse direction.

CHAPTER 3

SPLIT HOPKINSON PRESSURE BAR TESTING

3.1. Consideration of Historical Developments

The first experimental study of high strain rate deformation was reported in 1872 by J. Hopkinson [55] who demonstrated that metals can withstand larger impulsive loads in tension than they can do under static loading. Following J. Hopkinson, his son, Bertram. Hopkinson [56] subsequently measured the pressure developed in a long steel rod caused by the impact of bullets or by the detonation of explosive charges at one end of the rod. The apparatus he used in his experiments was known as the Hopkinson Pressure Bar (HPB) and consisted of a long steel rod ballistically suspended. A steel pellet known as *time piece* was attached at the one end of the rod with a little grease or magnetism. The *time piece* had the same diameter as the steel rod and was made of the same steel. At the other end of the bar, the firing end, an elastic compression wave was created. The compression wave then propagated along the rod and, when it reached the greased joint, it was transferred to the sample without any change in its form. Since the rod was long compared to its radius, it was assumed that the wave propagated without any significant distortion. As soon as the compressive wave reached the free end of the bar, it was reflected as the tension wave. When a tension pulse developed at the rod/*time piece* interface the grease joint broke and resulted in the *time piece* flying off. The *time piece* was then caught by a momentum trap, from which its momentum could be easily measured, and at the same instant the momentum remaining in the rod was calculated from the amplitude of swing of the rod. By testing different lengths of *time piece*, the pressure-time curve of the rod could be easily calculated.

Although the HPB was very simple, it suffered from several problems. The technique could not give a continuous record of pressure-time relationship and the greased joint limited the measurements of the small amplitude pulses. In 1948, Davies [57] modified the HPB by placing a condenser microphone system at the free end of the

bar which could measure small displacements. This electrical measuring system allowed one to obtain a continuous record of the displacement/time response of the rod created by pressure pulse.

Following Davies, Kolsky [58] split the HPB into two bars, now known as incident and transmitter bars, to measure the stress/strain response of materials in compression. The specimens were sandwiched between incident and transmitter bar and a third bar, known as the striker bar, were used to create a stress pulse in the incident bar. Condenser records obtained from incident and transmitter bars were used to calculate specimen stress/strain curve. This new technique was then named the Split Hopkinson Pressure Bar or, in some cases, the Kolsky Bar.

3.2 SHPB Principles

SHPB principles are based on uniaxial elastic wave propagation in long bars. When a long bar having a velocity of v_o strikes another long bar at rest and having the same elastic modulus and diameter as the impact bar, a rectangular elastic stress pulse is produced in the impacted bar and the magnitude of stress and strain are direct functions of the velocity of the striking bar, modulus (E) and elastic wave velocity (C) of the impacted bar. The maximum stress (σ) and the maximum strain (ε) in the bar are given as follows [59]

$$\sigma_b = \frac{v_o E_b}{2C_b} \tag{3.1}$$

and

$$\varepsilon_b = \frac{v_o}{2C_b} \tag{3.2}$$

where b refers to the bar. Similarly, in any SHPB test the theoretical stress and the strain in the incident bar due to impact of the striker bar can be easily calculated using Equations 3.1 and 3.2.

Upon impact, the compressive stress wave generated travels down along the incident bar towards the specimen (Figure 3.1(a)). When it arrives at the interface

between incident bar and the specimen, the wave partially reflects back as a tensile wave and the remainder transmits through the specimen into the transmitter bar (Figure 3.1(b)). The relative magnitudes of the reflected and transmitted waves are a function of the difference in acoustic impedance of the specimen and the bar materials. At the interface of the specimen and the transmitter bar, part of the wave again reflects into the specimen. The dashpot is to protect the bar end from damage during the test.

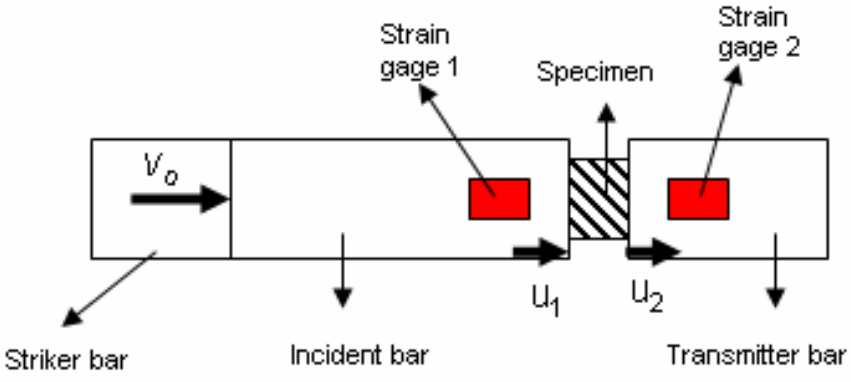

(a)

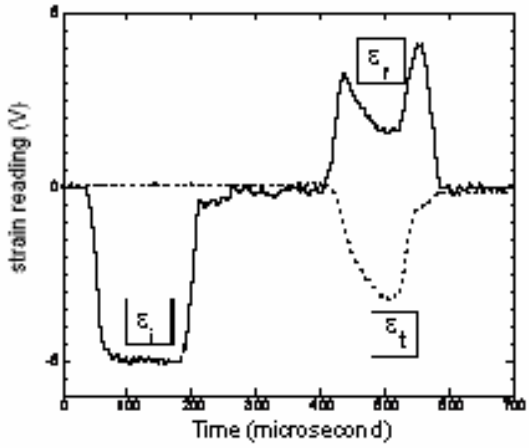

(b)

Figure 3.1 (a) Schematic of SHPB set up and (b) measured incident, reflected and transmitted strains.

The strain reading of the incident, reflected and transmitted bars, ε_i, ε_r and ε_t and the displacements of the incident and transmitter bars u_1 and u_2 (Figure 3.1 (a)) can be found using the following equations

$$u_1 = C_b \int_0^t (-\varepsilon_i + \varepsilon_r) d\tau \tag{3.3}$$

and

$$u_2 = -C_b \int_0^t \varepsilon_t d\tau \tag{3.4}$$

where *i*, *r* and *t* refer to incident, reflected and transmitted waves, respectively. The strain in the specimen is then

$$\varepsilon_s = \frac{u_2 - u_1}{L_s} = \frac{C_o}{L_s} \int_0^t (-\varepsilon_t + \varepsilon_i - \varepsilon_r) d\tau \tag{3.5}$$

where *L* is the length and *s* refers to the specimen. The loads on each interface, incident bar/specimen (1) and specimen/transmitter bar (2), are

$$P_1 = A_b E_b (\varepsilon_i + \varepsilon_r) \tag{3.6}$$

and

$$P_2 = A_b E_b \varepsilon_t \tag{3.7}$$

A is the cross-section. Assuming a stress equilibrium between bar/specimen interfaces (1 and 2 of Figure 2), so that $P_1 = P_2$, Equation 3.5 can be written as

$$\varepsilon_s = \frac{-2C_b}{L_s} \int_0^t \varepsilon_r d\tau \tag{3.8}$$

Accordingly, the stress in the specimen is

$$\sigma_s = \frac{P_1}{A_s} = \frac{P_2}{A_s} = \frac{A_b}{A_s} E_b \varepsilon_t \tag{3.9}$$

It should be finally noted that the above analysis assume that

1. The waves propagating in the bars can be described by the one-dimensional wave propagation theory.
2. The stress and strain fields in the specimen are uniform in its axial direction.
3. The specimen inertia effect and the friction effect in the compression test are negligible.

CHAPTER 4

MATERIALS AND TESTING METHODS

4.1 Materials

The unidirectional continuous FP™ fiber 99% α-Al_2O_3 reinforced ZE41A Mg MMC plate was produced and provided by E.I. Dupont Co. of the U.S.A. using a molten metal vacuum infiltration technique. In this technique, the FP tape was prepared using a fugitive organic binder and then tapes were laid up in the desired orientation, fiber volume and shape. After burning away the binder, the molten metal was infiltrated through the network of FP fibers in a casting mold of steel [60].

The composite material studied was manufactured in the form of 13 mm thick plate and contained 35 volume percent fiber, determined microscopically using an image analyzer. The matrix alloy contained 4.2%Zn, 0.7%Zr and 1.2% rare earths (mainly Ce). Typical microstructures of the MMC shown in Figs. 4.1(a) and (b) through longitudinal and transverse directions exhibits 100 μm in size α-Mg grains decorated by a pseudo ternary phase of Mg-Zn-Ce. The average fiber diameter was 20 μm.

Fiber FP is an aluminum oxide fiber developed by the Du-Pont Company for reinforcing metallic matrices. It is essentially 100% polycrystalline α-alumina with a purity of greater than 99% Al_2O_3 and fired to a density of 98% of theoretical so that the fiber is stable at elevated temperatures. The room temperature mechanical properties of the fiber and matrix alloy are tabulated in Table 4.1 and 4.2, respectively. The tensile modulus of the fiber varies between 345 and 379 GPa, and it has also relatively high tensile strength, 1380 MPa. The yield strength of the matrix was determined previously and found 140-148 MPa with a modulus of approximately 45 GPa and a tensile strength of 169-205 and a compressive strength of 330-365 MPa.[25,61,62,63]

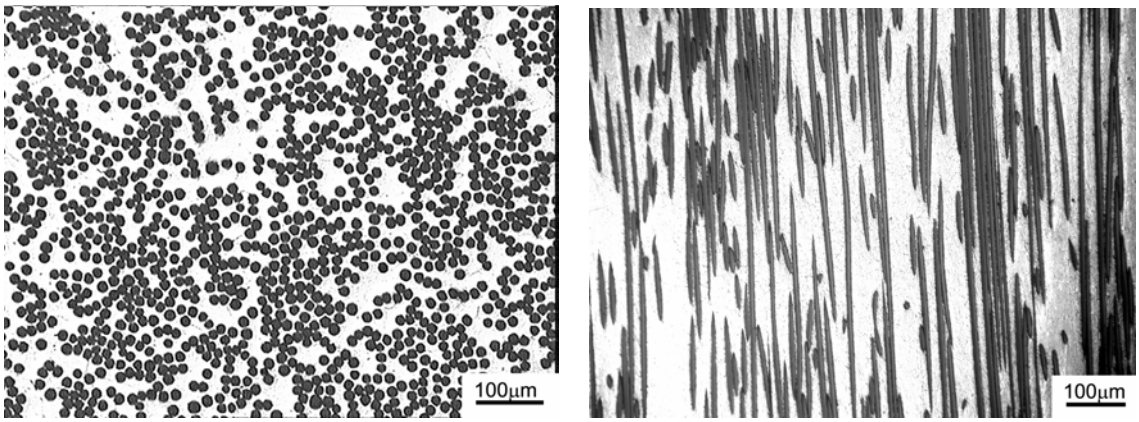

(a) (b)

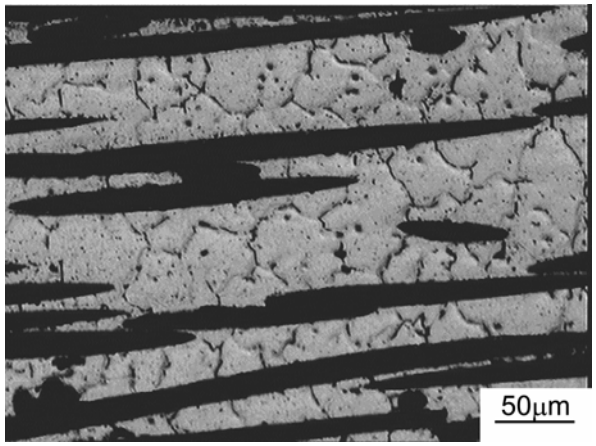

(c)

Fig.4.1 Optical micrographs of the composite in (a) transverse and (b) axial fiber directions and (c) etched surface of axial direction showing magnesium grains decorated by Mg-Zn-Re ternary alloy.

Table 4-1 mechanical properties of Fiber FP

Tensile Strength (MPa)	**Tensile Modulus (GPa)**	**Elongation (%)**	**Density (gr/cm^3)**	**Melting Point (^oC)**	**Filament Diameter (μm)**	**Reference**
1380	345-379	0.4	3.90	2045	20 ± 5	[60]

Table 4-2 Mechanical properties of matrix alloy.

Tensile Strength (MPa)	**Tensile Modulus (GPa)**	**Yield Strength (MPa)**	**Elongation tension (%)**	**Compressive Strength (MPa)**	**Compressive Moduslus (GPa)**	**Shear Strength (MPa)**	**References**
169	45.1			355	42,5		[25]
195							[61]
200	44	148	3	330-365		138	[62]
205		140	5				[63]

For comparison purpose, FP fiber reinforced Al matrix composite having the same volume fraction of fiber was also tested for comparison purposes. The composite contained 35 volume percent fiber (V_f%) and 3% Li in the Al matrix. The presence of Li provided wetting of FP fibers by aluminum[60]. The composite was previously tested by Guden and Hall [64] and at quasi-static and high strain rates. Additional tests at intermediate quasi-static strain rates (between $1.3x10^{-4}$ and $1.3x10^{-1}$) were performed in this study. Three samples were tested at each three strain rates for both directions. Typical microstructure of the composite in the fiber plane is shown in Fig. 4.2. As received composite was in the form of plate, 15mm in thickness. Plate-like samples normal and parallel to the fiber plane were cut using diamond saw in order to core drill cylindrical specimens corresponding longitudinal and transverse directions.

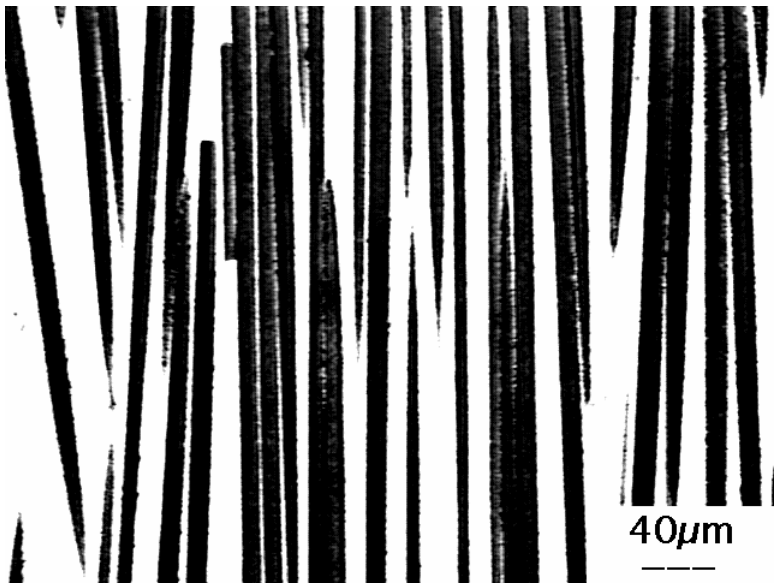

Fig.4.2. Optical micrograph of the untested FP/Al in the fiber plane.

4.2 Testing Methods and Microscopy

Quasi-static and high strain rate compression tests on Mg MMC were conducted on cylindrical core drilled specimens (Fig. 4.3), 6.7 mm in diameter and 12.8 mm in length, through and normal to the fiber plane. Quasi-static tests were conducted using a displacement controlled SHIMADZU AG-I universal tension-compression test machine at cross-head speeds of 0.1, 3.2, 100 and 500 mms^{-1} corresponding to the strain rates of

$1.3x10^{-4}$, $4.16x10^{-3}$, $1.3x10^{-1}$ and $6.51x10^{-1}$ s^{-1}. For each quasi-static strain rate 5 samples were tested for both directions.

High strain rate tests were conducted using a compression Split Hopkinson Pressure Bar (SHPB) at University of Delaware by Res. Asst. Alper Taşdemirci, comprising three 19mm diameter Inconel-718 bars: a striker bar (724mm in length), an incident bar (3660mm in length) and a transmitter bar (1830mm in length). The characteristic time window is ~290μs and the repeated loading of the specimen in between the bars is prevented due to the shorter transmitter bar. The striker bar produces a constant amplitude elastic compressive wave in the incident bar; this wave propagates down the bar to the bar/specimen interface where it is partly reflected back into the incident bar as a tensile pulse and partly transmitted to the transmitter bar as a compressive pulse. The strain rate ($\dot{\varepsilon}$), strain (ε) and stress (σ) in the specimen are given by;

$$\dot{\varepsilon}(t) = -\frac{2C_b}{L_s}\varepsilon_r(t) \tag{4.1}$$

$$\varepsilon(t) = -\frac{2C_b}{L_s}\int_0^t \varepsilon_r(t) \tag{4.2}$$

$$\sigma(t) = \frac{E_b A_b}{A_s}\varepsilon_t(t) \tag{4.3}$$

where, C_b is the elastic wave velocity in the bar, L_s is the sample length and A_s and A_b are the sample and bar cross-sectional areas respectively. ε_I, ε_r and ε_t are incident, reflected and transmitted strains measured from strain gages on the bar, respectively.

In quasi-static testing the stress (σ) and strain (ε) values were calculated from displacement *vs.* load graph of the specimen using following relations.

$$\varepsilon = \delta_{sp} / l_{sp} \tag{4.4}$$

$$\sigma = F / A_{sp} \tag{4.5}$$

In these equations ε, δ_{sp}, F, l_{sp}, and A_{sp} are strain, displacement at the sample, applied load, the length of the sample and cross-section area of the sample, respectively. It is well known that all testing machines and auxiliary apparatus deflect under the load during any test. Therefore, the displacement during compression testing is the sum of the machine (δ_m) and specimen (δ_s) displacements. If v_{CR} is the cross-head speed of the testing machine and t is the time, the total displacement may be written as

$$v_{CR}t = e_s l_s + \frac{p}{K} \tag{4.6}$$

where s refers to the specimen, P is the instantaneous load and K is the Instron machine stiffness. The second term of Equation 4.6 represents the machine displacement at an instantaneous load. By arranging Equation 4.6, specimen strain is written as

$$e_s = \frac{1}{l_s}(v_{CR}t - \frac{p}{K}) \tag{4.7}$$

For the studies cross-head speeds the machine compliance was calculated using Equation 4.7.

The strain-rate is calculated from the proportion of crosshead speed (v_c) and the lentgh of the specimen (l_{sp}) where the units of $\dot{\varepsilon}$, v_c and l_{sp} are sec^{-1}, mm/sec and mm, respectively. (Eq 4.8)

$$\dot{\varepsilon} = \frac{v_c}{l_{sp}} \tag{4.8}$$

An oil-based lubricant was used to reduce friction between the specimen and testing apparatus in quasi-static and high strain rate testing.

Figure 4.3 Untested cylindrical sample in axial direction

The compression testing through axial direction was conducted using high strength steel caps in order to prevent the brooming of the composite, leading to inaccurate material property. Figures 4.4 (a-c) show a steel cap and the insertion of a sample into the caps.

(a) (b) (c)

Figure 4.4 a) Steel tap used in axial tests ,b and c) insertion of test samples into the steel caps

Microscopic analyses were performed on the tested composite samples using optical microscopy and a Philips XL30-SFEG scanning electron microscope (SEM) with an Energy Dispersive X-ray (EDX) analyzer. Polished samples surfaces were etched with Kroll's reagent (3 cm^3 of HF and 6 cm^3 of HNO_3 in 100 ml of H_2O).

4.3 SHPB Apparatus

The schematic presentation of the SHPB set-up at the University of Delaware (UD) is shown in Figure 4.5. The apparatus consists of three major parts; gas gun assembly, bars and electronic data measuring system.

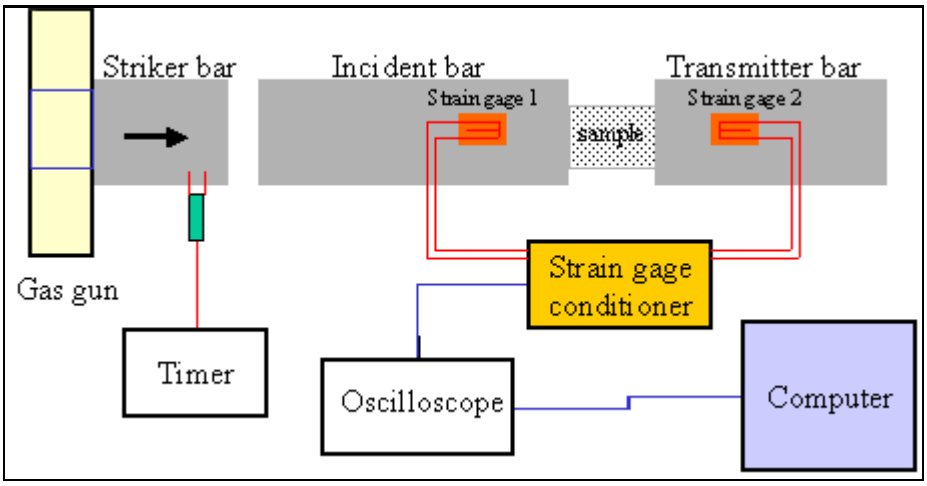

Figure 4.5. Schematic presentation of the SHPB set-up

The gas gun assembly consists of pressure chambers which facilitate the impact of striker bar on to the incident bar. For that purpose, the inner and outer pressure chambers of the gas gun assembly are pressurized by nitrogen gas from a high pressure gas cylinder before each test. When the inner gas chamber pressure is released by the valve, the outer chamber pressure is emptied in to the barrel. This action moves the striker bar horizontally on Teflon rings until it impacts the incident bar end. This impact initiates a constant amplitude compressive elastic wave in the incident bar. The amplitude of the wave is directly proportional to the striker bar .

In each test, v_o is measured just before impact of the striker bar on to the incident bar by the help of two infrared beams set four inches apart. A timer connected to the infrared beam system records the time of travel of the striker bar between the beams. The compressive elastic wave developed at one end of the incident bar propagates down the bar until it reaches the bar/specimen interface where it is partly

reflected as a tension wave back to the incident bar and partly transmitted as the compression wave through the transmitter bar. The relative magnitudes of the reflected and transmitted pulses are a function of the difference in acoustic impedance of the bar and the specimen materials. The SHPB bars at UD are made of Inconel 718 alloy. The lengths of the available striker bars are 362 and 724 mm and the lengths of the incident and transmitter bars are 3658 and 1440 mm. All bars' diameters are the same, 19 mm.

The electronic measuring system consists of two major devices, a strain gage conditioner and oscilloscope. The strain gage conditioner is used to form a full bridge strain gage circuit on the bars in order to measure the longitudinal strain involved in each test. The Gage 1 and Gage 2 of Figure 4.4 are, therefore, used to measure strains on incident and transmitter bars, respectively. Gage 1 measures both incident and reflected pulses and Gage 2 measures only transmitted pulse. An oscilloscope (Fluke, PM3394A) connected to the strain gage conditioner is used to monitor and record the strain gage bridge circuit voltages during each experiment. Besides these devices, a micro-computer and a plotter are provided in order to conduct data reduction (calculation of stress and strain) process and to get hard copy of wave forms, respectively.

Before each test, the specimen size, length and diameter were measured for use in calculating strain, strain rate and stress. After obtaining strain measurements from incident and transmitter bars, the data reduction process was applied. The strain in the specimen was calculated using the relation

$$\varepsilon_s = -\frac{2C_b}{L_s}\left(\frac{2\int \varepsilon_r(V)dt}{G_g K_g V_e(1+\varphi)}\right) \tag{4.9}$$

where G_g, K_g, V_e and φ are the strain gage conditioner gain, strain gage factor, excitation voltage of the strain gage bridge and Poisson's ratio of the bar material, respectively. The above formulation is only valid for a "Full-Bridge" strain gage circuit. Similarly the stress in the specimen was calculated using

$$\sigma_s = \frac{A_b}{A_s} E_b\left(\frac{2\varepsilon_t(V)}{G_g K_g V_e(1+\varphi)}\right) \tag{4.10}$$

The values of G_g, K_g, and V_e were 200, 2.07 and 9.73V, respectively. The elastic wave velocity of the bar was calculated as follows. An additional strain gage was mounted on the transmitter bar and the distance between the two gages was precisely measured. SHPB tests were conducted by bringing incident and transmitted bars together without any specimen between them so that all the incident wave was transmitted to the transmitter bar. The two recorded transmitted waves were used to calculate wave velocity by shifting one of them relative to the other on the time scale. The distance between two strain gages was divided by the shift time to calculate exact value of the elastic wave velocity of the bar. The elastic wave velocity of the present bar was calculated to be 4960ms^{-1} by applying above procedure. The modulus of the bar was calculated using

$$E = C_s^2 \rho \tag{4.11}$$

where ρ is density of the bar. The ρ for the material is given as 8190 kgm^{-3} and using this value the modulus was calculated to be 201.4GPa.

CHAPTER 5

Results

5.1 Microstructural Analysis of FP fiber reinforced Mg MMC

The EDAX analysis of the grains of Mg in the composite as shown in Figure 5.1. shows the presence of Zn element as the solid solution in the matrix. The EDAX analysis of the secondary phase which decorated the grain boundaries has confirmed a quaternary alloy of Mg-Zn-Al-Ce (Figure 5.4). The presence of Al mainly resulted from the FP fiber which was reduced by Mg. It is also noted that Ce is found in the secondary phase.

The results of EDAX line scan analysis of a cross-section of the composite contained a fiber and precipitates in it are shown in Figures 5.2(a-d). The concentration of main element of the matrix decreases at the cross-sections of small precipitates and is nil in the cross-section of the FP fiber as shown in Figures 5.2(a) and (c). In Figure 5.2(a) the O concentration is seen only through the FP fiber cross-section. Figure 5.2(d) further confirms the presence of element Zn both in matrix and precipitates. Al is found both in the precipitate and in fiber (Figure 5.2(a)). Figure 5.4(b) further confirms the presence of small amount of Ce solely in the precipitates.

It is also noted in Figures 5.2(c) and 5.3(a) that the Mg concentration becomes zero at some finite distance from the fiber matrix interfaces through the fiber site while Al concentration starts to increase at some finite distance away from the fiber matrix interface. These results were attributed to the reduction of the Al_2O_3 by Mg, leading the formation of MgO at the fiber matrix interface.

Figure 5.1 EDAX analysis of Mg grains.

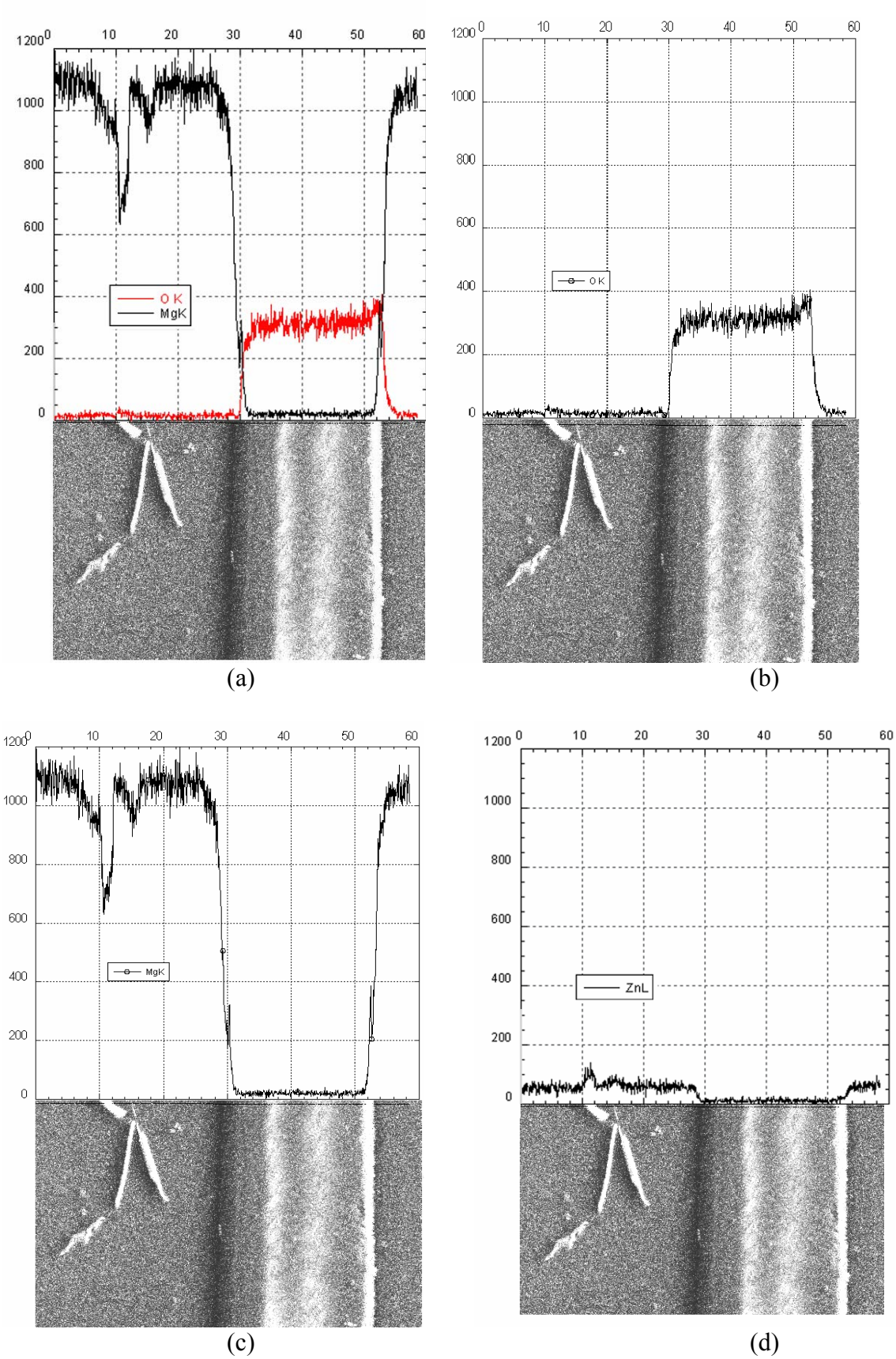

Figure 5.2 EDX Line scan of (a) Mg and O, (b) O, (c) Mg and (d) Zn through matrix, precipitates and fiber.

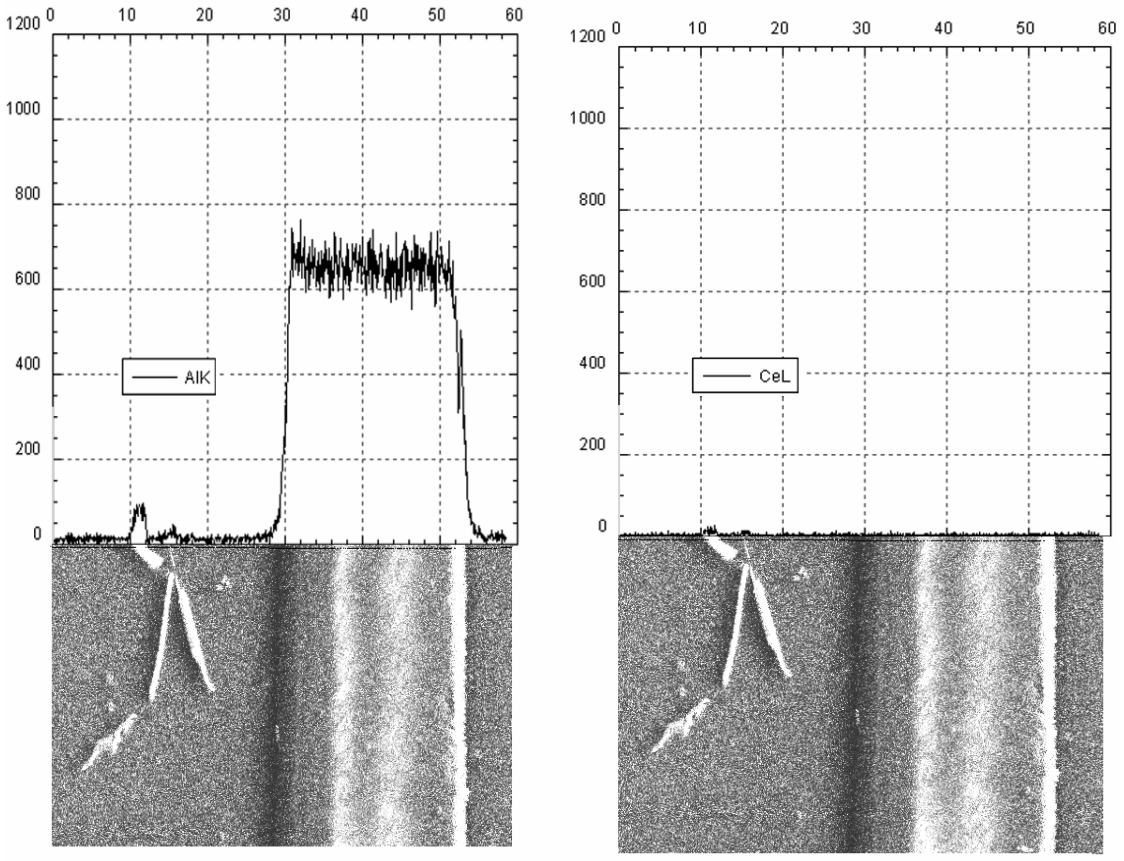

(a) (b)

Figure 5.3 EDX Line scan of (a) Al and Ce through matrix, precipitates and fiber.

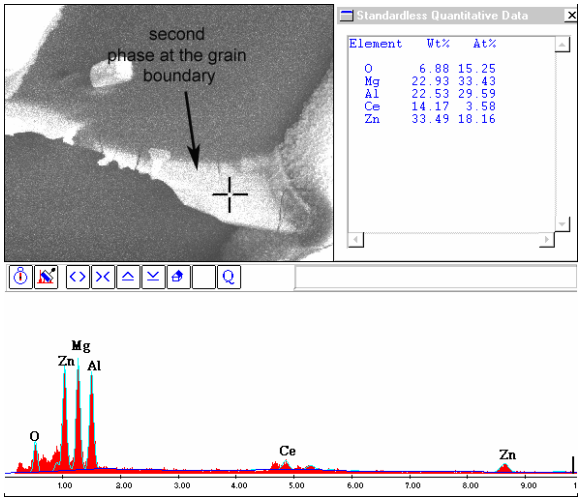

Figure 5.4 EDAX analysis of the secondary phase at the grain boundaries.

5.2 Compression behavior of FP fiber reinforced Mg MMC

5.2.1 Transverse Direction

An example of SHPB strain reading of the FP fiber reinforced Mg MMC specimen tested in the transverse direction and the corresponding stress and strain rate variation with strain are shown in Figure 5.5 and Figure 5.6 respectively. In Figure 5.5, the sudden increase in reflected wave and the corresponding decrease in transmitted wave show the failure of the sample as marked with arrow. For a specific test, the instantaneous strain rate also varied during deformation (Figure 5.6), from zero to final or failure strain, and therefore an average strain rate was calculated as

$$\dot{\varepsilon}_{avg} = \frac{1}{\varepsilon_f}\int_0^{\varepsilon_f} \dot{\varepsilon}\, d\varepsilon \qquad (5.1)$$

where, ε_f is the maximum strain.

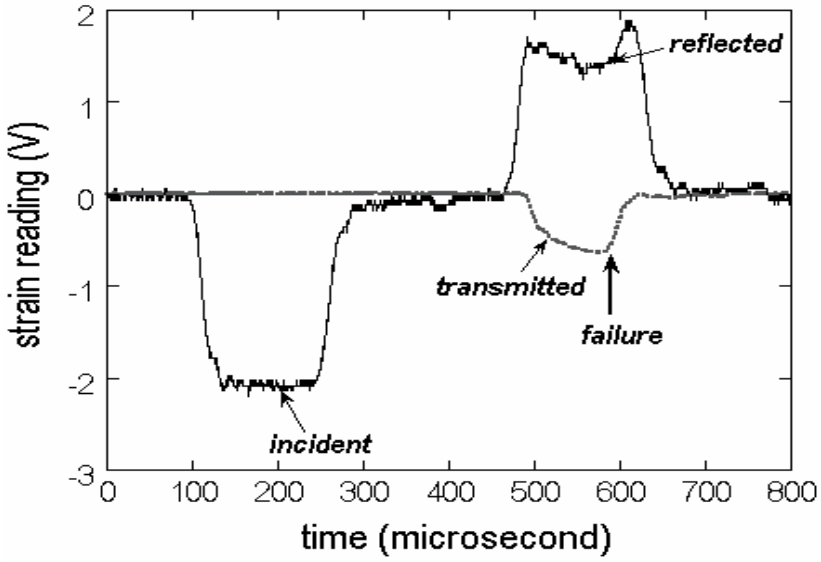

Figure 5.5. Strain reading of the specimen tested in the transverse direction

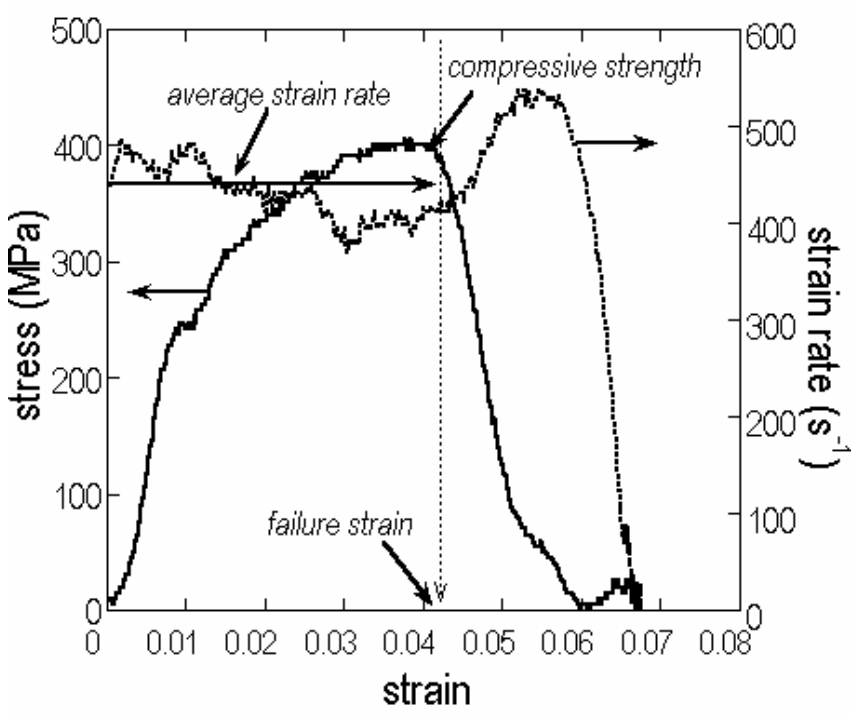

Figure 5.6. Stress and strain rate variation with strain of the specimen tested in the transverse direction

Typical quasi-static and high strain rate compression engineering stress-strain curves of the composite in the transverse direction are presented in Figure 5.7. The initial elastic region of each curve is followed by a region of inelastic deformation until about a maximum stress is reached after which sample fails by shear banding which will be elaborated later. The maximum stress and corresponding strain are considered as failure stress (marked by arrows in Figure 5.7) and failure strain. The effect of increasing strain rate is to increase flow stress and failure stress values of the composite as shown in Figure 5.8. The flow stress at 2% strain, for example, increases from 300 MPa to 350 MPa on the average, when the strain rate increases from quasi-static to high strain rate. Similarly, the failure stress increases from 350 MPa at quasi-static strain rates to 400 MPa at high strain rates. Increasing strain rate however decreases the failure strain (Figure 5.9). The failure strain at $1.3x10^{-4}$ s^{-1} is about 4%, while it decreases to about 3% when the strain rate is higher than $1.3x10^{-1}$ s^{-1}.

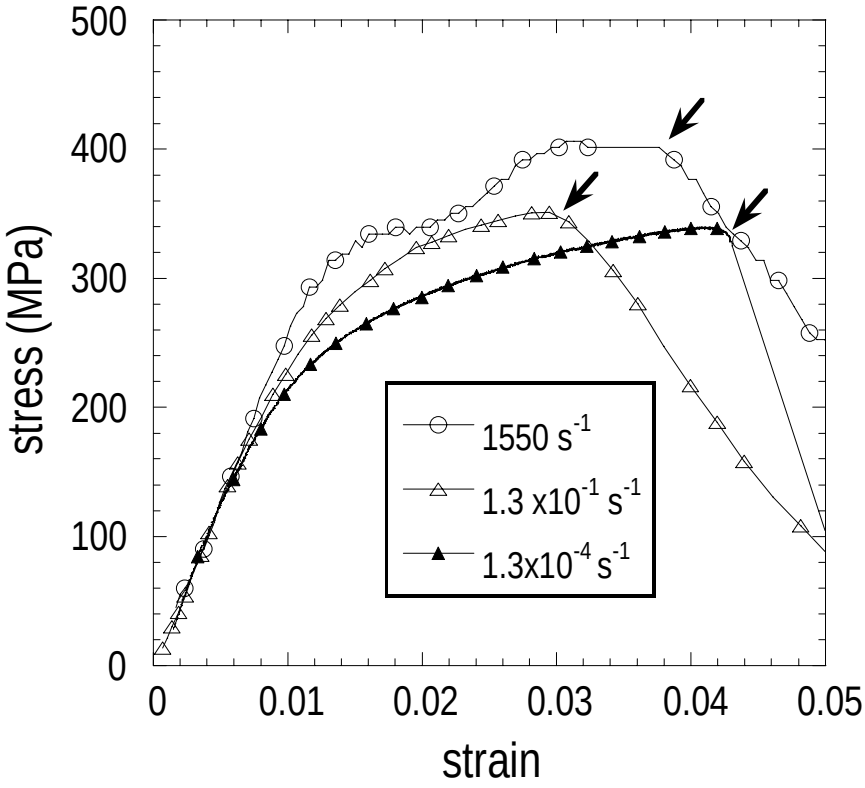

Figure 5.7. Engineering stress-strain curves of FP-Mg tested at transverse direction at various strain-rates.

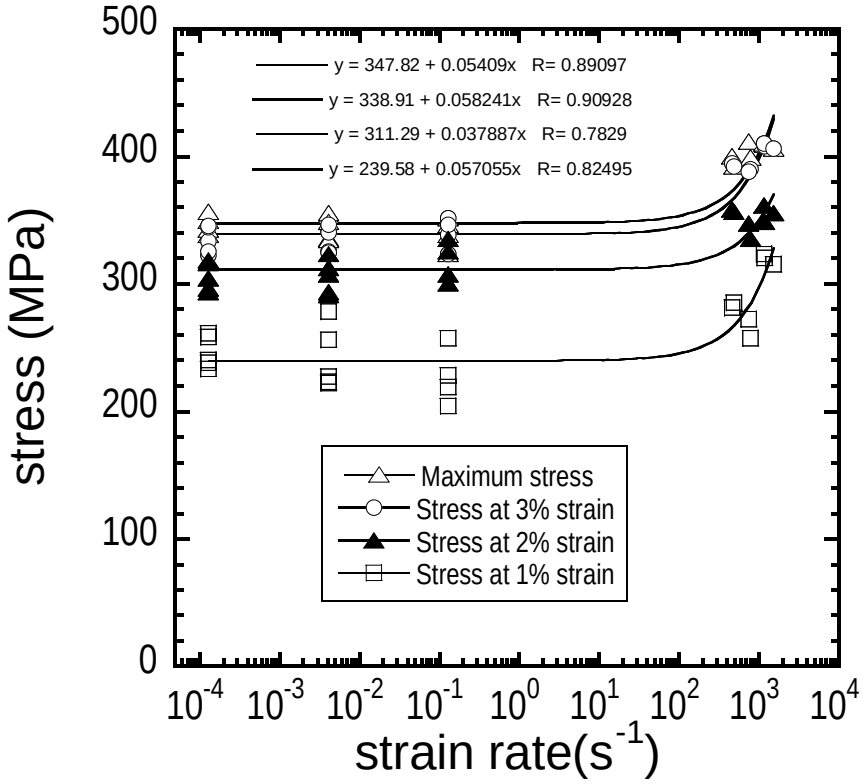

Figure 5.8 Failure stress via strain-rate plot of FP-Mg tested at transverse direction.

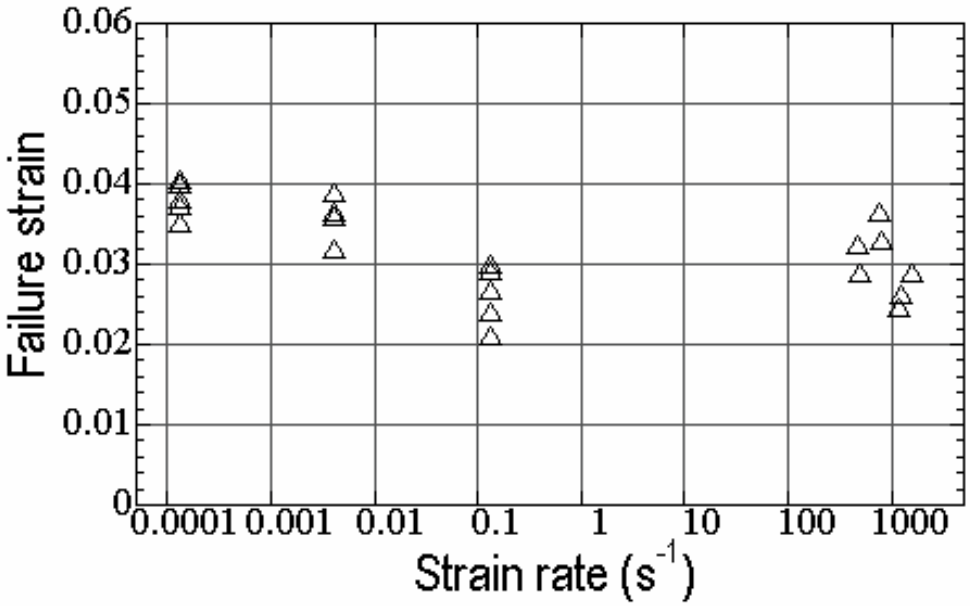

Figure 5.9. Failure strain via strain rate plot of FP-Mg tested at transverse direction.

5.2.2 Axial Direction

Testing of unidirectionally reinforced composites in the longitudinal direction is somewhat problematic in that the deformation and failure modes are strongly dependent upon the precise loading configuration. Initial tests were conducted using three different configurations; (a) without steel caps, (b) with steel caps (Figure 5.10) and (c) with steel caps and dog-bone shaped specimen. Specimens tested without end-caps failed prematurely by axial splitting and brooming occurring at one of the ends of the specimen (Figure 5.11(a)). The use of dog bone shape specimen also resulted in premature failure of the composite (Figure 5.11(b)) by forming splitting near to one of the end caps. The highest maximum stress was obtained cylindrical samples tested with end caps (Figure 5.12) and therefore further testing of the composite was therefore continued with end-caps.

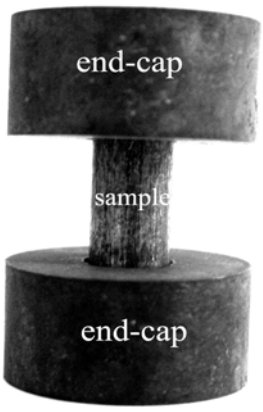

Figure 5.10. Test sample with end-caps.

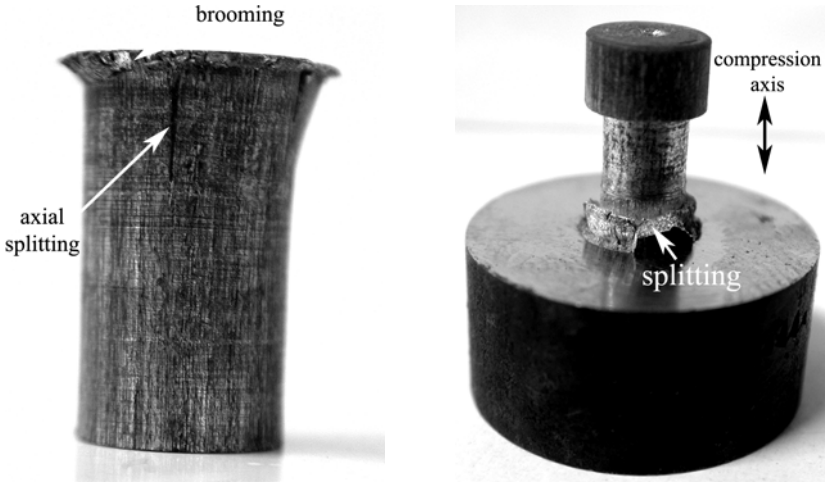

(a) (b)

Figure 5.11. Failure in the axial direction of the composite (a) without end-caps and (b) dog bone shape with end caps.

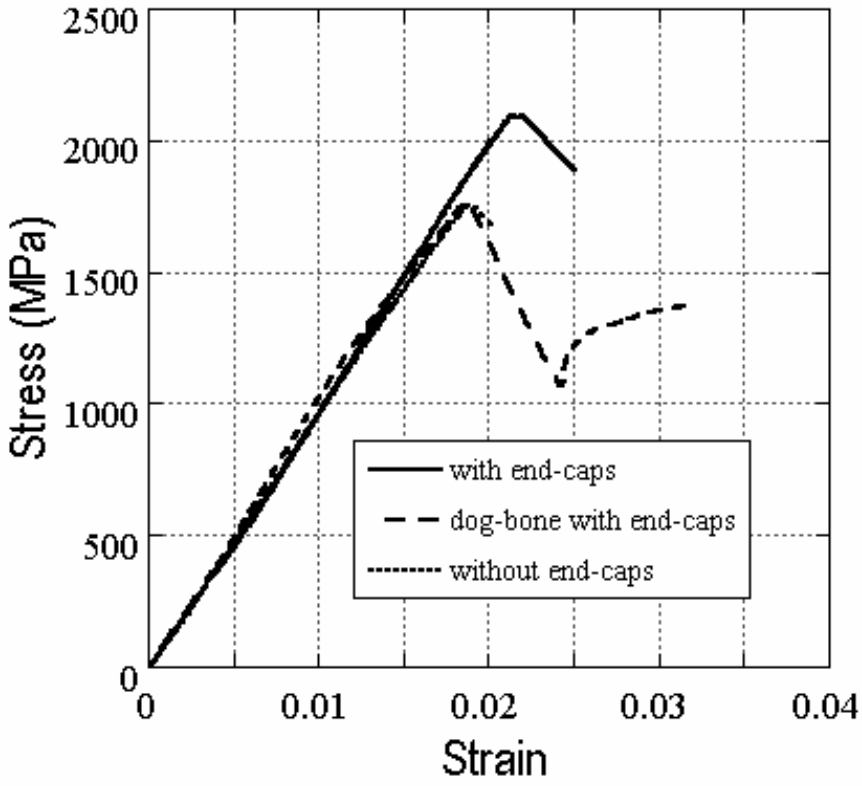

Fig. 5.12 Typical quasi-static ($1.3x10^{-4}s^{-1}$) stress-strain curves of composite samples with end-caps, dog-bone shape with end-caps and without end-caps.

Typical high strain rate stress-strain rate vs. strain curves of the composite is shown in Figure 5.13. The stress initially to a maximum while the strain rate decreases gradually until the maximum stress is reached. Thereafter the strain rate increases as a result of kink band propagation which will be considered later in this chapter. An average strain rate was also calculated in the axial direction for each test.

Typical stress-strain curves of the composite until maximum stress in the longitudinal direction at high and quasi-static strain rates are shown in Figure 5.14. It can be noted that the stress-strain curves of the composite in axial direction are almost linear with a compression modulus of about 100 GPa. Figure 5.15(a) and (b) show the variation of failure stress and strain with strain rate, respectively. Despite the large variations in failure stress values (1700-2500MPa), the composite in the longitudinal direction shows almost no strain rate dependency in failure stress. Although failure stresses are slightly higher on the average at the lowest quasi-static rate, $1x10^{-4}s^{-1}$. The failure strain is also slightly affected by the strain rate as shown in Figure 5.14(b). The failure strain is 2.5% at $10^{-4}s^{-1}$ and it decreases to 2% on the average at $10^{3}s^{-1}$ strain rates.

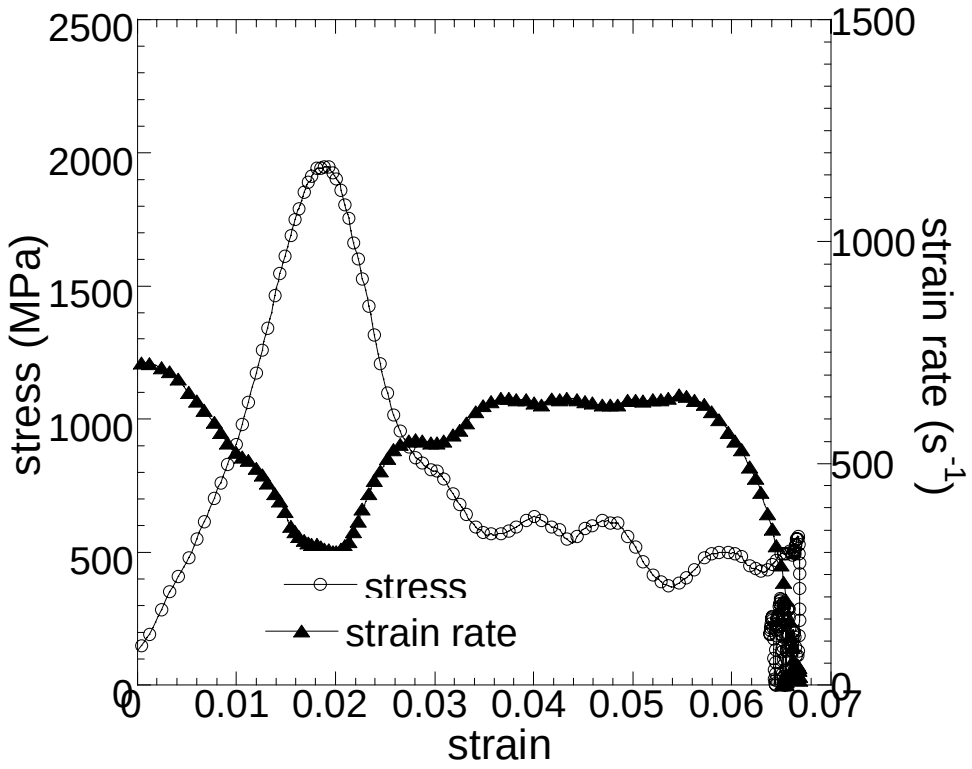

Figure 5.13 Typical high strain rate stress-strain rate (~500 s^{-1}) and strain curves of the composite in axial direction.

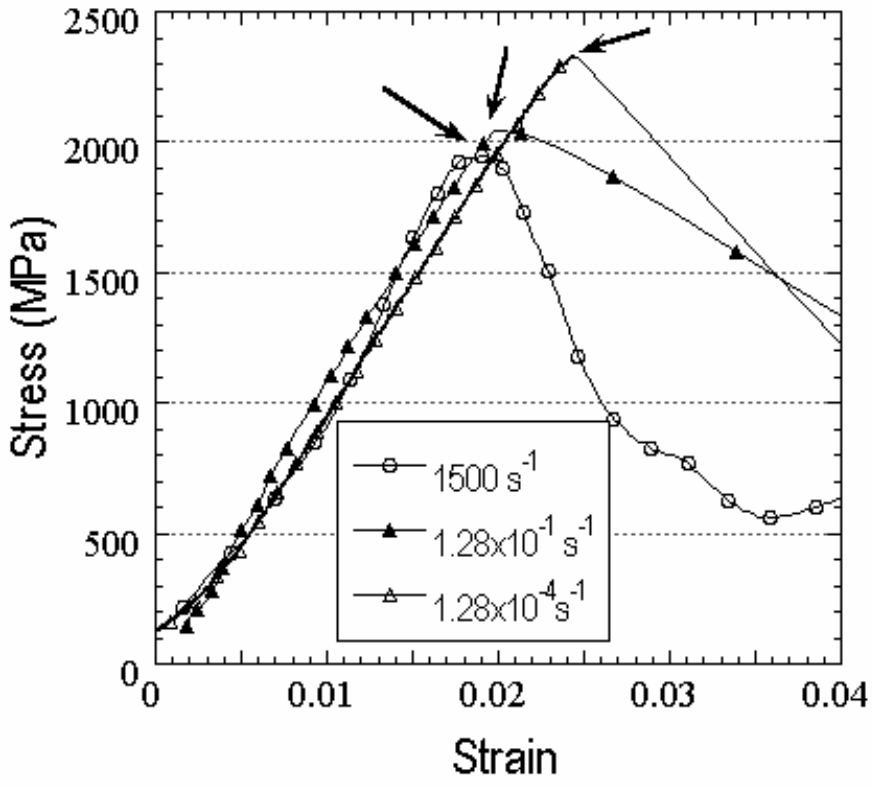

Figure 5.14 Engineering stress-strain curves of FP-Mg tested at longitudinal direction at various strain-rates.

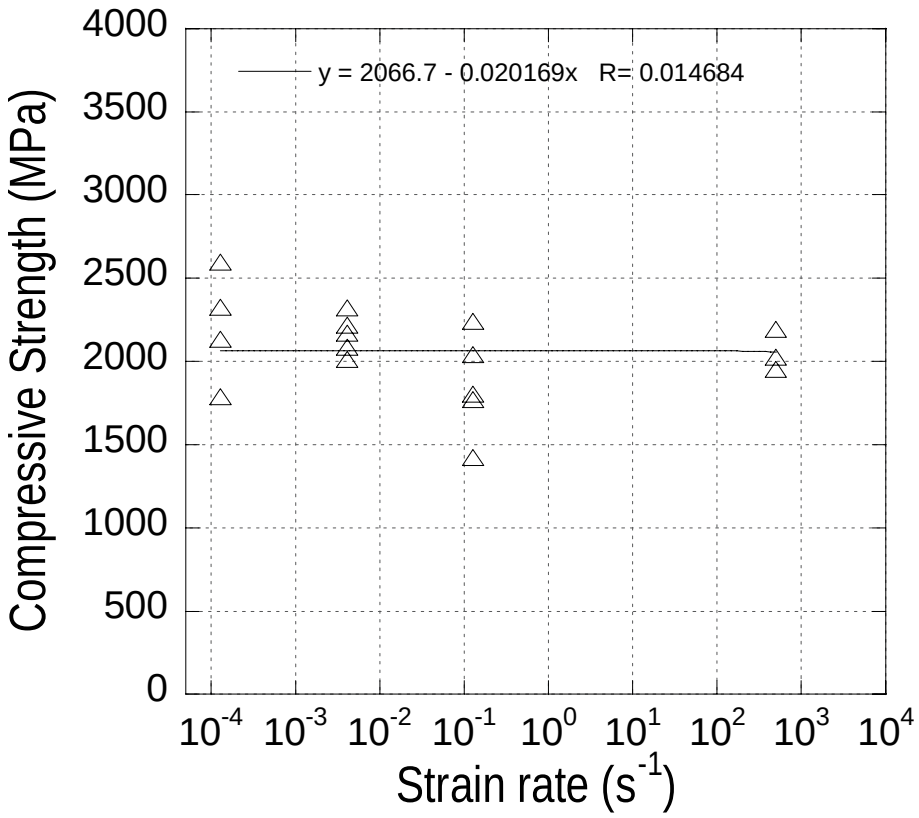

(a)

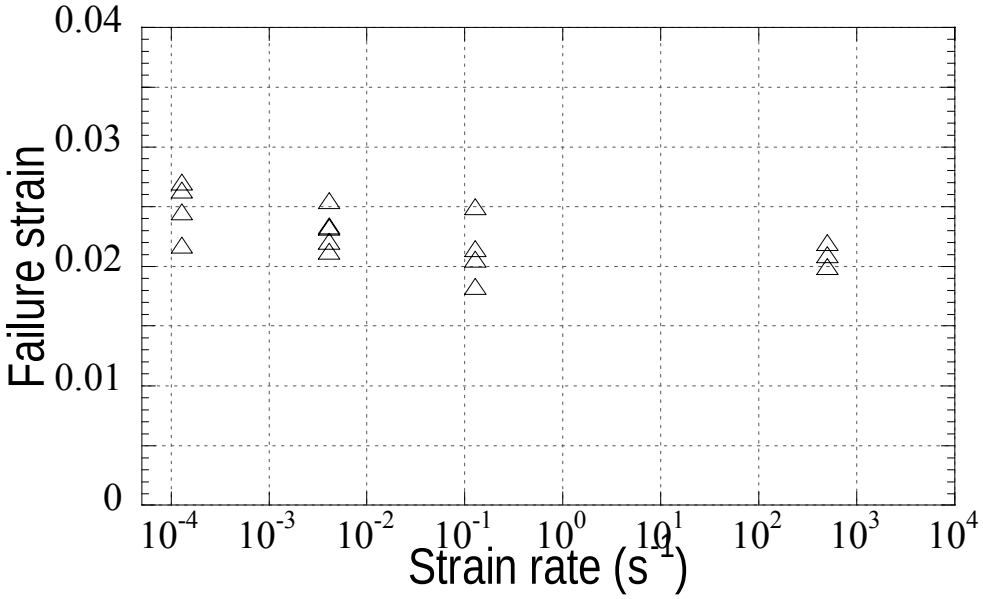

(b)

Figure 5.15. Variation of (a) failure stress and (b) failure strain with strain rate

5.3 FP fiber reinforced Al MMC

FP alumina fiber reinforced unidirectional Al MMC was previously tested in transverse and axial directions by Guden and Hall [64]. The composite showed a strain rate dependent compressive stress in both directions. Additional tests at quasi-static strain rates were conducted in order to confirm the previous results and provide more data for accurate prediction of strain rate dependent flow and compressive strength. Figure 5.16 show the typical quasi-static stress strain curve in transverse direction. The stress-strain curve of Mg MMC in the transverse direction at the same strain rate is also shown in the same figure for comparison purpose. Similar to Mg MMC, Al MMC in the transverse direction failed by shear banding but at a higher strain (6%). Also noted in the same figure Mg MMC shows higher flow stress as compared with Al MMC in the transverse direction. The following figure, Figure 5.17, compares the strain rate dependent flow stresses of both composites at constant strain. It is noted in the same figure, the present results of flow stresses of Al MMC and the previous results show well agreements. Although both composites in the transverse direction show strain rate dependency in flow stress, Mg MMC show a higher strain rate dependency. The strain rate dependency in compressive strengths in the MMCs is however very similar as depicted in Figure 5.18.

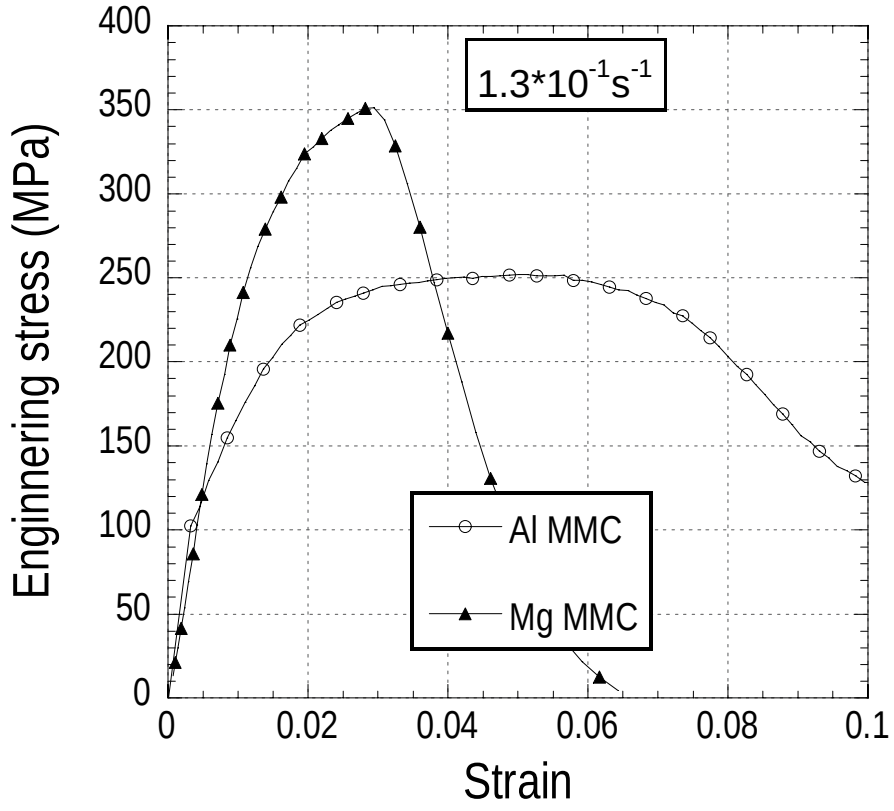

Figure 5.16 Compression stress strain curves of Al and Mg MCC in transverse directions at the same strain rate

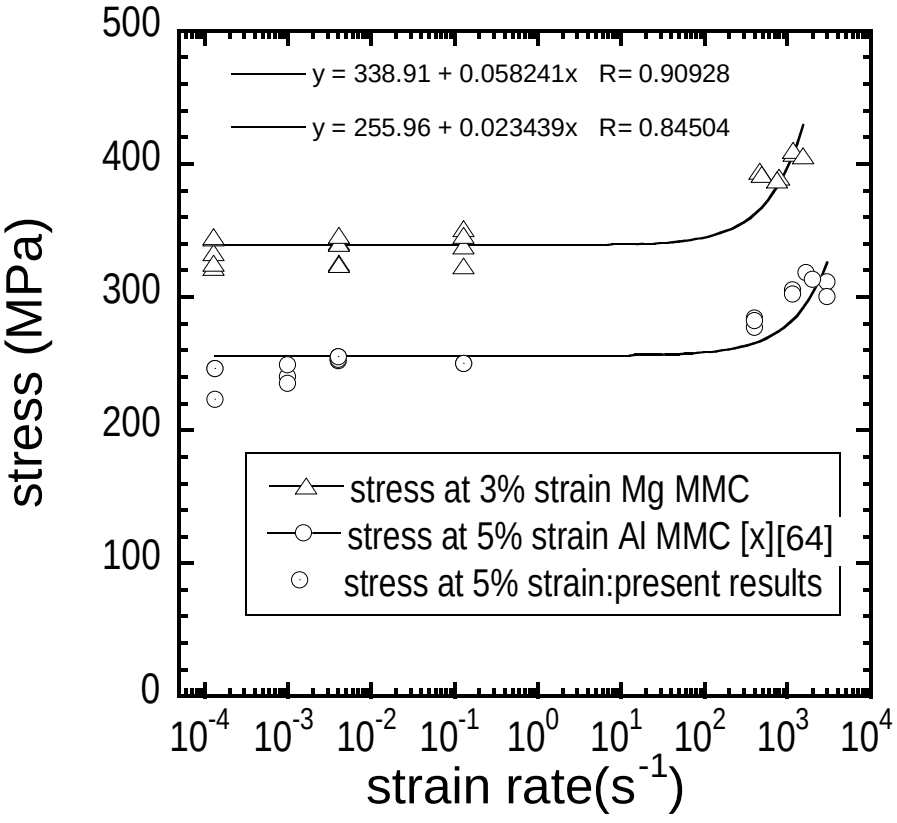

Figure 5.17 Stress strain curve for FP-Al sample tested at transverse direction.

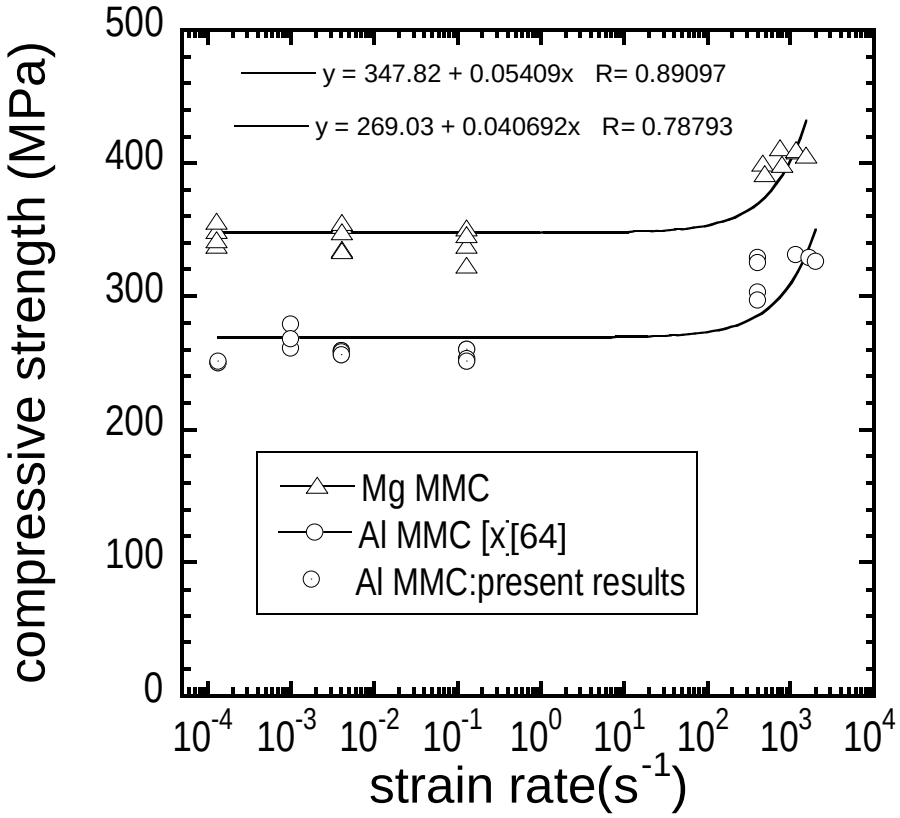

Figure 5.18. Failure stress via strain-rate curve for FP-Al sample tested at transverse direction.

In the axial direction FP-Al MMC composite shows lower compressive strength (~1800 MPa) than FP Mg MMC at quasi-static strain rates as shown in Figure 5.19. At high strain rates >100 s^{-1}, due to higher strain rate sensitivity Al MMC shows higher compressive strength than Mg MMC.

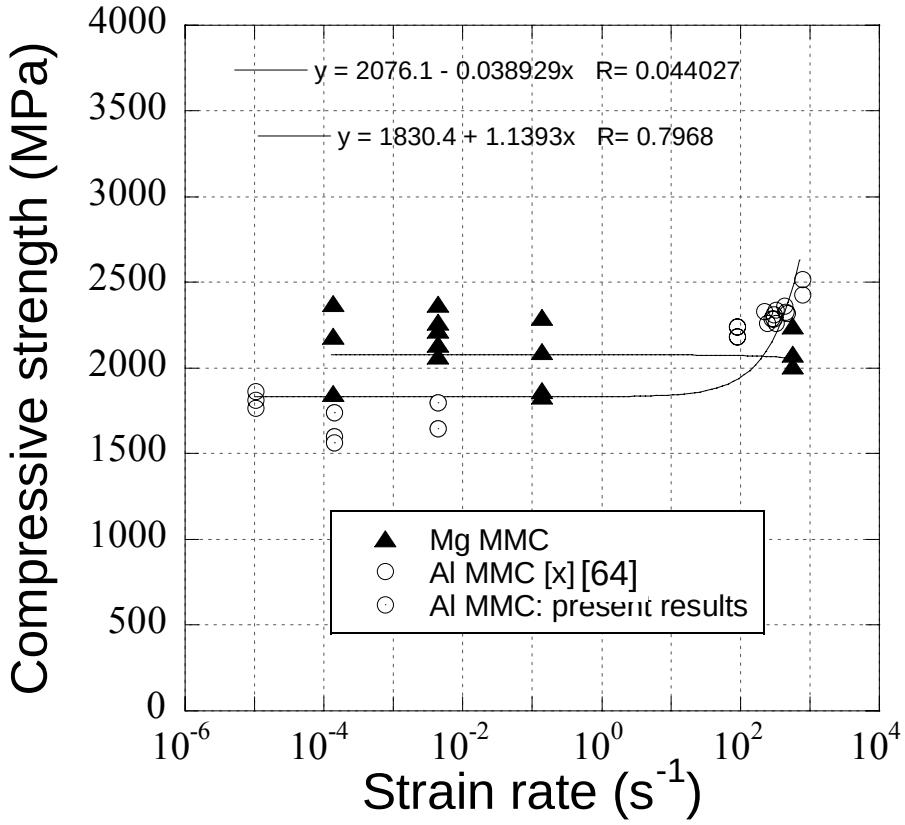

Figure 5.19 The variation of compressive strength with strain rate

5.4 Deformation modes and Failure

5.4.1 Transverse direction

The microstructures of the polished cross-sections of failed samples tested at various strain rates are shown in Figures 5.20(a), (b), (c) and (d). Twinning is seen at all samples although the number of twins decreases as the strain rate increased and/or as the failure strain decreases. The number twins were counted form the micrographs corresponding to an area of $5x10^{-2}$ mm^2. The twin concentration is shown in Figure 5. 21 as function strain rate. It is seen that twin concentration decreases as the strain rate increases. Note the failure strain of the samples tested at different strain rates is different and therefore Figure 5.21 does not show the effect of strain rate on the number of twins formed. In order to see the effect of strain on the twin formation at a constant strain rate, samples were deformed until about 0.5,1, 1.5 and 2 % strains and in these samples the number of twins was counted. In Figure 5. 22 the increase of twin density is show as

function of strain for a sample deforming at $1.3x10^{-4}$ s^{-1}. It is seen that the twin density also increases with increasing strain rate.

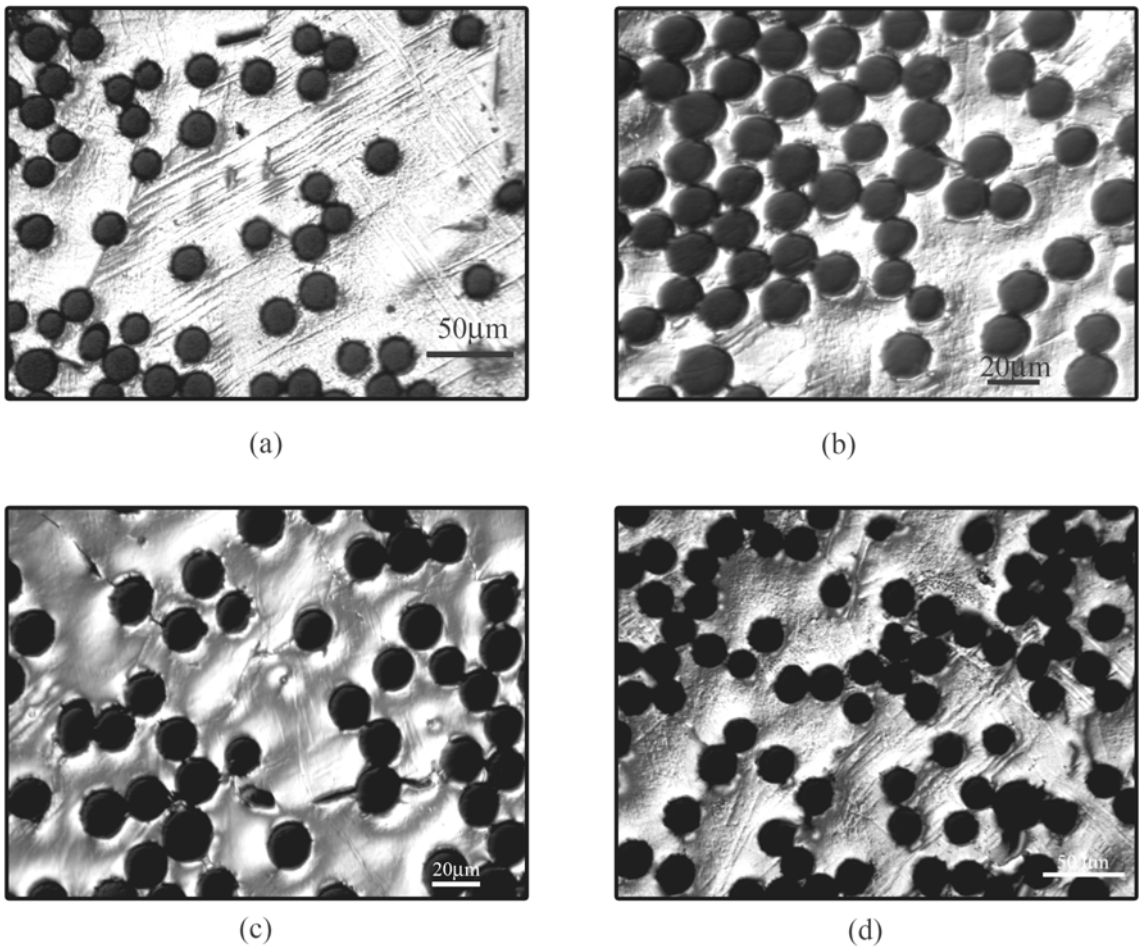

Figure 5.20 Micrographs taken from 100 µm away from the fracture surface of deformed samples at various strain-rates and failure strains a)$1.3x10^{-4}$ s^{-1} at 0.038 strain, b)$4,1x10^{-3}$ s^{-1} at 0.032 strain c)$1.3x10^{-1}$ s^{-1} at 0.029 strain d) 750 s^{-1} at 0.0246 strain.

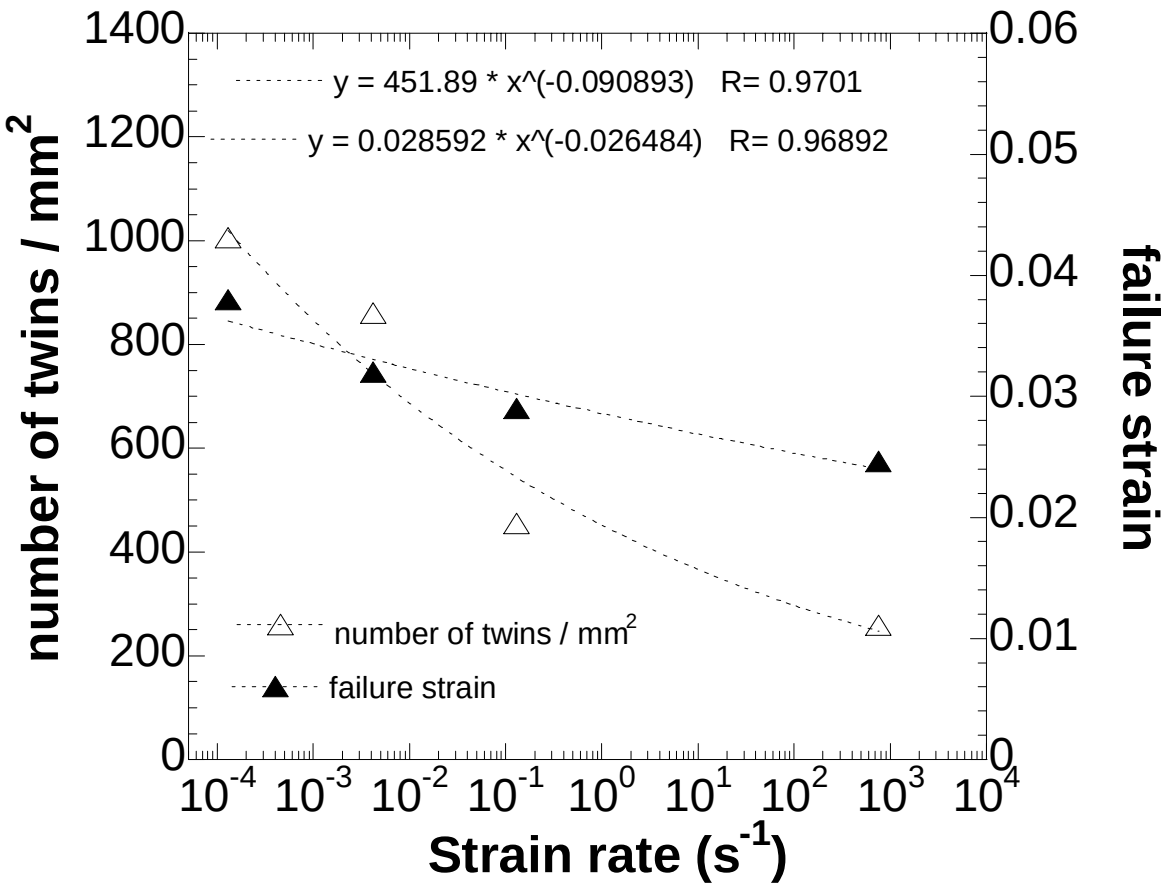

Figure 5.21 Twin concentration and failure strain vs. strain rate.

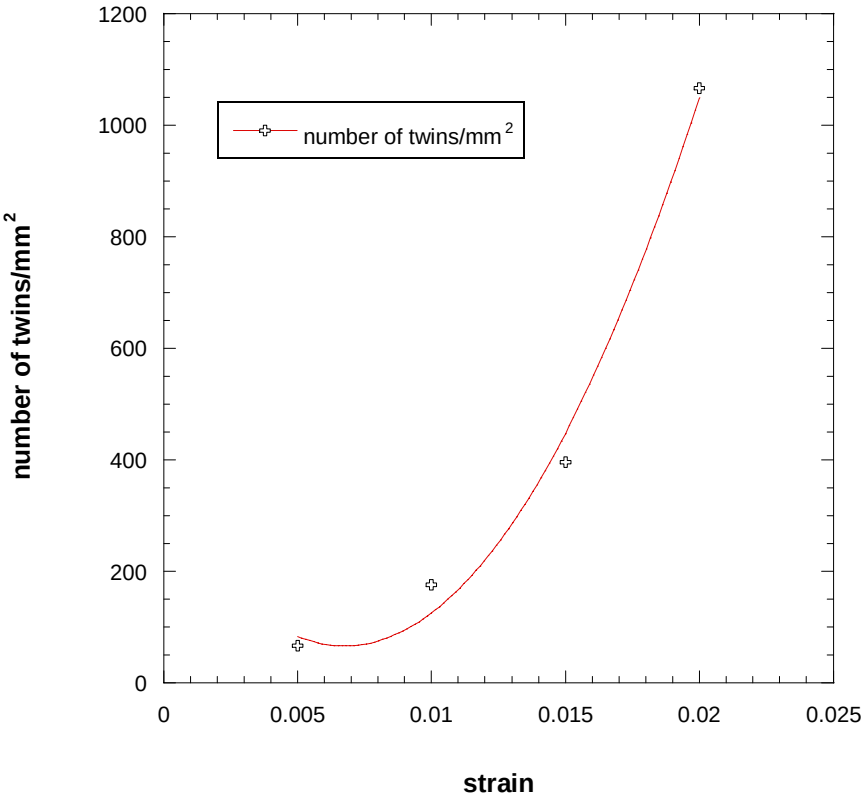

Figure 5.22 Twin density vs. strain at 1.3×10^{-4} s^{-1}

It was observed microscopically that twins formed within individual grains at interfaces, including fiber/matrix interface (Figure 5.23(a) and (b)). Extensive twinned regions are also seen between the fibers as shown in Figure 5.23(c). Figure 5.23(d) also shows the twins accommodation on a grain boundary.

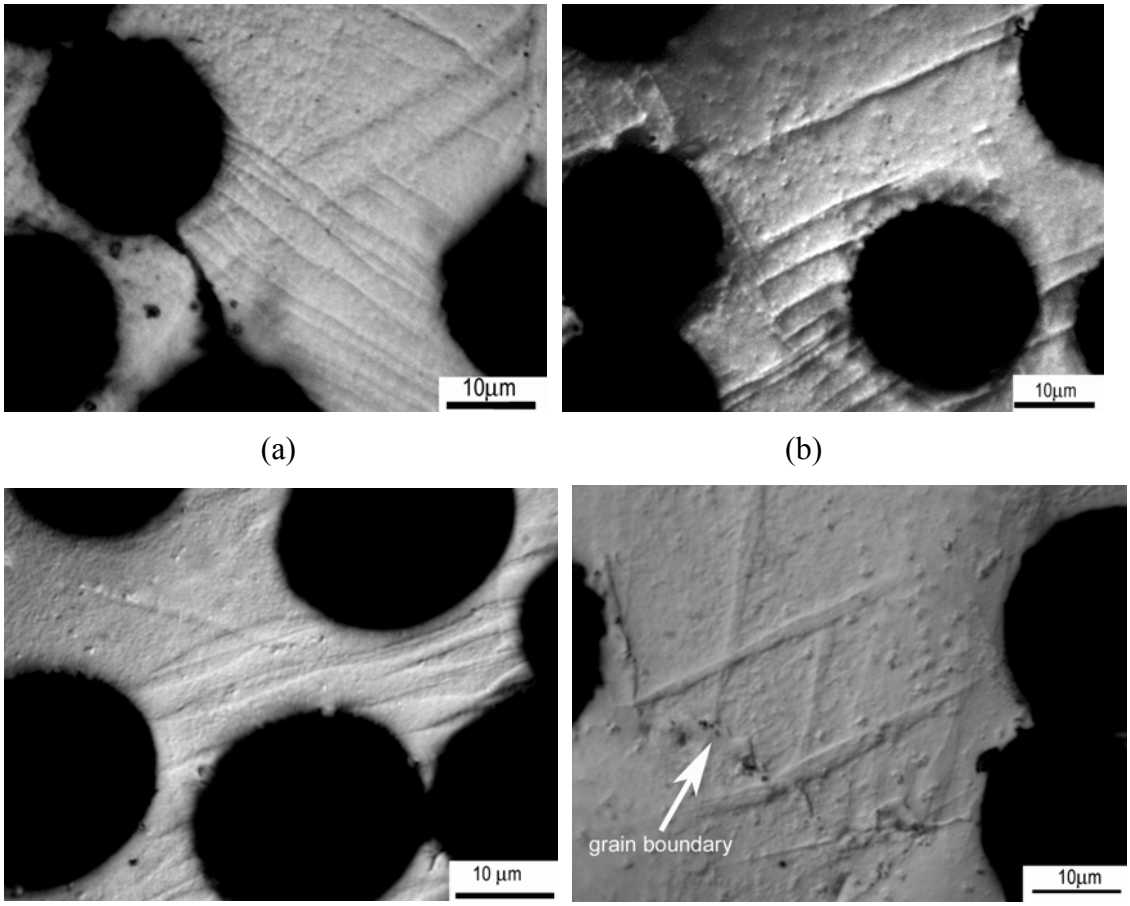

(a) (b)

(b) (d)

Figure 5.23. Twins in samples tested at $1.3x10^{-4}s^{-1}$ and in samples tested at 750 s^{-1} (c) and (d).

The failure mode of the samples tested in the transverse direction, at quasi-static and high strain rates was through shear of the matrix, 45° to the compression axis as shown in Figure 5.24. In order to differentiate damage accumulation in the composite at quasi-static and dynamic strain rates, the fracture surfaces of the samples tested at different strain rates were analyzed. Failed composite samples at quasi-static and

dynamic strain rates were also cut and material graphically prepared for microscopic observations.

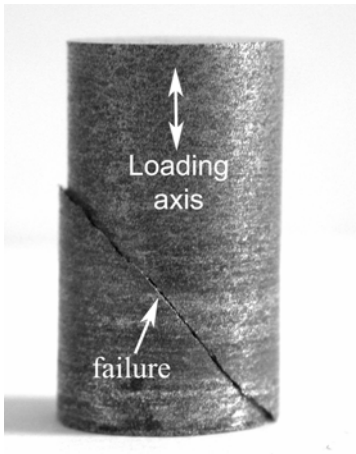

Figure 5.24 Failed compression test sample tested at $1.3x10^{-4}s^{-1}$.

Figures 5.25(a) and (b) show the fracture surfaces of the samples tested at quasi-static and high strain rates, respectively. The presence of higher number of fibers on the fracture surface of quasi-statically tested sample as compared with high strain rate tested sample confirm the relatively higher ductility of the samples tested at quasi-static strain rates. Figure 5.26 (a) through (d) show sequentially the polished and etched cross-sections of the failed samples at various strain rates along the failure sites. Excessive deformation in the form of shear band near the failure surface is clearly seen in the samples deformed at low strain rates shown in Figure 5.26(a) and (b). At high strain rates the shear banding is less produced (Figure 5.26(c) and (d)). These observations have also confirmed the failure mode of shear banding, 45 ^{o} to the loading axis. Figure 5.26 (a) and (b) also show the crack path following the fiber/matrix interface as the debonded and deattached fibers from the surface, while debonding of the fibers are less produced in the samples tested at higher strain rates as seen in Figure 5.26(c) and (d).

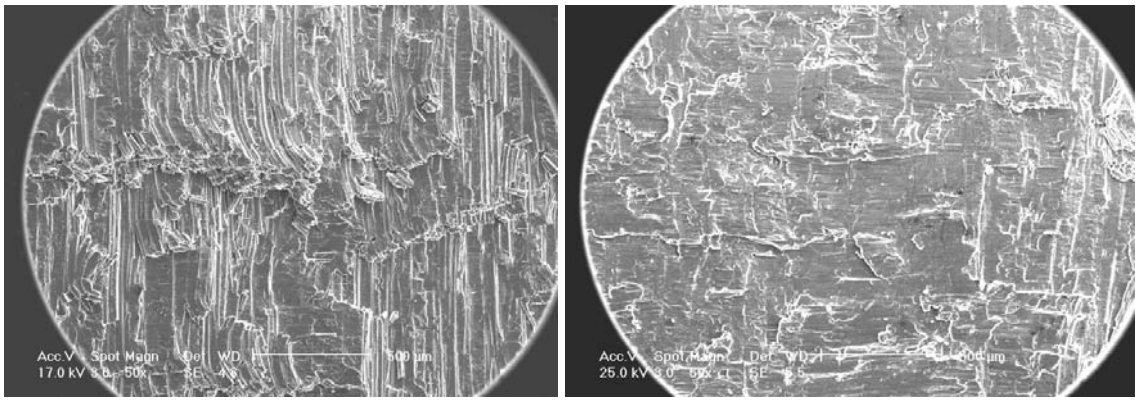

(a) (b)

Figure 5.25 Fracture surfaces of samples tested in various strain rates (a) $1.3x10^{-4}$ s^{-1} (b) 750 s^{-1}.

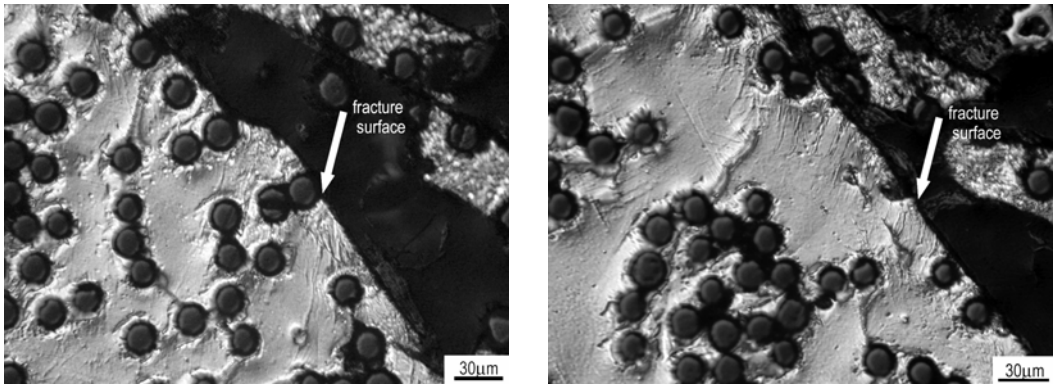

(a) (b)

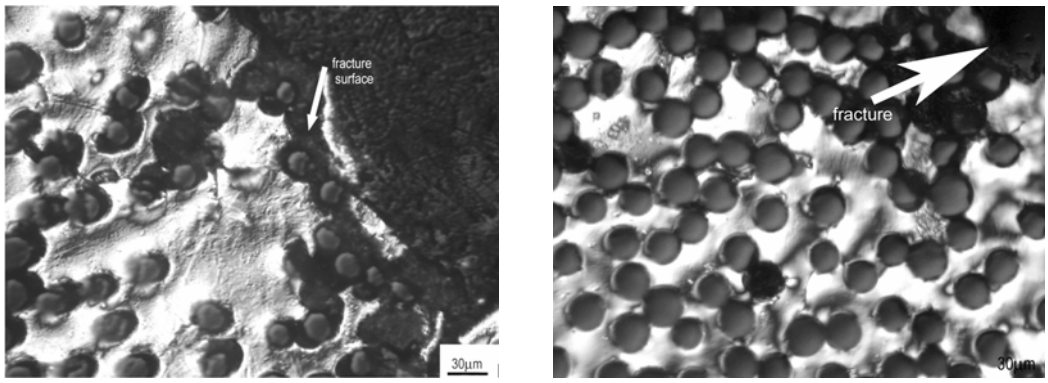

(c) (d)

Figure 5.26. Polished and etched cross-sections of the failed samples testes at a) $1.3x10^{-4}$ s^{-1}, failure strain of 0.038; b) $4.1x10^{-3}$ s^{-1}, failure strain of 0.032; c)$1.3x10^{-1}$ s^{-1}, failure strain of 0.029 and d) 750 s^{-1}, failure strain of 0.0246

Figures 5.27(a), (b) and (c) show the SEM micrographs of the quasi-statically deformed sample microstructure at increasing magnifications. In Figure 5.27(a) the highly deformed region next to the failure composing of twins and Figure 5.27(c) shows

the dynamically recrystallized (DRX) grains next to failure. The twin intersections at the grain boundaries were also observed to fracture the grain boundary precipitates as depicted in Figure 5.27(d). Similar to the quasi-statically tested samples, samples of high strain rate (750 s^{-1}) formed, although narrow, a highly deformed region next to the failure with the DRX grains in it (Figure 5.28(a)). The grain boundary precipitate cracks of twin intersections were also seen in these samples (Figure 5.28(b)). Detailed microscopic observation at the failure surface have shown wavy slip lines at the surface especially near to the debonded fibers (Figure 5.29(a) and (b)). Although slip lines were also seen in high strain rate tests (Figure 5.29(c)), the failure is cleavage type as shown in Figure 5.29(c). It was also note that the separation of the fiber from the matrix Although the fracture surface of the matrix in quasi-statically deformed samples contained wavy slip lines as shown in Figure final separation of the matrix between the fibers

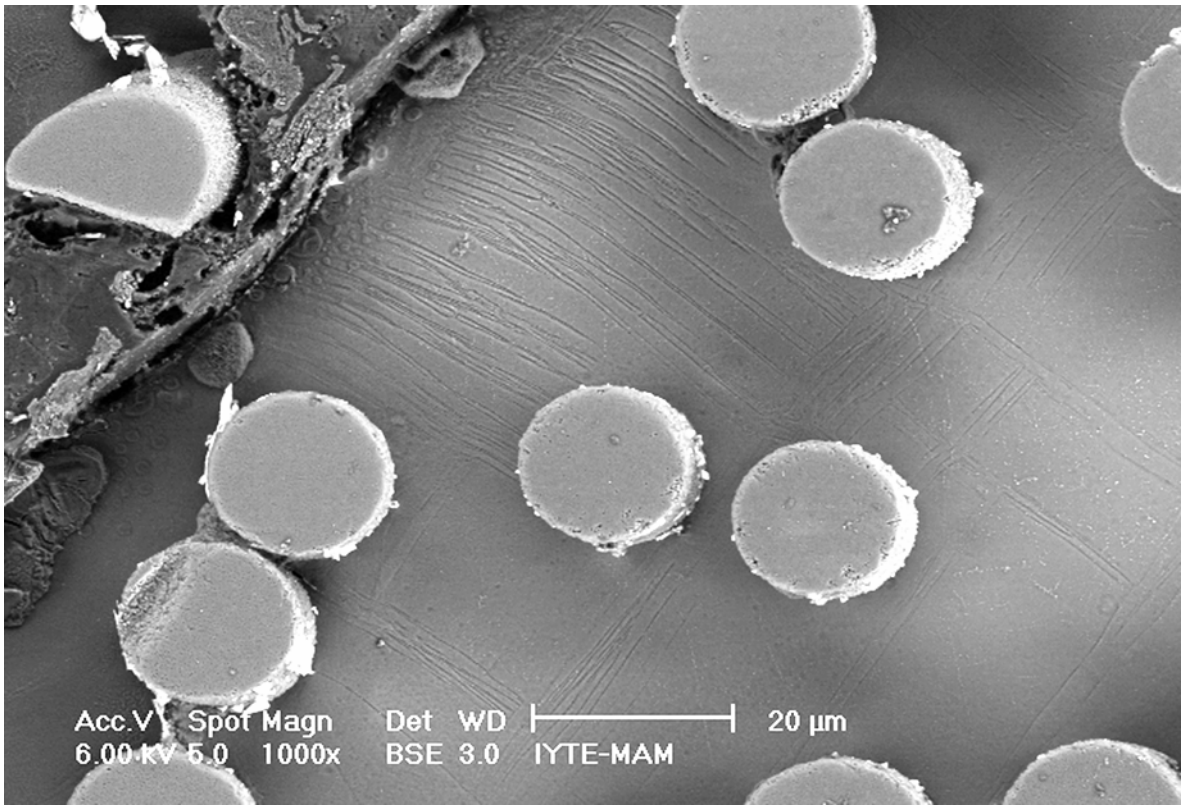

(a)

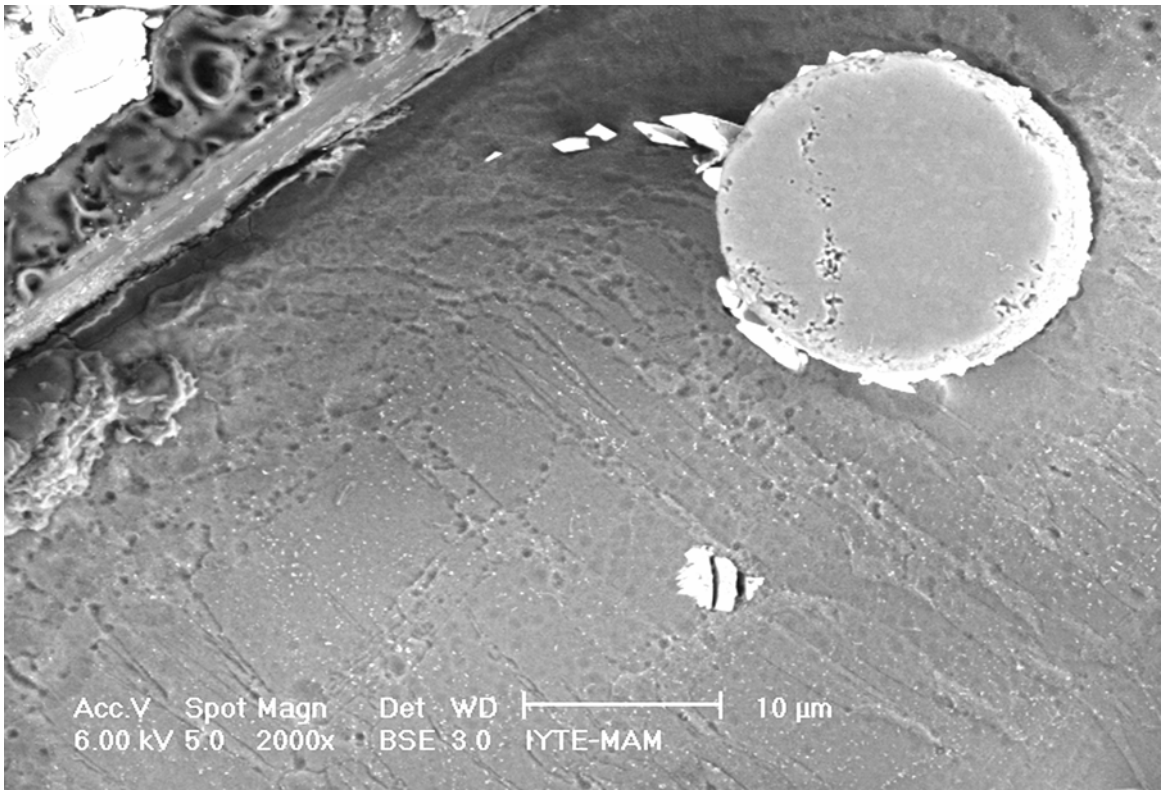
Acc.V Spot Magn Det WD 10 µm
6.00 kV 5.0 2000x BSE 3.0 IYTE-MAM

(b)

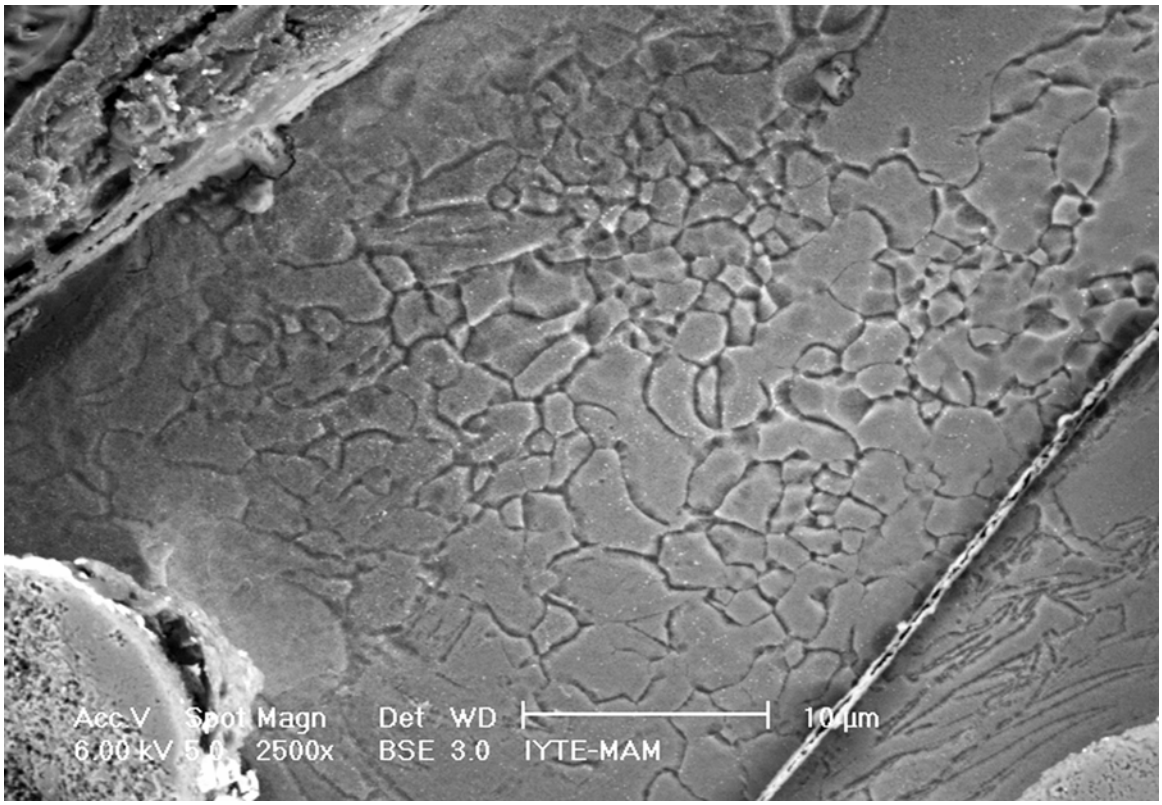
Acc.V Spot Magn Det WD 10 µm
6.00 kV 5.0 2500x BSE 3.0 IYTE-MAM

(c)

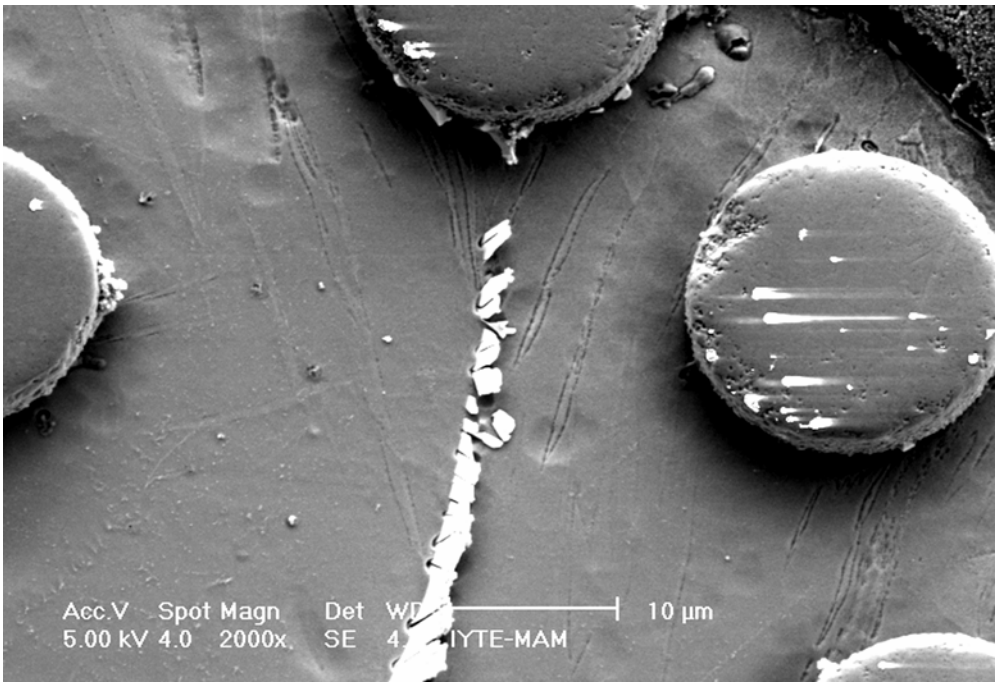

(d)

Figure 5. 27 SEM micrographs of a sample tested at $1.3x10^{-4}s^{-1}$ showing shear and twinned region near the failure surface, (b) a higher magnification of the region given in (a), (c) dynamically recrystallized grains next to the failed surface and (d) deformation of the grain boundary precipitates by twinning.

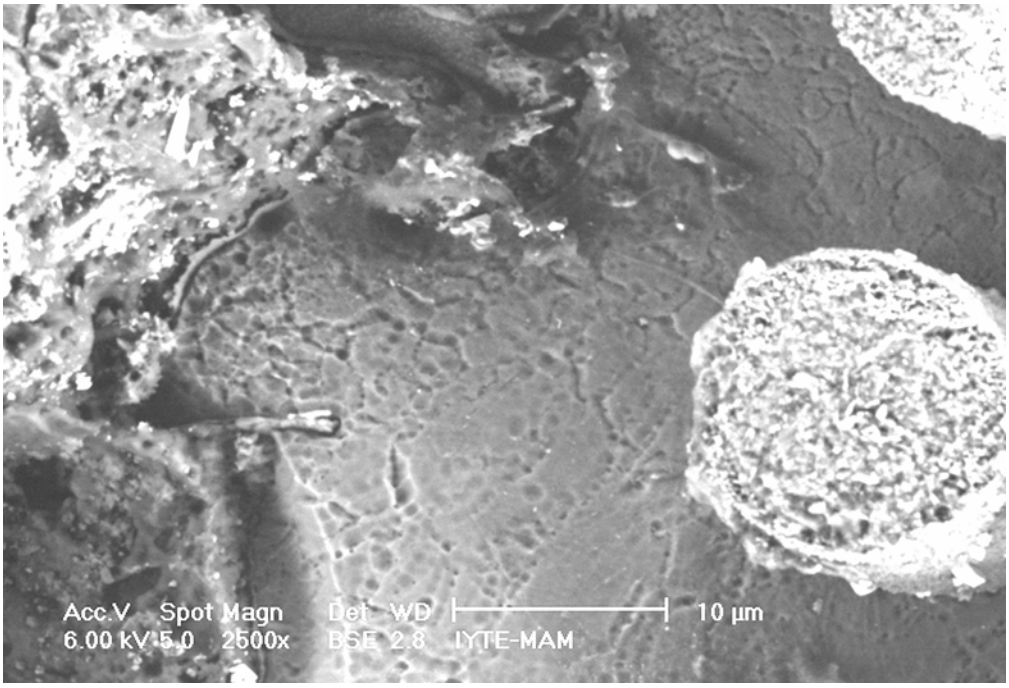

(a)

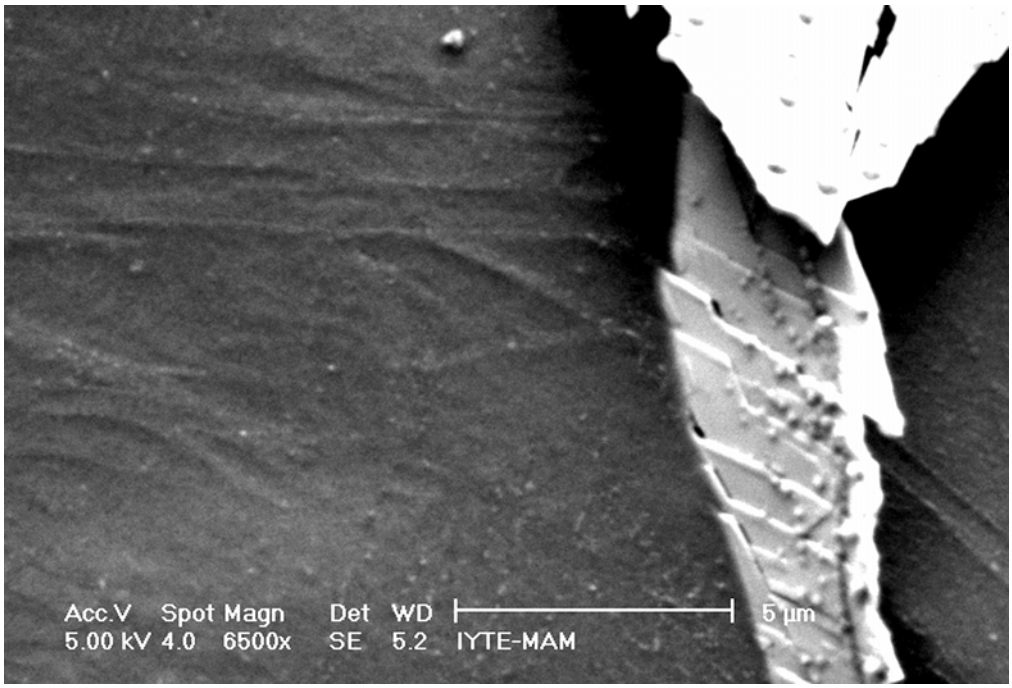

(b)

Figure 5. 28 a) DRX grains next to failure, b) precipitate cracks of twins

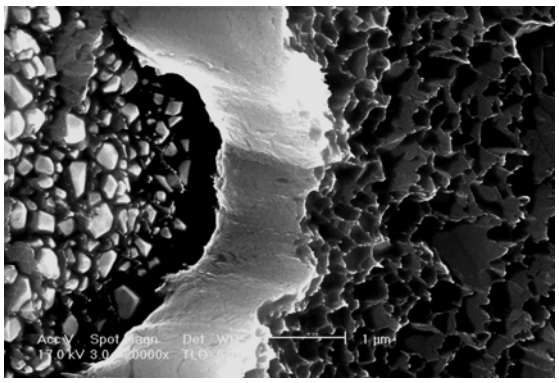

(a)

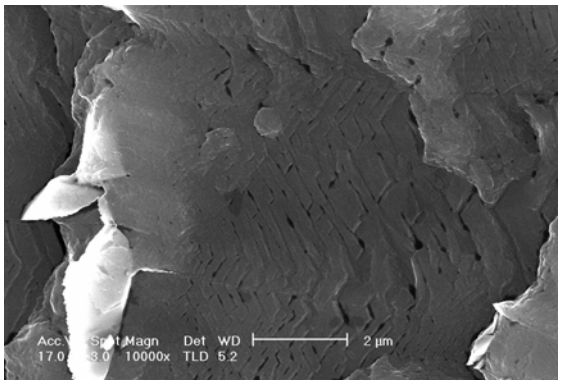

(b)

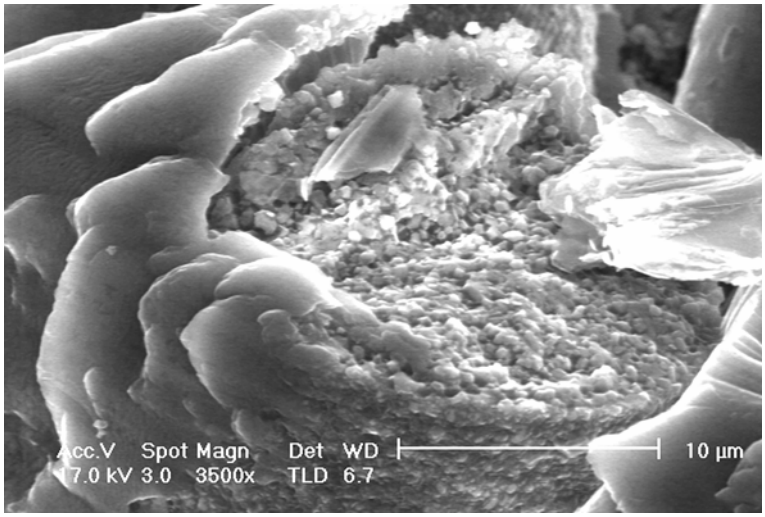

(c)

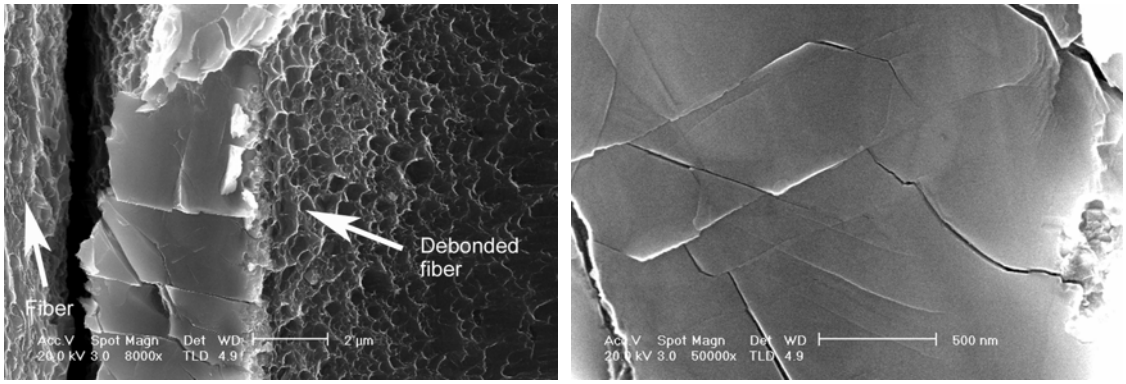

(d) (e)

Figure 5.29. S.E.M. images of fracture surfaces samples tested at strain rate 750 s^{-1}.

5.4.2 Axial direction

Two types of failure mechanism were observed in this direction: failure resulted from kink formation and/or axial splitting and failure by brooming. The formers occurred when end caps or metal inserts were used to support the specimen ends and the later was formed when the ends of the samples were not supported. In Figure 5.30(a) and (b) typical modes of failure in composite samples tested at $1x10^{-4}$ and 500 s^{-1} are presented, respectively. The kink formed near to the one of the end caps as previously reported [64]. The second sample of Figure 5.30(b) presents the sample tested at high strain rate and failed by kinking and axial splitting. It is anticipitated that splitting occurred following and/or as a parallel deformation to kinking. Small areas of splitted regions were also observed in quasi-statically tested samples.

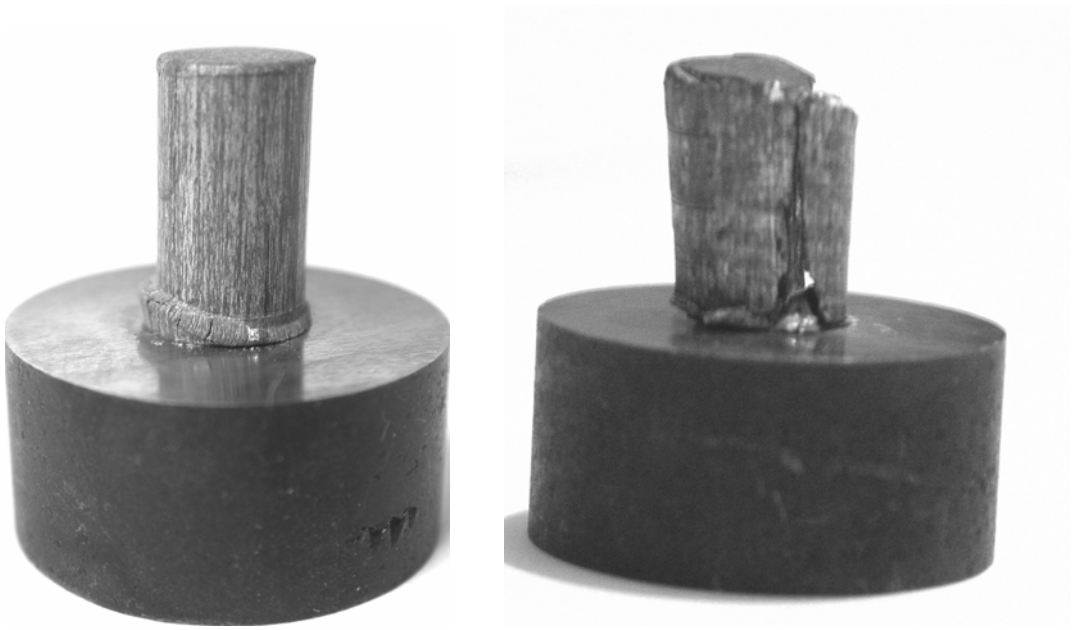

Figure 5.30 Samples tested at (a) $1x10^{-4}$ s^{-1} and (b) 500 s^{-1}.

Typical kink formation in a dynamically tested specimens recovered just after the maximum compressive strength is shown in Figure 5.31 (a). The final failure observed in kink region as shown in Figure 5.31(b).

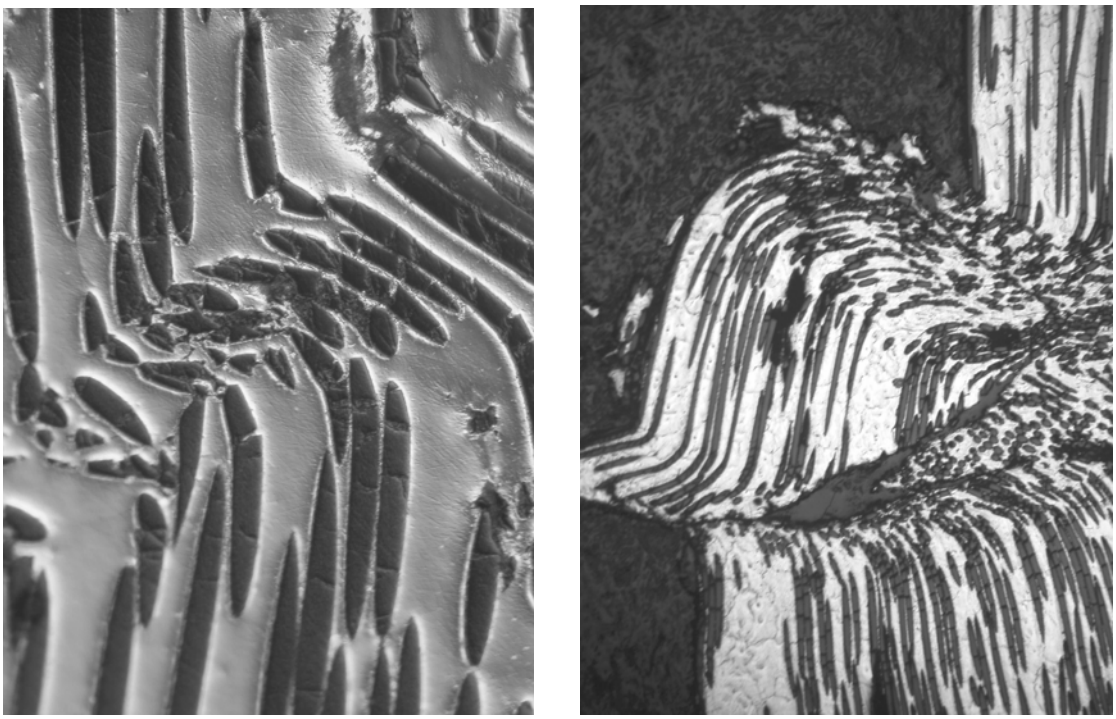

(a) (b)

Figure 5. 31(a) The kink band progression in a sample deformed at 500 s^{-1} and (b) failure in the kink band region in a sample tested at $1x10^{-4}$ s^{-1}.

Extensive fiber fracture in the form of buckling was observed at king boundaries as well as within the kink region (Figures 5.31(a) and (b)). It would be noted here, a buckled fiber could form a tension stress in the buckling and a compression stress at the opposite side in the matrix. The tensile stresses in the matrix would then tend to form a highly deformed region or voids in the matrix and the opposite side of the fiber pieces was then under compression (Figure 5.32(a)). The small fractured but non separated fiber pieces seen on the top of the fibers in Figure 5.32(b) corresponded to the compression side of the buckled fiber and in opposite side fiber-matrix interface was extremely opened (Figure 5.32(b)). Another fracture surface feature is shown in Figures 5.33(a) and (b). The fibers in the kink boundary and in the kink band region were fragmented under the shear strain operating in the matrix resulted from microbuckling.

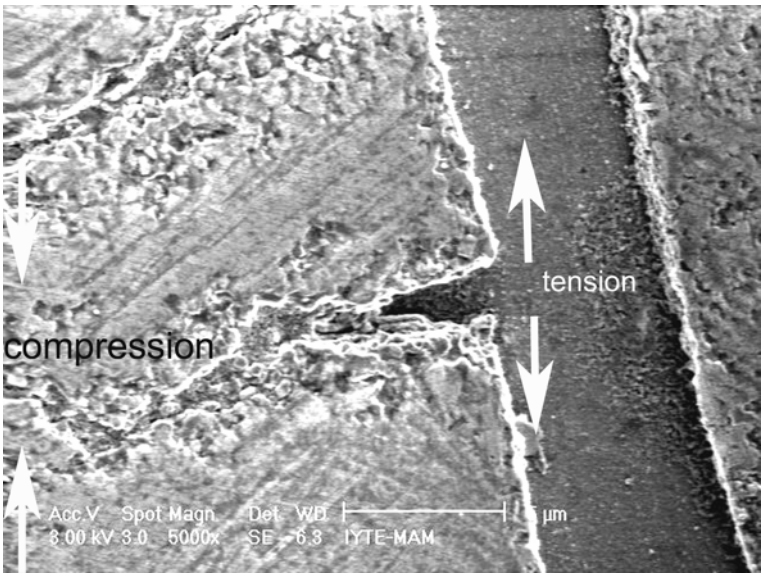

(a)

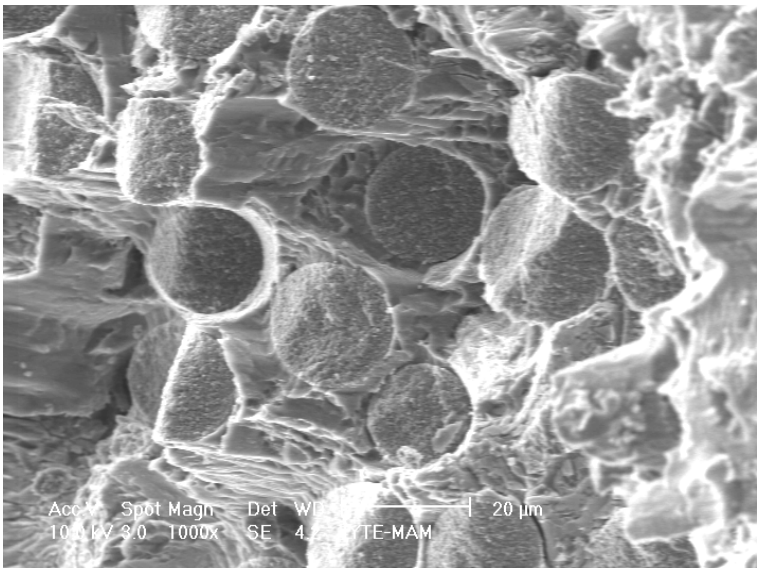

(b)

Figure 5. 32 (a) Fiber buckling and formation of tensional and compressional regions in the matrix in a sample tested at $1x10^{-4}$ s^{-1} and (b) fracture surface of the sample tested at 500 s^{-1} showing tensional and compressional regions around the fibers.

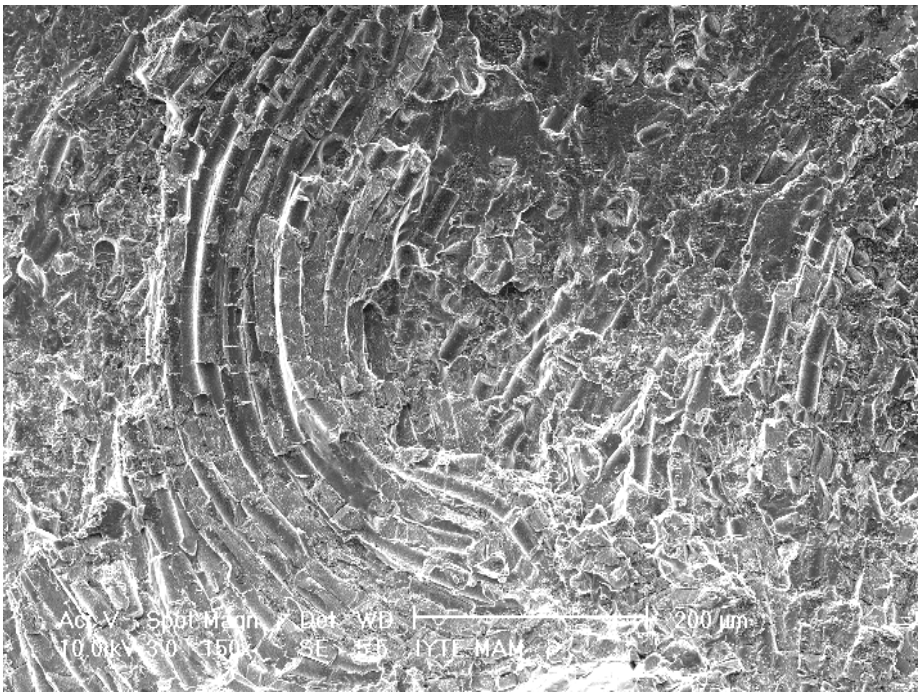

(a)

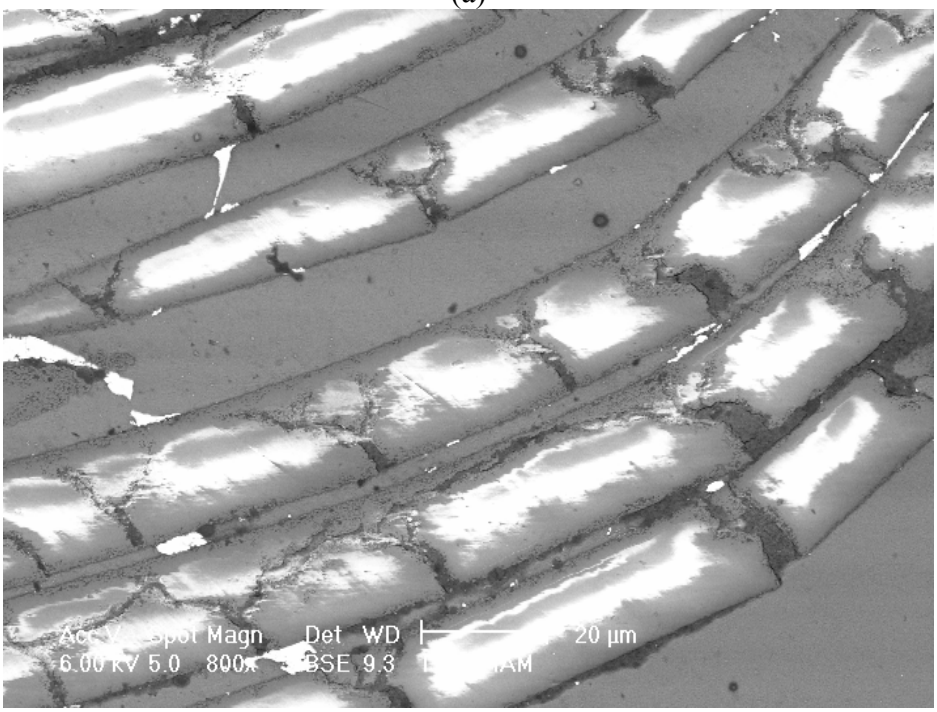

(b)

Figure 5.33. (a)Extensive fiber fracture at the kink boundary where the fracture of the sample occurred, sample tested at 500 s^{-1} and (b)fiber fragmentation within the kink band in a sample tested at $1x10^{-4}$ s^{-1}.

The shearing of the kink band produced a highly deformed region inside kink band(Figure 5.34(a). Twining was observed within the kink band and near to the kink band boundaries and also in places away from the kink region (Figure 5.34(b)). Twinning similar to the quasi-statically tested sample was also found to occur in dynamically tested samples as shown in Figure 5.34(c). These results confirmed that

twining is also the main deformation mode in the composite through the axial direction. Furthermore in small areas DRX were seen in the tested samples within the kink region (Figure 5.34(d)). Similar to the transverse direction, in axial direction the fracture surfaces contained wavy slip lines (Figure 5.35(a) and (b)), proving deformation by slip also contribute to the final deformation in this direction.

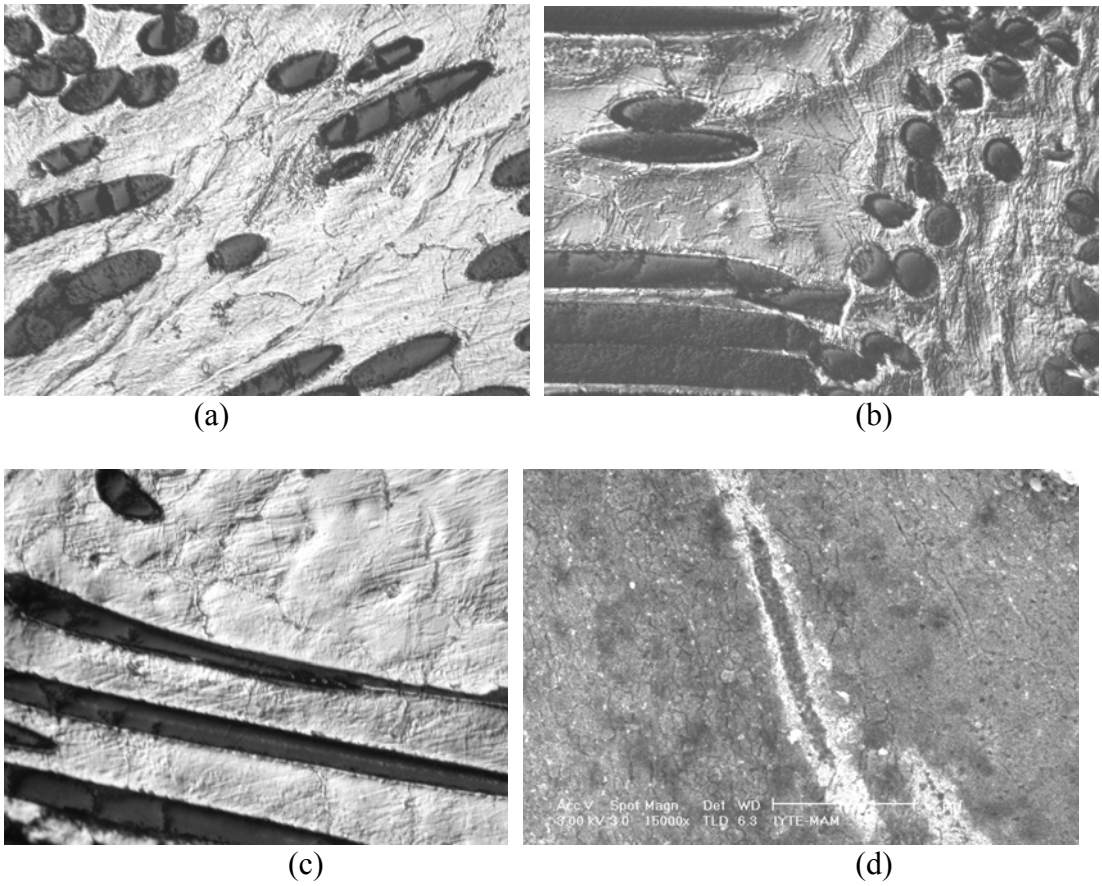

Figure 5. 34 Highly deformed region in a kink band (a)and twinning near to the kink region (b) in quasi-statically tested sample and (c) twining and (d) DRX formation in dynamically tested sample.

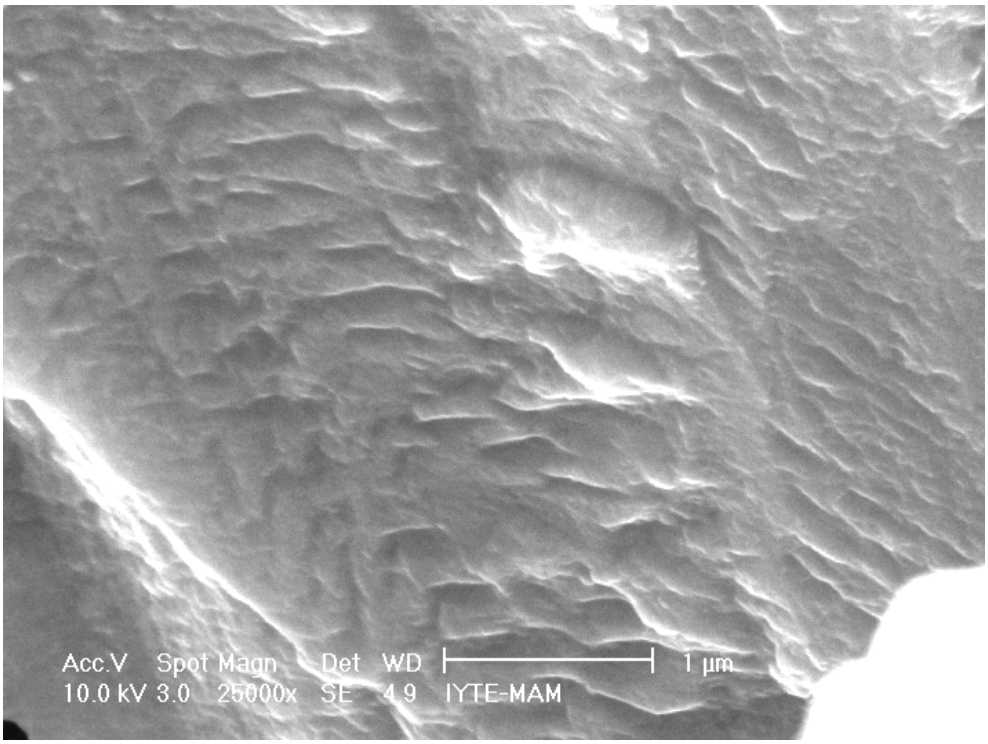

(a)

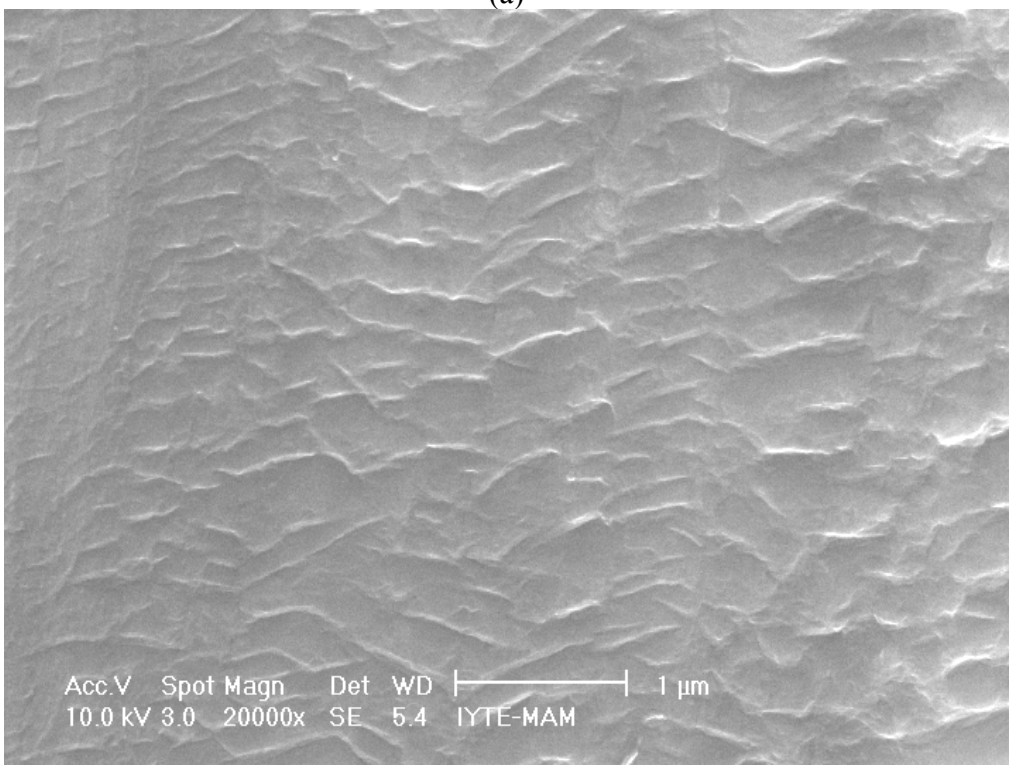

(b)

Figure 5.35. Wavy slip lines on the fracture surfaces of samples tested at (a) 500 s^{-1} and (b) $1.3x10^{-4}$ s^{-1}

Chapter 6

DISCUSSION

6. 1 Microstructure

The presence of Al in the secondary phases of the composite was most likely due to reaction between liquid Mg metal with FP fiber in the processing stage, in which Al_2O_3 was reduced by Mg leading to release of Al in to the melt and concurrently formation of MgO at the melt/oxide interface. The presence of a thin layer of MgO uniformly sorronding the Al_2O_3 fibers and in some locations and the formation of Al_2MgO_4 spinel phase in Mg-alloys composite were also observed previously [65, 66]. Solidification behavior of Mg-Zn-RE alloy, with the similar composition of the present matrix alloy, was further studied by Wei at. al [67] and it was shown that the α–Mg grains were decorated with a ternary phase of Mg-Zr-RE. Coherent $MgZn_2$-type precipitates parallel to the c-axis of the matrix were also observed in TEM [26].

6.2 Validity of SHPB Tests

In SHPB testing of brittle materials for the valid failure stress values, stress homogenization occurred after about 3 to 4 reflections [68]. The limiting strain rate conditions are therefore needed to be verified based on the stress-homogenization for the attainment of valid ultimate failure properties. For brittle materials that show only linear elastic behavior before failure, the nominal strain rate can be approximated by

$$\dot{\varepsilon} = \frac{\varepsilon_f}{t_f} \tag{6.1}$$

where ε_f and t_f are the failure strain and failure time, respectively. Applying the condition of 4 reflections of wave the limiting strain rate can be determined by

$$\dot{\varepsilon} = \frac{\varepsilon_f c_s}{4L_s} \tag{6.2}$$

Eqn. 6.2 gives a limiting strain rate of 7500 s^{-1} with using following parameters: ε_ϕ~0.02, c~5000 m/s and L_s~13x10^{-3} m. The highest average strain rate in the testing of the composite in the axial direction was in the order 100 s^{-1}, proving the validity of the compressive strength values of the composite in this direction.

6.3 Deformation and strain rate effects in the transverse direction

The mechanical properties of unidirectional composites in the transverse direction are dominated by the matrix properties. However, in terms of damage formation the presence of fibers normal to the loading direction in compression is very significant. Typical damage observations made in MMC's include debonding, fiber fracture and crushing and matrix fracture on the maximum shear stress plane at ~45° to the compressive loading axis [69, 70]. The observations made in this study are very similar to those given above. Therefore, it may be assumed that the rate sensitive flow stress behavior observed in the transverse direction of FP/Mg and FP/Al composite is due to strain rate sensitive flow stress behavior of the matrix alloy.

Mg has hexagonal closed-packed (hcp) crystal structure with limited number of slip systems and therefore its ability to deform is limited especially at room temperature. At room temperature slip occurs predominantly on the basal plane $\{0001\}$ in $<11\bar{2}0>$ direction while prismatic, $\{10\bar{1}0\}$, and pyramidal, $\{10\bar{1}1\}$ and $\{10\bar{1}2\}$, slip become more important at increasing temperatures. In addition to slip on the basal plane, twinning on the $\{10\bar{1}2\}<\bar{1}011>$ provides means of deformation. Double twinning, involving $\{10\bar{1}1\}$ followed by $\{10\bar{1}2\}$ has also been shown to be important and facililates compression along the c-axis [71].

At room temperature the plastic deformation by slip is evidenced in Figure 5.29 (d) by uneven configuration (different slip planes) of slip bands due to the basal and non-basal slip from the microsrocopic observation of the failed samples. The presence of debonded fibers on the fracture surface of quasi-statically tested samples (Figures 6.1(a) and (b)) further show that fiber debonding are effective in the development of failure both quasi-static and high strain rates. In the failure region, the deformation

strain increased greatly due to the maximum shear stresses operating in this region, 45 ^{o} to the loading axis. The increased strain is evidenced by the excessive deformation region just next to the fracture. Near to the fracture surface, DRX grains and twins are clearly seen in Figure 6.2. It is therefore the composite sample in the transverse direction is eventually failed by the shear band formation, but detailed analysis of failure mechanism will elaborated in the following sections.

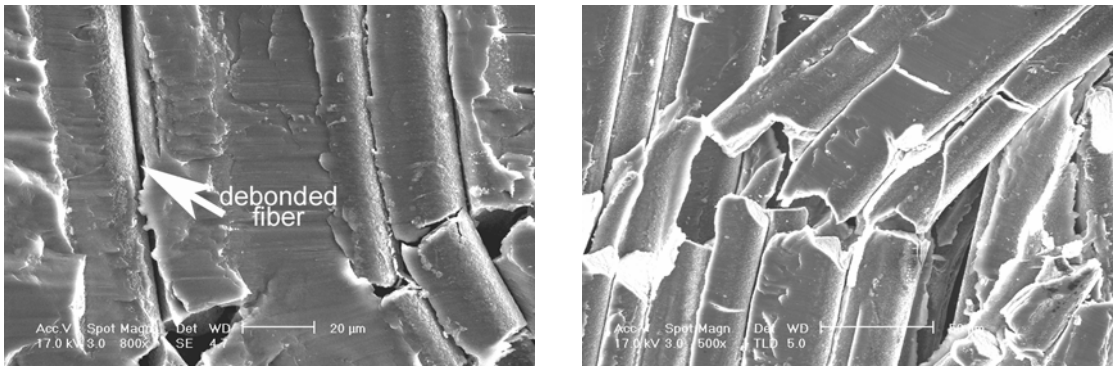

Figure 6.1 Debonded fibers on the surface of the failed samples of transverse direction, (a) $1.3X10^{-4}s^{-1}$ and (b) $500s^{-1}$.

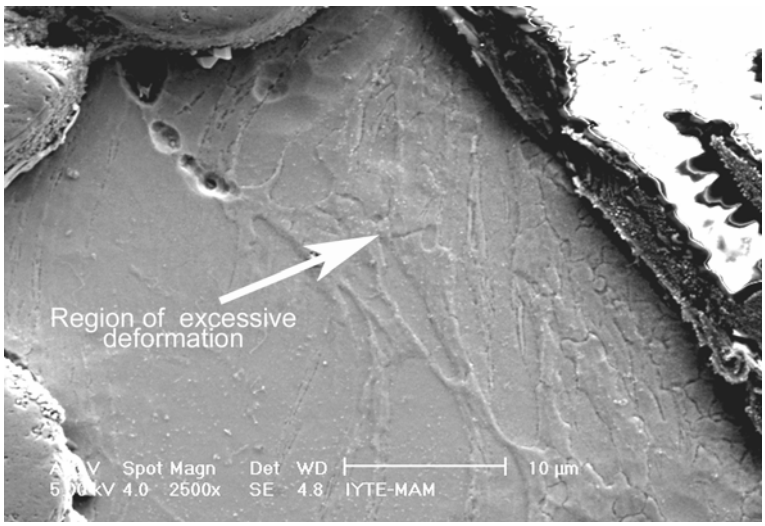

Figure 6.2 Region of excessive deformation near to the fracture surface in a sample tested at $1.3X10^{-4}s^{-1}$

DRX refers to the concurrence of recrystallization during deformation and in this annealing or softening process, both nucleation and growth processes are taking place while the strain is applied [72]. This phenomenon usually occur at high temperatures during working of Mg alloys and the presence of a distinct peak in the flow stress often occurs just following the onset of dynamic recrystallization [11, 12, 15, 72]. DRX was also observed at relatively low temperatures, Low Temperature Dynamic Crystallization

(LTDRX) [73]. The nucleation of the DRX in polycrystalline materials predominantly proceeds from the grain boundaries and expands into the unrecrystallized parts. The grain refinement microstructure is usually called necklace structure [74]. A twinning induced DRX model has been also proposed (Figure 6.3) [15]. In the initial stage of twinning, basal dislocations with **a** Burgers vector accumulates near twin boundaries. With the increasing of strain more dislocation pile-up at the grain boundary and the stress concentration reach the critical resolved shear stress for the activation of the non-basal slip (a+c). Three dimensional DRX nuclei then form by the interaction of (a) and (a+c) dislocations. Since the growth of DRX nuclei grow to crystallized small strains under the control of grain boundary migration, it shows temperature as well as strain rate sensitivity. Wang et al. [75] have recently investigated the role of twinning during dynamic recrystallization in 800H alloy and showed that the twin frequency at the DRX front was a factor of two higher than the DRX volume average. They concluded that twinning was an active nucleation mechanism of DRX to promote the expansion of the recrsytallizition front in the course of DRX.

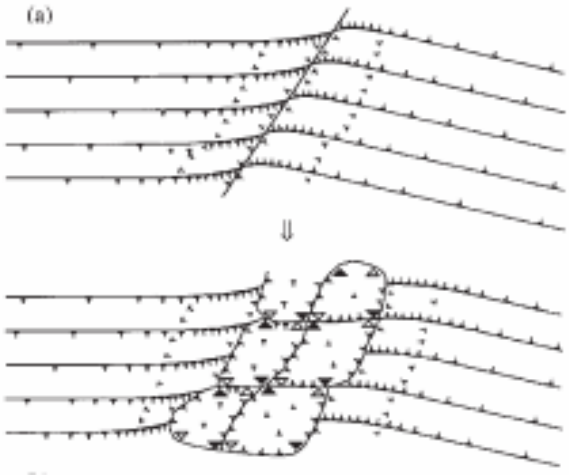

Figure 6.3 DRX nucleation process [11].

Typical deformation microstructure of an Mg-Al-Zn alloy, which was tested under torsion at various temperatures and strain rates was reported to be the subgrains formation that was aided by the additional slip system operation as a results of both higher temperatures and more complex stresses near the twin intersections [12]. As the temperature increased the matrix developed the substructure resulting from the basal and non-basal slip systems. It was also found that at low temperatures twin intersections

consisted of sharp diamond shaped cells become polygonal with high misorientations [12]. The heavily etched microstructure of the studied composite sample tested until failure strain is shown in Figure 6.4. The microstructure shown in this figure was taken from the regions adjacent to the fracture region. DRX grains next to the fracture surface are clearly seen in this figure. Near to the DRX grains heavily etched specimen microstructure reveal also the formation of polygonal subgrain structure. The subgrains were also observed to form preferentially near to the fiber matrix interface (Figure 6.4), within the twin bands (Figure 6.5) and near to the grain boundary and /or second phases (Figure 6.6 and 6.7).

The failure of the composite procedded 45^{o} to loading axis, where the shear stress was the maximum. In this region twin bands were formed within the grains and/or at the fiber matrix interface. DRX grains formed preseuambly at twin intersections, grain boundaries, fiber/matrix interface and /or near to the secondary particles since the deformation localization in these regions is expected to nucleate DRX grains. The strain localization in the regions of the DRX grains presumably promoted the failure in this region.

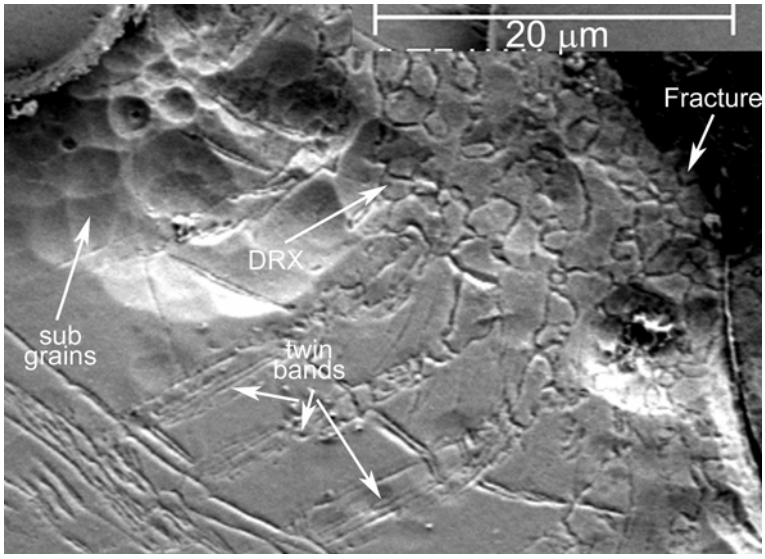

Figure 6.4 SEM micrograph showing the matrix microstructure near to failed section in a sample tested at $1x10^{-4}s^{-1}$.

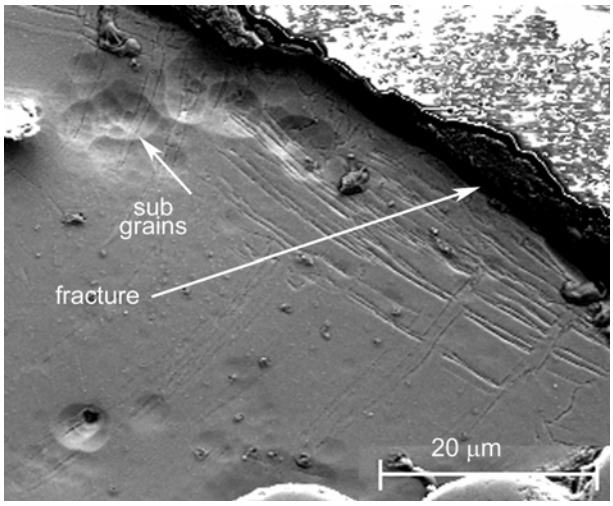

Figure 6.5 SEM micrograph showing the subgrain structure on the twin bands near to failed section in a sample tested at $1x10^{-4}s^{-1}$.

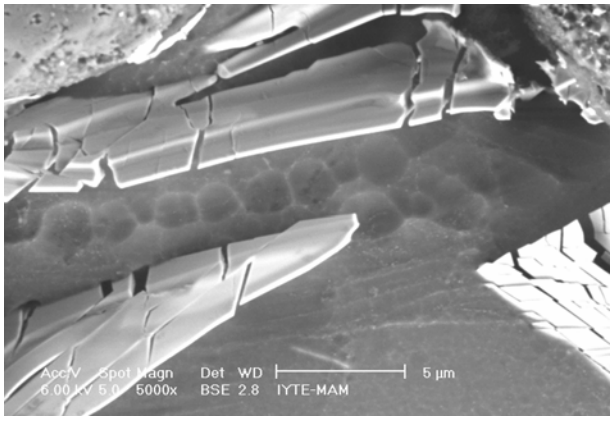

Figure 6.6 SEM micrograph showing the subgrain structure near to grain boundary second phases in a sample tested at 500 s^{-1}.

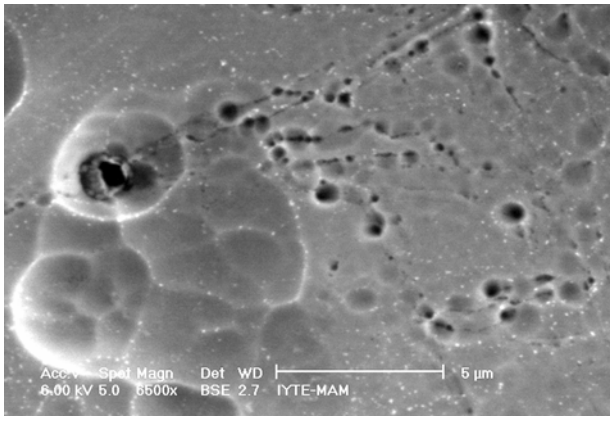

Figure 6.7 SEM micrograph showing the subgrain structure a matrix second phase in a sample tested at 500 s^{-1}.

The strain to peak (when DRX forms a peak stress) increases with decreasing temperature and decrease with increasing strain rate. Lower strain rates provide more time and higher temperatures provide higher mobility for DRX [15]. The observed increased peak stress and reduced strain to peak in the transverse direction therefore show well accordance to the previous studies. At high strain rates the DRX formed at lower strains and once they formed strain localization failed the sample in the DRX region.

The role of deformation twinning on strain hardening in cubic and hexagonal polysrystalline metals has been investigated recently [75]. It was shown that the hardening of the material by deformation twinning due to reduction of the effective slip length (Hall-petch effect) and increases in hardness of the twinned regions (Basinski mechanism). Basinski [76] proposed that glissile dislocations before twinning was converted into sessile configurations as a results of the twinning shear deformation. Consequently the twinned regions should be harder than the untwined regions and will thus provide an overall hardening of the material. Third there is a textural softening arising from the reorientation of the material to the favorable orientation for slip, which in contrary to the first two mechanisms results in softening.

Experimental studies on a HCP structure metal, Ti have shown that at constant strain the twin concentration increased with increasing strain rate [77]. In this study the twin concentration was measured in failed samples having different failure strains and they were measured near to the failed section. Additionally there are counted with optical microscope and therefore measurement show the only macro twins. Adding all these factors it is rather difficult to conclude that the twin concentration increased with strain rate. Similar to the hcp Ti [78] although the cross sections of the deformed sample filled with twins particularly near to the failed section of the specimen the evidence of the single and multiple slip on the fracture surfaces dictates that slip is dominant deformation mechanism and therefore thermally activated deformation is valid for the tested composite sample in the transverse direction. Previous studies on Mg alloys have showed that the flow stress increased with increasing strain rate [11, 17, 31, 73, 78] and therefore the measured strain rate sensitivity of the composite in the transverse direction is due to the matrix strain rate sensivity. Previous studies on many metals have shown that metallic materials such as copper [79] and aluminum [80] show increased strain-rate sensitivity at strain-rates in excess of $\sim 10^3 s^{-1}$. This increase in strain-rate sensitivity is interpreted as a change in the deformation mechanism. Below

~$10^3 s^{-1}$, deformation is believed to be controlled by thermal activation and the strength of the material increases slowly, if at all, with the strain-rate. The change of deformation mechanism after ~$10^3 s^{-1}$ is interpreted as a result of the increasing importance of a dislocation drag mechanism and the strength/strain-rate dependence becomes linear in this region. This explanation of the strain-rate dependent strength of common metallic materials applies also to the unreinforced matrix material tested in this study since no appreciable rate sensitivity is observed at strain-rates below ~$10^3 s^{-1}$.

6.4 Deformation and strain rate effects in the longidutional direction

The failure mode in Mg and Al MMCs in the axial direction is predominantly fiber microbuckling parallel to the loading axis, except axial splitting was promoted in Mg composite at high strain rates. Therefore, the compressive strengths were essentially governed by the composite shear stress–strain response. For composites following the Ramberg-Osgood shear stress–strain response, the compressive strength is predicted by [81]

$$\sigma_c = \frac{G}{\left[1 + n\left(\frac{3}{7}\right)^{\frac{1}{n}}\left(\frac{\phi/\gamma_y}{n-1}\right)^{\frac{n-1}{n}}\right]} \quad (1)$$

where G is the shear modulus of the composite (G_{12}), n is the hardening exponent
t, γ_y is the composite yield strain in the longitudinal shear and Φ is the average fiber misorientation. The compressive strength of FP fiber reinforced Mg and Al composites were predicted using above equations. The material parameters for Al composite were chosen as G=36 GPa, n=8 [81], $\phi=3^o$ and $\gamma_y=0.003$. The shear yield strain was rougly calculated by dividing the matrix shear yield stress (~80GPa [82]) by the composite shear modulus. The composite shear modulus was approximated using following relation [83]

$$G = \left[\frac{f}{G_f} + \frac{(1-f)}{G_m}\right]^{-1}$$

Where G_f and G_m are the fiber and matrix shear modulus and typical values are 130 and 26 GPa, respectively. Fiber misorientation of 0-5^o are common for the long fiber

composites [81]. For Mg composite following parameters were used G=25 GPa, n=8, $\phi=3^{o}$ and $\gamma_y=0.0052$. Similarly the shear yield strain was calculated by dividing the matrix shear yield stress (~138GPa [64]) by the composite shear modulus. Using above parameter the composite strength in the axial direction was ~2100 MPa and 2400 MPa for Al and Mg matrices, respectively. These values were found higher than those of average quasi-static fracture strengths, 1800 and 2100 MPa. It should be noted that calculated values are only rough estimates and as the fiber misorientation increases the compressive strength value decreases. But both in experimental and calculated stress values are higher for Mg composite and the differences between them are the same 300 MPa for experimental and calculated values. The higher compressive strength of the Mg composite simply arises from the higher shear stresses of the studied Mg composite which resulted in higher yield shear strains.

It is noted that the compressive strength of the FP-Al composite is higher than that of FP-Mg composite at strain rate higher than $100s^{-1}$. This is mainly due to the higher strain rate sensitivity of the FP-Al composite as compared with FP-Mg composite in the axial direction. The compressive strength of FP-Mg composite in the axial direction essentially remains to be constant as the strain rate increases to 100's s^{-1}. Eqn. 1 dictates that the increase in matrix yield strength with increasing strain rate will increase the compressive strength and this effect is clearly seen in FP-Al MMC. The strain rate insensitive behavior of the composite in the axial direction may be due to the several possible reasons. In axial loading similar to the transverse direction twinning and DRX grain formation were observed in the kink region. One possible reason for the lack of strain rate sensitivity of the composite in the axial direction may the formation of DRX grains prior to the kink band formation which resulted in softening of the matrix alloy and hence reduced shear strength. The higher rate of temperature increase at high strain rate due to near adiabatic conditions also promotes early DRX formation. Second since the composite in the axial direction is relatively brittle, the large variation of the compressive strength may hide the any rate sensitive behavior to detect. And lastly the highest strain rate tested in the study may not enough to see strain rate sensitive compressive strength since the strain rate become effective after $1000s^{-1}$ in many materials.

CHAPTER 7

Conclusion

The mechanical response of an FP long fiber (35%) Mg composite has been determined in the transverse and longitudinal directions in compression. Results were also compared with those of a similar composite of Al matrix. It was found that the composite in the transverse direction exhibited strain rate sensitivity of the flow stress and maximum stress within the studied strain rate range (10^{-4} to $1x10^{3}s^{-1}$). However the increase in strain rate decreased the failure strain. Microscopic observations on the failed samples have shown that the composite failed predominantly by shear banding. Near to the fracture surface DRX grains were observed within the shear band and it was proposed that the lower ductility of the composite at increasing strain rates was due to the early DRX grain formation which softened the composite and resulted in lower ductility. Although twinning was observed in the deformed cross-sections of the samples at all strain rates particularly near the shear band region, it was proposed that the main deformation mechanism was slip which was evidenced by the slip lines on the fracture surface. The strain rate sensitivity in fracture stress of the composite in transverse direction was also found to be similar to that of the Al composite tested in the same direction. In the longitudinal direction, the composite failed by kink formation at quasi-static strain rates, while kinking and splitting at high strain rates. The maximum stress in the axial direction was however found to be strain rate insensitive. In this direction similar to transverse direction DRX grain formation was observed in the kink region. The lack of strain rate sensitivity in this direction was attributed to DRX grain formation at high strain rates combined with adiabatic heating and the brittle nature of the composite leading to fluctuatiton in the compressive strength.

In order to determine any strain rate sensitivity in axial direction additional tests should be conducted in SHPB. The deformation microstructure of the samples should also be analyzed in transmission electron microscope in order to identify the effect of strain rate on the twin and DRX grain formation.

REFERENCES

[1] S. Kudela, "Magnesium Lithium matrix composites – an overview", *International Journal of Materials and Product Technology*, **18**, (2003), 91

[2] Hu Lianxi and Wang Erde, "Fabrication and mechanical properties of SiC_w/ ZK51A magnesium matrix composite by two-step squeeze casting", *Materials Science and Engineering*, **A278**, (2000), 267

[3] Z.Trojonová, W.Riehemann, H. Ferkel, P. Lukáč, "Internal friction in microcrystalline magnesium reinforced by alumina particles", *Journal of Alloys and Compounds*, **310**, (2000), 396

[4] Narasimalu Srikanth and Manoj Gupta, "Dumping characterization of magnesium based composites using an innovative circle-fit approach", *Composites Science and Technology*, **63** (2003), 559

[5] S.Seshan, M. Jayamathy, S.V. Kailas, T.S. Srivatsan, "The tensile behavior of two magnesium alloys reinforced with silicon carbide particulates", *Materials Science and Engineering*, **A363**, (2003), 345

[6] L. Lu, K. K. Thong and M. Gupta, "Mg-based composite reinforced by Mg2Si", *Composites Science and Technology*, **63**, (2003), 627

[7] Q.C. Jiang, H.Y. Wang, J.G. Wang, Q.F. Guan, C.L. Xu, "Fabrication of TiC_p/Mg composites by the thermal explosion synthesis reaction in molten magnesium", *Materials Letters*, **57**, (2003), 2580

[8] M.D. Nave, M.R. Barnett, "Microstructures and textures of pure magnesium deformed in plane-strain compression", *Scripta Materilia*, **51**, (2004), 881

[9] S. Barbagallo, P. Cabvaliere, E.Cerri, "Compressive plastic deformation of an AS21X magnesium alloy produced by high pressure die casting at elevated temperatures", *Materials Science and Engineering A*, **367**, (2004), 9

[10] P. Yang , Y. Yu , L. Chen and W. Mao, " Experimental determination and theoretical prediction of twin orientations in magnesium alloy AZ31", *Scripta Materialia*, **50**, (2004), Pages 1163

[11] M. R. Barnett, "Influence of deformation conditions and texture on the high temperature flow stress of magnesium AZ31", *Journal of Light Metals*, **1**, (2001), 167

[12] M. M. Myshlyaev, H. J. McQueen, A. Mwembela and E. Konopleva, "Twinning, dynamic recovery and recrystallization in hot worked Mg–Al–Zn alloy", *Materials Science and Engineering A*, **337**, (2002), 121

[13] S. Kleiner and P. J. Uggowitzer, "Mechanical anisotropy of extruded Mg–6% Al–1% Zn alloy", *Materials Science and Engineering A*, **379**, (2004), 258.

[14] C. Yan, L. Ye and Y.-W. Mai, "Effect of constraint on tensile behavior of an AZ91 magnesium alloy", *Materials Letters*, **58**, (2004), 3219

[15] A. Galiyev, R. Kaibyshev and G. Gottstein, "Correlation of plastic deformation and dynamic recrystallization in magnesium alloy ZK60", *Acta Materialia*, **49**, (2001), 1199

[16] S.C. Sharma ,B. Anand, M.Krishna, "Evaluation of sliding wear behavior of feldspar particle reinforced magnesium alloy composites," *Wear* **241**, (2000), 33

[17] P. Pérez, G. Garcés, P. Adeva, "Mechanical properties of a Mg–10(vol %)Ti composite ", *Composites Science and Technology*, **64**, (2004), 145

[18] L.Lu, C.Y.H. Lim, W.M: Yeong, "Effect of reinforcements on strength of Mg9%Al composites", *Composite Structures*, **66**, (2004), 41

[19] R. A. Saravanan and M. K. Surappa, "Fabrication and characterization of pure magnesium-30 vol.% SiC_p particle composite", *Materials Science and Engineering A*, **276**, (2000), 108

[20] C.Y.H. Lim, S.C. Lim, M.Gupta, "Wear bahavior of SiC_p-reinforced magnesium matrix composites", *Wear*, **255**, (2003), 629

[21] H.Y. Wang, Q.C. Jiangs, Y. Wang, B.X. Ma and F. Zhao,"Fabrication of TiB2 particulate reinforced magnesium matrix composites by powder metallurgy", *Materials Letters*, **58**, (2004), 3509

[22] M.Y. Zheng, W.C. Zhang, K.Wu, C.K. Yao, "The deformation and fracture behavior of SiC_w/AZ91 magnesium matrix composite during in-situ TEM straining", *Journal of Materials Science*, **38**, (2003), 2647

[23] M.Y. Zheng, K. Wu, C.K. Yao, “Effect of interfacial reaction on mechanical behavior of SiCw/AZ91 magnesium matrix composites”, *Materials Science and Engineering A*, **318**, (2001), 50

[24] M.Y. Zheng, K. Wua, M. Liang, S. Kamadob, Y. Kojima, "The effect of thermal exposure on the interface and mechanical properties of Al18B4O33w/AZ91 magnesium matrix composite", *Materials Science and Engineering A*, **372**, (2004), 66

[25] D. J. Towle and C. M. Friend, "Effect of reinforcement architecture on mechanical properties of a short fibre/magnesium RZ5 MMC manufactured by preform infiltration", *Materials Science and Engineering A*, **188**, (1994), 153

[26] Z. Trojanová, V. Gartnerová, P. Lukac, Z. Drozd, “Mechanical properties of Mg alloys composites reinforced with short Saffil® fibres*”, Journal of Alloys and Compounds*, **378**, (2004), 19

[27] Jensen, J.A., with L.S. Chumbley, "Processing and Mechanical Properties of Mg and Mg-Li Composites Containing Steel Fibers", *Metallurgical Transactions A*, **29A**, (1998), 863

[28] C. Hausmann, C. Cayron, O. Beffort, S. Long, “The influence of aluminum additions on the properties and microstructure of magnesium unidirectionally reinforced with T300 carbon fibres*”, 9th CIMTEC-World Forum on New Materials, SymposiumV, Florence, Italy*, June 1998

[29] M. Pahutová, V. Sklenićka, K. Kuchařova and M.Svoboda, “Creep resistance in magnesium alloys and their composites”, *International Journal of Materials and Product Technology*, **18,** (2003), 116

[30] C. Körner,w. Schäff, M. Ottmüller and R.F. Singer,"Carbon Long Fiber Reinforced Magnesium Alloys", *Advanced Engineering Materials*, **2**, (2002),327

[31] P. Klimanek and A. Pötzch, “Microstructure evolution under compressive plastic deformation of magnesium at different temperatures and strain rates”, *Materials Science and Engineering* A, **234**, (2002), 145

[32] T. Mukai, M. Yamanoi, H. Watanabe, K. Ishikawa and K. Higashi, “Effect of grain refinement on tensile ductility in ZK60 Magnesium Alloy under Dynamic Loading”, *Materials Transactions*, **42**, (2001), 1177

[33] H. Watanabe, T. Mukai, K. Ishikawa, "Differential speed rolling of an AZ31 magnesium alloy and the resulting mechanical properties", *Journal of Materials Science,* **39**, (2004), 1477

[34] T. Mukai, M. Yamanoi, and K. Higashi, “Processing of ductile magnesium alloy under dynamic tensile loading”, *Materials Transactions*, **42**, (2001), 2652

[35] Y.H. Wei, Q.D. Wang, Y.P. Zhu, H.T. Zhou, W.J. Ding, Y. Chino, M. Mabuchi, “Superplasticity and grain boundary sliding in rolled AZ91 magnesium alloy at high strain rates”, *Materials Science and Engineering*, **A360**, (2003), 107

[36] A. Fjeldly; H.J. Roven;"Effects of strain rate and anistropy on the tensile deformation properties of extruded AlZnMg Alloys", *Metallurgical and Materials Transactions*, **31A**, (2000), 669

[37] H. Takuda, S. Kikuchi, T. Tsukada, K. Kubota and N. Hatta, "Effect of strain rate on deformation behaviour of a Mg–8.5Li–1Zn alloy sheet at room temperature"*Materials Science and Engineering A*, **271**, (1999), 251

[38] Y.El Saeid Essa, J.L. Pérez-Castellanos, “Effect of the strain rate and temperature on the mechanical behavior of a Mg–5% Zn alloy reinforced with SiC paritcles”, *Journal of Materials Processing Technology,* **143**, (2003), 856

[39] P.M., Jelf and N.A. Fleck, “Compression failure mechanismsin unidirectional composites”, *Journal of Composite Materials*, **26**, (1992), 2706

[40] V.W. Rosen, “Mechanics of composite strengthening. In: Fiber Composite Materials”, *American Society of Metals, Metals Park, Ohio,* (1965), 37

[41] A.G. Evans, W.F. Adler, “Kinking as a mode of structural degradation in carbon fiber composites”, *Acta Metallugica*, **26**, (1978),725

[42] S.Kyriakides, R. Arseculeratne, E.J. Perry, K. Liechti, “On the compressive failure of fibre reinforced composites”, *Internatinal Journal of Solid Structures*, **32**, (1995), 689

[43] M.R. Piggott, B.J. Harris, “Compression strength of carbon, glass, and Kevlar-49 fibre reinforced polyster resins”, *Materials Science. and Engineering*, **15**, (1980), 2523

[44] C. Sourtis, R. Tenchev, “A Property Degradation Model for Fibre Microbuckling Failure in Composite Laminates”, *Science & Engineering of Composite Materials*, **4**, (1995), 28

[45] P.M. Moran and C.F..Shih, “Kink band propagation and broadening in ductile matrix fiber composites: experiments and analysis”, International Journal of Solids Structures”, 35, (1998), 1709

[46] J.S. Paulsen, P.M. Moran, C.F.Shih, E. Byskov, “Kink band initiation and band broadening in clear wood under compressive loading”, *Mechanics of Materials*, **25**, (1997), 67

[47] Norman A. Fleck and John Y. Shu, "Microbuckle initiation in fibre composites : A finite element study", *Journal of the Mechanics and Physics of Solids*, 43 (1995), 1887T.J. Vogler, S. Kyriakides, “Initiation and axial propagation of kink bands in fiber composites”, *Acta Materialia*, **45**, (1997), 2443

[48] T.J. Vogler, S.-Y. Hsu, and S. Kyriakides, "On the initiation and growth of kink bands in fiber composites: part II analysis" *International Journal of Solids & Structures*, **38**, (2001), 2653

[49] T. W. Clyne and A. J. Phillipps, “Interfacial control and macroscopic failure in long fibre reinforced and laminated inorganic composites”, *Composites Science and Technology*, **51**, (1994), 271

[50] Argon, A.S, “Fracture of Composites”, *Treatise of Materials Science and Technology*, **Vol I**, (1972), Academic Press, New York

[51] B. Budiansky, N. A. Fleck and J. C. Amazigo, "On kink-band propagation in fiber composites", *Journal of the Mechanics and Physics of Solids*, **46** (1998), 1637

[52] J. Lankford, “The failure of fiber-reinforced ceramic-matrix composites under dynamic loading*.”, JOM-J. Min. Metals Mater*. Sot., 47, (1995), 64

[53] M.P.F. Sutcliffe and N.A. Fleck, “Microbuckle propagation in fiber composites”, *Acta Materialia*., 45, (1997), 921

[54] L.N. McCartney and W.R. Broughton, “Continuous Parallel Fiber Composites: Deformation and Strength”, in *Encyclopedia of Materials: Science and Technology*,1609

[55] J.Hopkinson, “On the rupture of an iron wire by a blow”, J.Proc. Manchest. Liter Philos., Soc., **11**, (1872), 40.

[56] B. Hopkinson, “A method of measuring the pressure produced in the detonation of high explosives or by the impact of bullets”, *Phil. Trans. Roy. Soc. Lond. A*, **213**,(1914), 437

[57] R.M. Davies, “A simple modification of the Hopkinson pressure bar” in *Poc 7th Int. Congress on Applied mechanics*, **1**, (1948), 404.

[58] H. Kolsky, “An investigation of mechanical properties of materials at very high rates of loading”, *Proc. Phys. Soc. Lond. B*, **62**, (1949), 676.

[59] J. Harding, E.D. Wood, J.D. Campbell, “Tensile testing of materials at impact rates of strain”, *Journal of Mechanical Engineering Science*, 2, (1960), 88

[60] A.R. Champion, “Fiber FP Reinforced Metal Matrix Composites”, Proceedings of the 1978 International Conference on Composite Materials, 1978, 884

[61] M. S. Yong and A. J. Clegg, “Process Optimisation for a Squeeze Cast Magnesium Alloy”, *Journal of Materials Processing Technology*, 145, (2004), 134

[62] www.magnesium-elektron.com/data/downloads/DS452RZ6.PDF TradeMark of Magnesium Elektron

[63] www.magnesium.com

[64] M. Güden, and I.W. Hall, “High strain rate deformation behavior of a continuous fiber reinforced aluminum metal matrix composite”, Computers and Structures, **76**, (2000), 139

[65] W.S. Wolbach, S.R. Bryan, G.L. Shoemaker, T.W. Krucek, R.D. Maier, K.K. Soni, J.M. Chabala, R. Mogilevsky, R. Levi-Setti, “Optimization of chemical reactions between alumina/silica fibres and aluminum-magnesium alloys during composite processing”, *Journal of Materials Science*, **32**, (1997), 1953

[66] J.Kiehn, K.U. Kainer, P. Vostry and I. Stulikova, “Resistivity changes due to precipitation effects in fibre reinforced Mg-Al-Zn-Mn alloy”, *Physica Status Solidi,* **161**, (1997), 85

[67] L.Y. Wei, G.L. Dunlop, H. Westengen, “Solidification behavior and phase constituents of cast Mg-Zn—misch metal alloys”,

[68] G. Ravichandran, G. Subhash, “Critical appraisal of limiting strain rates for compression testing ceramics in a split Hopkinson pressure.” *Journal of American Ceramic Soceity*, (1994), **77**, 263

[69] B. J. Weng, S. T. Chang and S. E. Hsu, “Microfracture mechanisms of fibre reinforced aluminium composites”, *Materials Science and Engineering A*, **156**, (1992), 143

[70] C. C. Poteet and I. W. Hall, "High strain rate properties of a unidirectionally reinforced C/Al metal matrix composite", *Materials Science and Engineering A*, **222**, (1997), 34

[71] M.O. Pekguleryuz, A.A. Kaya, “Creep resistant magnesium alloys for powertrain applications”, *Advanced Engineering Materials,* 5, (2003), 866

[72] R. D. Doherty, D.A. Hughes, F.J. Humphreys, J.J. Jonas, D. Juul Jensen, M.E. Kassner, W.E. King, T.R. McNelley, H.J. McQueen, A.D. Rollett, ”Current issues in recrstallization: a review”, *Materials Science and Engineering A*, **238**, (1997), 219

[73] D.L. Yin, K.F. Zhang, G.F. Wang, W.B. Han, “Warm deformation behavior of hot-rolled AZ31 Mg alloy”, *Materials Science and Engineering A*, In Press, Corrected Proof, (2004)

[74] D. Ponge, G. Gottstein, “Necklace formation during dynamic recrystallization: mechanisms and impact on flow behavior”, *Acta Materiala*, **46**, (1998), 69

[75] X. Wang, E. Brünger, G. Gotttstein, “The role of twinning during dynamic recrystallization in alloy 800H”, *Scripta Materialia*, **46**, (2002), 875

[76] Z.S. Basinski, M.S. Szczerba, M. Niewczas, J.D. Embury, S.J. Basinski, “ ”. Rev. Metall. **94**, (1997), 1037

[77] D.R. Chichili, K.T. Ramesh, and K.J. Hemker, “The high strain rate response of alpha titanium: experiments, deformation mechanisms and modeling”, *Acta Materiala*, **46**, (1998), 1025

[78] K. Yu, W.Li, J. Zhao, Z. Ma, R Wang, “Plastic deformation behaviors of a Mg-Ce-Zn-Zr alloy”, *Scripta Materialia*, **48**, (2003), 1319

[79] R. Dowling, J. Harding and J. D. Campbell, *J. Inst. Met*., **98,** (1970) p. 215.

[80] P. S. Follansbee, Metallurgical Applications of Shock Wave and High-Strain Rate Phenomena (L. E. Murr, K. P. Staudhammer and M. A. Meyers, Eds.), Marcel Dekker, New York, p. 451, 1986.

[81] B. Budianski, N.A. Fleck, “Compressive failure of fibre composites”, *Journal of the Mechanics and Physics of Solids*, **41**, (1993), 183

[82] C.M. Cady, G.T. Gray, “Influence of strain rate on the deformation and fracture response of a 6061-T6 Al-50 vol.% Al_2O_3 continious-reinforced composite” , *Materials Science and Engineering A*, **298**, (2001), 56

[83] T.W. Clyne and P.J. Winters, in *An Introduction to Metal Matrix Composites*, (Cambridge University Press, Cambridge, 1993)